ELSEVIER

Comput. Methods Appl. Mech. Engrg. 120 (1995) 65–118

Computer methods in applied mechanics and engineering

Dynamics of sliding geometrically-exact beams: large angle maneuver and parametric resonance[☆]

L. Vu-Quoc*, S. Li

Aerospace Engineering, Mechanics & Engineering Science, University of Florida, Gainesville, FL 32611, USA

Received 27 March 1993

Abstract

We present the dynamic formulations for sliding beams that are deployed or retrieved through prismatic joints. The beams can undergo large deformation, large overall motion, with shear deformation accounted for. Until recently, the sliding beam problem has been tackled mostly under small deformation assumptions, or under quasi-static motion. Here we employ geometrically-exact beam theory. Two theoretically-equivalent formulations are proposed: A full Lagrangian version, and an Eulerian–Lagrangian version. A salient feature of the problem is that the equations of motion in both formulations are defined on time-varying spatial domain. This feature raises some complications in the computational formulation and computer implementation. We discuss in detail the transformation of the equations in the full Lagrangian formulation from a time-varying spatial domain to a constant spatial domain via the introduction of a stretched coordinate. A Galerkin projection is then applied to discretize the resulting governing partial differential equations. Even though the system does not have any rotating motion as in gyroscopic systems, the inertia operator has a weak form that can be decomposed exactly into a symmetric part and an anti-symmetric part. The distinction between the full Lagrangian formulation and the Eulerian–Lagrangian formulation from the computer implementation viewpoint is indicated. Several numerical examples – 'spaghetti/reverse spaghetti problem,' beam under combined sliding motion and large angle maneuver, parametric resonance – are given to illustrate the versatility of the proposed approach. The results reveal a rich dynamical behavior to be explored further in the future.

Dedicated to the memory of Professor Juan Carlos Simo[†]

1. Introduction

Flexible moving structures are present in several important applications, encompassing diverse engineering areas such as hot rolling process, copy machines, film and tape transporters, cloth handling equipment, traversing yarn system in the textile industry, and even fluid jets [1]. Another class of important engineering system having flexible moving structures consists of robot manipulator arms, or deployable space structures, with prismatic joints. In these (primal) problems, the structures are moving relative to the supports (which themselves may undergo rigid body motion). A class of problems dual to the above is found in moving loads over flexible beams, where the moving loads can be thought of as moving supports. These dual problems also have important engineering applications such as high-speed trains moving on flexible guideways [2–7].

A first formulation for the primal problem is presented by Carrier [8] who studied the 'spaghetti problem', which consists of describing the motion of a cord of finite length, being retrieved vertically

---

[☆] The present work was presented at an invited seminar at the MacNeal-Schwendler Corp., Pasadena, CA, and at the Symposium on Mechanics of Flexible Media, ASME Winter Annual Meeting, Anaheim, CA, in November 1992 (Vu-Quoc and Li [53]).

[*] Corresponding author.

[†] Whose early demise is a great loss for the applied and computational community.

0045-7825/95/$09.50
SSDI 0045-7825(94)00051-N

into an orifice. The cord was modeled using string theory. The 'spaghetti problem' owes its name to an amusing observation that compares the mechanical process of retrieving the cord to the sucking of spaghetti by a person at lunch.[1] Also investigated in the same paper was a dual problem consisting of an oscillating elastic guitar string having a rigid support being slided along the string. For these two problems to be tractable analytically, linear (small deformation) string theory was used.

Demanded by industrial applications, there has since been a plethora of publications focusing on the study of 'axially moving continua', Zaiser [9] appears to be the first who derived successfully the non-linear equations for a moving string.[2] Mote [10] and Thurman and Mote [11] gave accounts on the non-linear oscillation of axially moving strings. A more recent follow-up work on moving strings was given in [12], with a thorough review of the literature on the subject in [13]. Simply-supported boundary conditions at both ends of the string were assumed, since research on moving strings was motivated by applications such as high-speed magnetic and paper tapes, power transmission chains and belts, etc.[3]

The advent of space exploration and robotic technology requires a consideration of the flexural stiffness of axially moving 'strings', thus making the latter into sliding beams, with cantilever boundary conditions. Early works on the sliding beam problem often relied on the small deformation assumption imposed a priori to obtain the linearized equations. Cherchas [14], Lips and Modi [15], Tsuchiya [16],[4] Ibrahim and Modi [17], Kalaycioglu and Misra [18] and Creamer [19] are some examples of research works on sliding beams for applications in aerospace engineering. Most of these works are concerned with the deployment of flexible beams (reverse spaghetti problem), and not so much on their retrieval (spaghetti problem), for a simple reason, that in general once deployed, the appendages of a spacecraft are expected to remain in place throughout the lifetime of the spacecraft. When a study of non-linear deformation is needed, the sliding beam was modeled, not by using beam theory, but by using a chain of links connected by elastic hinges as in, e.g. [20, 21].

In robotic applications, sliding beams are designed to function under both deployment and retrieval. Rapid periodic sliding motion of beams can be found in machine tools. In this area too, sliding beams (manipulator arms with prismatic joints) were often modeled using the small deformation assumption at the outset. With the limited power supply in space environment, manipulator arms with prismatic joints have an advantage over those with revolute joints since the former consume less energy. Most past studies on flexible manipulators concentrated on the dynamics and control of manipulators with revolute joints. To date, however, only a small number of studies have been conducted on flexible manipulators with prismatic joints. Perhaps the reason is due to the complexity of the model having its vibrating length changing with time. Such problem does not arise in the case of manipulators with revolute joints, where the links have fixed lengths.

Elmaraghy and Tabarrok [22], and Zajaczkowski et al. [23, 24] presented a stability analysis for Euler–Bernoulli beams subjected to periodic sliding motions. Their analysis, even though restricted to linear beams, revealed the complex nature of the instability of sliding beams. It is then reasonable to expect that the stability behavior of fully non-linear sliding beams would be even richer, and may contain surprising results. A model for robot arm with two revolute joints, one prismatic joint and a flexible link, together with numerical results, were given in [25]. Clamped-free mode shapes were used to model the vibration in the flexible link. In their model, the mode shapes were assumed to be time independent, and thus the sliding motion was not completely accounted for, perhaps for the purpose of simplifying for the controller design and due to the relatively slow sliding motion considered. In a different study, by considering the time rate of change of the total vibrational energy, Wang and Wei [26] presented a formulation for the sliding Euler–Bernoulli beam. They used the spectral Galerkin method to discretize the spatial coordinate by assuming time-dependent mode shapes. Similar to this approach is the work of Krishnamurthy [27] who considered a dynamic model for flexible cylindrical

---

[1] Professor Carrier's interest in the spaghetti problem at that time was primarily as an exercise in applied mathematics, without being motivated by any other particular applications [54].

[2] Tabarrok et al. [32]. See also Ames et al. [55].

[3] More recently, Hwang and Perkins [56] give a stability analysis of axially moving beams, using non-linear rod model, that admit initial curvatures due to sagging.

[4] See also Jankovic [57].

manipulators.[5] More recently, Pan et al. [28, 29] used the Lagrangian formulation to derive the equations of motion for a chain of flexible links connected to each other either by revolute joints or by prismatic joints. Results from numerical simulations were compared with experimental measurements. The importance of accounting for the sliding motion in the vibrational/positional control of sliding beams is considered by Buffinton [30] and Tadikonda and Baruh [31].

The first to formulate the equations for fully non-linear sliding beams appear to be Tabarrok et al. [32] for applications to spacecraft antennae. Unlike previous works in which the equations were derived with simplifying assumptions imposed a priori, these authors first obtained the equations for a non-linear Euler–Bernoulli beam having time-varying length. But due to the difficulty of obtaining analytical solutions to non-linear problems, linearized equations had to be considered. These authors then linearized the resulting non-linear equations of motion in a consistent manner, however, with the introduction of small deformation and inextensibility assumptions. Such linearization process is necessary for obtaining analytical solutions due to the difficulty of performing non-linear analyses. The linearized equations possess extra convective terms as compared to the equation for beams with fixed length.

More recently, Mansfield and Simmonds [33] studied the fully non-linear reverse spaghetti problem. They formulated the equations for the elastica, sliding out of a horizontal guide, and under the effects of gravitation. Similar to Tabarrok et al. [32], the elastica is inextensible. Their work was motivated by the motion of a sheet of paper coming out of a copy machine. Also motivated by high-speed copy machines with paper speed approaching 2 m/s, Stolte and Benson [34] extended the work of Mansfield and Simmonds [33] to account for arbitrary paper exit angle (i.e. not horizontal) and with accelerating paper feed rate. A distinct feature of these more recent formulations is the use of non-linear models and their solutions, which provide better tools to gain insight into the dynamic behavior of this non-linear problem. These studies, however, have left more to be desired as far as non-linear dynamics and stability are concerned.

Within a prismatic joint, the mechanical interaction between the joint wall and the beam may be more complex in many ways. There are indeed some concerns about the modeling of what actually happens mechanically inside the joint. Future works should address these concerns in more details. Since for most industrial applications, the motion of the beam inside the joint channel can be complicated, but also of less interest than what happens outside the channel, most works on this topic do not model the beam part inside the joint in detail.

1.1. The proposed formulations

Our approach is based on the geometrically-exact theory presented in [35], which addressed the case of beams with fixed undeformed length. The computational formulation for beams with fixed undeformed length, together with several complex numerical examples, are given in [36]. Geometrically-exact structural theories are shown to be versatile in a wide range of applications. A geometrically-exact formulation for the dynamics of multibody flexible spacecrafts is introduced in [37]. For an extensive historical review of past contributions to this subject, we refer to Simo and Vu-Quoc [38].

Two formulations for sliding geometrically-exact beams are proposed herein: A full Lagrangian version and an Eulerian–Lagrangian version. In the full Lagrangian formulation, the resulting equations of motion resemble closely those for beams with fixed undeformed length; the inertia operator does not carry any convective terms. The difference is, however, the time-dependent material domain, which can cause certain inconvenience in the computer implementation, requiring alterations of the existing data structure in conventional finite element codes. An approach adopted to circumvent such inconvenience is to transform the time-varying material domain to a fixed domain via the introduction of a stretched coordinate. Such transformation leads to equivalent equations of motion having, however, convective terms in the inertia operator. A comparison of the equations of motion for a geometrically-exact beam with fixed undeformed length to those with varying undeformed length underscores the additional physics encountered in sliding beams. Finally, with the domain being fixed, a

---

[5] See also Weeks [58].

conventional Galerkin projection can be employed to discretize the governing equations, without requiring extensive modifications to the basic data structure and data flow in conventional finite element codes. With this formulation, a sliding beam problem is first solved on a fixed domain; the results are then transformed back to the actual space by a post-processing. An important feature of the proposed full Lagrangian formulation using stretched coordinate is that the inertia operator has a weak form that can be decomposed exactly into a symmetric (self-adjoint) part and an anti-symmetric (non-self-adjoint) part; the resulting semi-discrete equations are similar to those of gyroscopic systems, even though the system has only sliding, not rotating, motion.

While the full Lagrangian formulation for sliding beams, before the transformation using a stretched coordinate, differs from the formulation for beams with fixed material length given in [35] only in the changing of the material domain, the proposed Eulerian–Lagrangian formulation begins from a different viewpoint. An intermediate configuration fixed in the inertial frame plays the role of a 'material' configuration with respect to the current deformed configuration. On the other hand, with respect to the sliding undeformed beam in rigid body motion, this intermediate configuration plays the role of a (spatially fixed) Eulerian domain (with moving boundary, though). The equations of motion are expressed with respect to the coordinates of the intermediate configuration. Even though the resulting equations in the two formulations are different, they can be obtained from each other via appropriate coordinate transformations.

The present formulations encompass formulations in previous works on sliding beams, among which are the linearized approaches widely adopted in the past, as particular cases. The sliding geometrically-exact beam can accommodate shear deformation, extensibility, large deformation, large overall motion. Many robotic and space structure applications involve large overall motions, and in particular large angle maneuvers, of flexible beams under deployment or retrieval. A salient feature of the present geometrically-exact formulation is a natural accommodation of large overall motions in sliding beams. Even though the inertia operator becomes more complex due to the presence of convective terms, the versatility of geometrically-exact theory with respect to large overall motion and large deformation is intactly preserved. The dynamics of sliding beams is referred directly to the inertial frame, bypassing the need for a floating reference frame. We use this versatile tool to investigate the fully non-linear spaghetti problem, the combined sliding motion and large angle maneuver, and the *contained* parametric resonance.

In the present work, we consider only the cantilever boundary conditions. From the stability viewpoint, a linear sliding cantilever beam is neither a conservative nor a gyroscopic system (cf. [39]). The problem will become more complex, if in addition, we have large deformation. From the energy balance viewpoint, the rate of change of energy in a sliding beam with prescribed time-varying length, which is an open physical system, is time-dependent. It was shown that a sliding linear Euler–Bernoulli beam exiting a channel with uniform velocity has a positive energy supply rate [26]. Thus, the total energy can accumulate in time if damping is weak enough. Such accumulation of energy provides a physical ground for instability. Wang and Wei [26] presented numerical examples of parametric resonance existing in linear sliding beams.

There is a fundamental difference in the character of parametric resonance found in the present fully non-linear sliding beam formulation as compared to that in the linear formulation: Unlike the linear theory, which leads to a blow-up of the structural displacement to infinity at resonance, we have here *contained* resonance in the sense that, even though the beam can undergo violent vibration at resonance, its structural displacement always remains finite. Infinite structural displacement can only occur if the beam material breaks down, but this possibility is not considered herein. On the other hand, considerable numerical difficulties are encountered at such parametric resonance, as the semi-discrete differential equations become much 'stiffer' than usual, requiring extreme care in the choice of the solution strategy and the choice of the time-step sizes. In these cases, the failure of conventional integration strategy manifests itself through the blow-up of the numerical results at resonance, indicating that a revision of the integration strategy is needed.

An important issue worth addressing here is the role of non-linear beam theories in capturing the stiffening effects in structures subjected to significant centrifugal forces and/or longitudinal inertial forces. Centrifugal forces are present in rapidly rotating structures, whereas longitudinal inertial forces are present in axially moving structures having transverse deflections. In sliding beams under large angle maneuvers, one encounters a combination of both motions (see Section 5 for an example). Since often linearized equations are of interest because they are easy to work with (e.g. for the control purposes), it was pointed out in [40, 41] that unless a consistent linearization of the non-linear equations of motion is performed—as opposed to using small deformation assumption at the outset of the formulation—the stiffening effects cannot be correctly captured. A 'premature' linearization can lead to results opposite to that found in reality.[6] The present formulations readily include all relevant dynamic effects due to rapid rotation and rapid sliding motion.

The organization of the paper is as follows. In Section 2, we present the full Lagrangian formulation for planar, sliding, geometrically-exact beams. The partial differential equations (PDEs) of motion are derived for the case with time-varying domain, followed by a transformation of the governing PDEs to a fixed domain. The alternative, but theoretically equivalent, Eulerian–Lagrangian formulation is given in Section 3. Discussed in Section 4 is Galerkin projection for discretizing the full Lagrangian PDEs on fixed domain, leading to a convenient finite element implementation. Time discretization is introduced via the Newmark algorithm. A brief discussion will be given on the computational formulation and computer implementation aspects for the Eulerian–Lagrangian PDEs developed in Section 3. Some comparison with linearized models will be given. Finally, we present in Section 5 several numerical examples that involve the spaghetti problem, reverse spaghetti problem, combined dynamic deployment and large angle maneuvers, and parametric resonance of sliding beams.

2. Full Lagrangian formulation

The essential ingredient in the full Lagrangian formulation for sliding beams is the use of geometrically-exact theory [35] based on a spatially fixed material (initial undeformed) configuration with moving partition boundary.

It is common to assume that the material frame coincides with the spatial frame, which plays the role of an inertial frame. Such choice is purely for the convenience of the formulation. The initial undeformed configuration is customarily chosen as the material configuration whose coordinate systems do not necessarily coincide with those of the spatial configuration. A general concept is to view the material configuration as a different space than the spatial configuration, with a different coordinate system, even though both configurations are embedded in the same ambient Euclidean space (e.g. $\mathbb{R}^2$). The structural deformation is described by a mapping, which could be time-dependent, from the material configuration to the spatial configuration.

The deformation of sliding beams can be 'naturally' decomposed into a rigid sliding translation of the initial undeformed beam to the sliding undeformed beam, and a superposed finite deformation from the sliding deformed beam; a description of the sliding motion is given in Fig. 1.[7] As shown in Fig. 3, the sliding undeformed beam is not the same as the 'shadow beam' discussed in [35]: Unlike the shadow beam that undergoes rigid body translation and rotation for structures subjected to large overall motions, the sliding undeformed beam only translates, but does not rotate, with respect to the inertial spatial frame. Thus, the orientation of the sliding undeformed beam in the spatial frame remains constant throughout the motion.

We will postpone, however, the above 'natural' viewpoint of sliding deformation until Section 3. Somewhat less 'natural' is the viewpoint adopted in the present full Lagrangian formulation. The initial undeformed configuration, which can have any arbitrary orientation and is fixed within the spatial configuration, is chosen to be the material configuration, which may have a coordinate system not necessarily coincident with the spatial coordinates (Fig. 3). The material configuration is divided into two parts—inside the joint channel and outside the channel—with the partition boundary (or channel orifice) moving with respect to the material frame, i.e. the channel orifice is moving relative to the material observer O_X as shown in Fig. 2. On the other hand, in the 'natural' viewpoint, the sliding undeformed beam is moving relative to the spatial observer O_x.

---

[6] It is perhaps due to a certain 'linearization' process that the equations in [59] did not reduce exactly to those in [32], as noted in [31].

[7] Even though the initial undeformed configuration is drawn horizontal in Fig. 1 to avoid confusion in the explanation of different configuration spaces, the formulations presented here allow *arbitrary* orientation of the initial configuration; see Fig. 3.

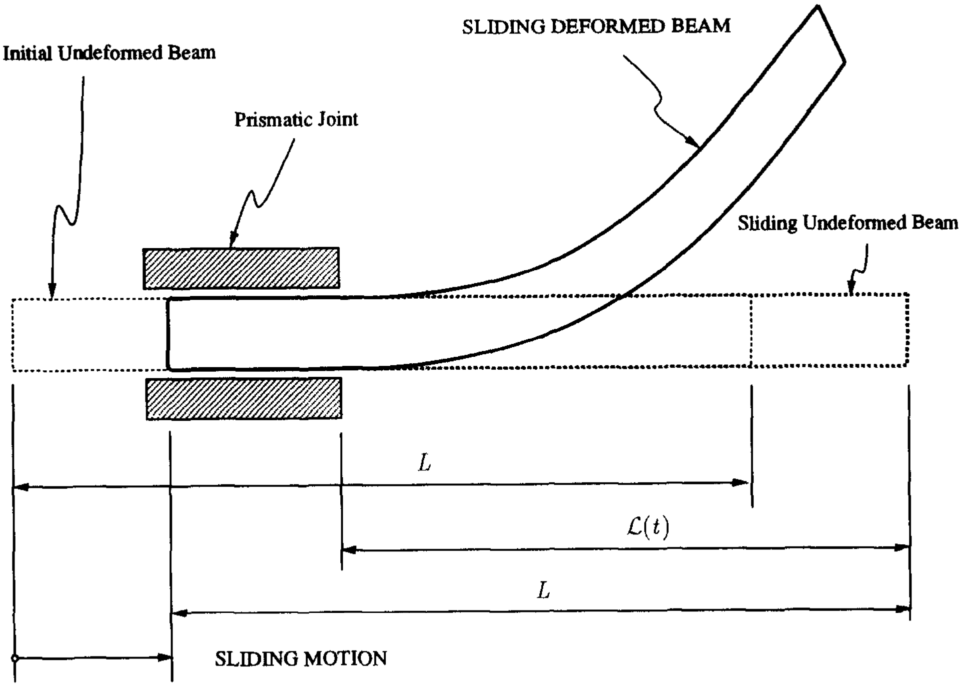

Fig. 1. Sliding beam: Description of sliding motion, time-varying length $\mathscr{L}(t)$.

Let (x^1, x^2) be the coordinate system for the spatial configuration, denoted by $\mathscr{B}_t$, and $\{e_1, e_2\}$ the related basis vectors. The material configuration, denoted by $\mathscr{B}_0$, is parameterized by the coordinates (X^1, X^2), having basis vectors $\{E_1, E_2\}$. The material basis vectors $\{E_1, E_2\}$ do not necessarily coincide with the spatial basis vectors $\{e_1, e_2\}$. The origin O_x of the spatial coordinates (x^1, x^2) is also the center of rotation in the present formulation. Let O_X designate the origin of the material coordinates. Thus, the material configuration $\mathscr{B}_0$ in Fig. 2 can be described as[8]

$$\mathscr{B}_0 := \{(X^1, X^2) \in \mathbb{R}^2 \,|\, X^1 \in]0, L[, X^2 \in]-h, h[\} . \tag{2.1}$$

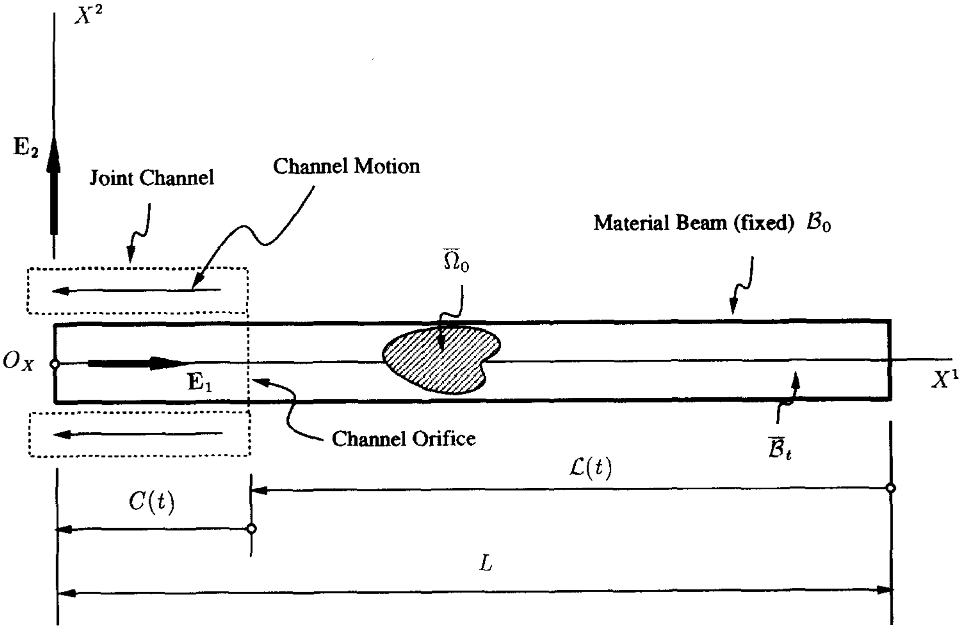

Fig. 2. Sliding beam: Material configuration $\mathscr{B}_0$. Moving partition boundary (channel orifice). The figure shows the case of beam under deployment: The channel orifice is moving toward the material observer O_X.

---

[8] An *open* interval is written as]a, b[.

Let ϑ_0 denote the (constant) angle from $\boldsymbol{e}_1$ to $\boldsymbol{E}_1$ (see Fig. 3); the angle ϑ_0 essentially represents the initial orientation of the undeformed sliding beam with respect to the inertial frame $\{\boldsymbol{e}_1, \boldsymbol{e}_2\}$. The basis vectors describing the shadow beam configuration are denoted by $\{\boldsymbol{a}_1, \boldsymbol{a}_2\}$ (Fig. 3).

2.1. Basic kinematic assumptions

The part of the material (undeformed) beam $\mathscr{B}_0$ inside the channel is assumed to be non-deformable (even axially); the part outside the channel, denoted by $\bar{\mathscr{B}}_t$, is finitely deformable, and is the part that we are interested in. Let the length of the material beam inside the channel be denoted by

$$C(t) := L - \mathscr{L}(t)\,, \tag{2.2}$$

where L is the total length of the material beam, and $\mathscr{L}(t)$ the time-varying length of the material beam outside the channel (Fig. 1). The time-dependent vector

$$\boldsymbol{C}(t) := C(t)\boldsymbol{E}_1 = C(t)[\cos\vartheta_0\, \boldsymbol{e}_1 + \sin\vartheta_0\, \boldsymbol{e}_2] \tag{2.3}$$

essentially describes the motion of the channel orifice relative to the material observer O_X. Thus, the time-varying subset $\bar{\mathscr{B}}_t$ of the material configuration $\mathscr{B}_0$, corresponding to the deformable part of the sliding beam outside the channel, can be described by

$$\bar{\mathscr{B}}_t := \{(X^1, X^2) \in \mathbb{R}^2 \mid X^1 \in\,]C(t), L[\,, X^2 \in\,]-h, h[\,\} \subset \mathscr{B}_0\,. \tag{2.4}$$

Let the spatial point $x = (x^1, x^2) \in \mathscr{B}_t$ be the image of the material point $X = (X^1, X^2) \in \bar{\mathscr{B}}_t$ outside the channel under the deformation map; the relationship between x and X at a given time t is

$$\boxed{x = X - \boldsymbol{C}(t) + \boldsymbol{u}(X, t)\,, \quad \text{for}\, X \in \bar{\mathscr{B}}_t\,,} \tag{2.5}$$

where $\boldsymbol{u}(X, t) = u^\alpha(X, t)\boldsymbol{e}_\alpha$ denotes the displacement vector[9] of the material point X.

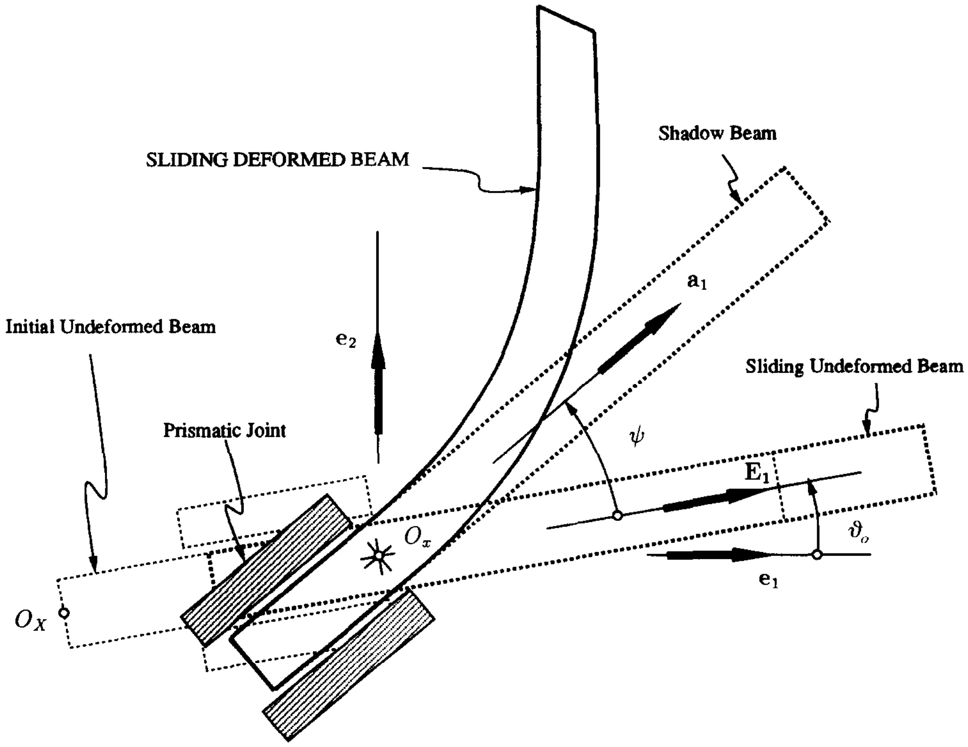

Fig. 3. Sliding beam: Configuration spaces. Initial (material) configuration, sliding undeformed configuration, shadow beam, sliding deformed (spatial) configuration.

---

[9] Summation convention is implied on repeated indices, with Greek indices take values in $\{1, 2\}$. Also, similar to $X = (X^1, X^2)$, we write $\boldsymbol{u}(X, t)$ as a shorthand notation for $\boldsymbol{u}(X^1, X^2, t)$.

REMARK 2.1. The displacement vector $\boldsymbol{u} = u^{\alpha}\boldsymbol{e}_{\alpha}$ is customarily defined as

$$\boldsymbol{u} := \boldsymbol{x} - \boldsymbol{X}\,, \qquad \text{or} \qquad \boldsymbol{x} = \boldsymbol{X} + \boldsymbol{u}\,. \tag{2.6}$$

There is a major difference between (2.5) and (2.6). The assumption that there is no deformation inside the channel, and thus the translation $\boldsymbol{C}(t)$ of the channel orifice with respect to the material observer O_X, is already accounted for in the displacement vector $\boldsymbol{u}$ as defined in (2.5). On the other hand, unlike the shadow beam approach (see Fig. 3), displacements due to finite large overall rotations are not eliminated from the displacement $\boldsymbol{u}$ in (2.5), i.e. the displacement $\boldsymbol{u}$ is measured relative to the fixed spatial frame $\{\boldsymbol{e}_1, \boldsymbol{e}_2\}$. This feature of the present full Lagrangian formulation allows a convenient accommodation of the sliding motion of the beam, while retaining the versatility of geometrically-exact formulation with regards to large overall motions. As an illustration, we refer the reader to Example 5.3 for a deployment of a beam under large angle maneuver in Section 5. □

Let us now introduce some kinematic quantities. The orthonormal basis vectors attached to a typical cross section at the point with position $X^1\boldsymbol{E}_1$ are denoted by $\{\boldsymbol{t}_1(X^1, t), \boldsymbol{t}_2(X^1, t)\}$, with $\boldsymbol{t}_1$ being always normal to the cross section. The angle from the spatial basis vector $\boldsymbol{e}_1$ to the section basis vector $\boldsymbol{t}_1(X^1, t)$ is denoted by $\vartheta(X^1, t)$. The whole system can be subjected to large angle rotation about the origin of the spatial frame; such angle of rotation (from $\boldsymbol{E}_1$ to $\boldsymbol{a}_1$) is denoted by $\psi(t)$.[10] Purely due to structural deformation is the rotation angle $\theta(X^1, t)$ from the shadow beam (or channel) axis $\boldsymbol{a}_1$ to the section basis vector $\boldsymbol{t}_1(X^1, t)$. Let $\Delta\vartheta(X^1, t)$ denote the angle from $\boldsymbol{E}_1$ to $\boldsymbol{t}_1$, i.e. the total angle of rotation of a cross section—which includes the rigid body rotation $\psi(t)$ and the deformation rotation θ—from its initial orientation to its current orientation. Therefore,

$$\vartheta(X^1, t) := \vartheta_0 + \Delta\vartheta(X^1, t)\,, \tag{2.7}$$

$$\Delta\vartheta(X^1, t) := \psi(t) + \theta(X^1, t)\,. \tag{2.8}$$

The definition of various angles is best summarized in Fig. 4.

Let $\boldsymbol{\Lambda}$ be the rotation tensor from the material configuration to the spatial configuration defined as follows

$$\boldsymbol{\Lambda} = \Lambda^{\alpha}_{\beta}\boldsymbol{e}_{\alpha} \otimes \boldsymbol{E}^{\beta}\,, \qquad \text{such that} \qquad \boldsymbol{t}_{\beta} := \boldsymbol{\Lambda} \cdot \boldsymbol{E}_{\beta} = t^{\alpha}_{\beta}\boldsymbol{e}_{\alpha}\,. \tag{2.9}$$

Then the matrix of components of $\boldsymbol{\Lambda}$, denoted by $[\Lambda^{\alpha}_{\beta}] \in \mathbb{R}^{2\times 2}$, is[11]

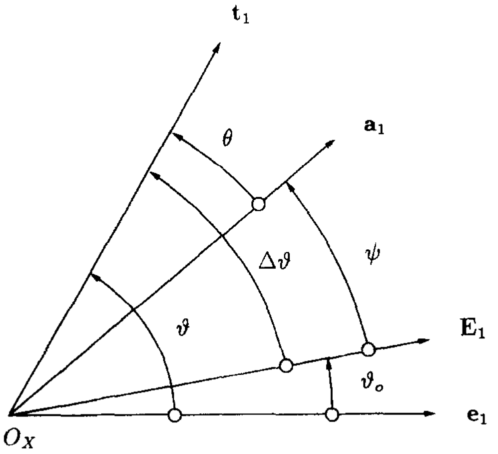

Fig. 4. Sliding beam. Angles of rotation.

---

[10] The angle $\psi(t)$ is similar to that in [35], where it represented the angle from the spatial basis vector $\boldsymbol{e}_1$ to the basis vector $\boldsymbol{a}_1$ of the shadow beam.

[11] With the convention that the superscript α in Λ^{α}_{β} designates the row index, whereas the subscript β designates the column index. This convention is to be applied to all matrices throughout the paper.

$$[\Lambda^{\alpha}_{\beta}] = \begin{bmatrix} \cos\vartheta & -\sin\vartheta \\ \sin\vartheta & \cos\vartheta \end{bmatrix} \in \mathbb{R}^{2\times 2} . \tag{2.10}$$

Extending the Timoshenko kinematic assumption for linear beam deformation—i.e. sections that are plane before deformation remain plane after deformation, but not necessarily perpendicular to the deformed centroidal line—to non-linear deformation to account for shear, the deformation map $\Phi : \bar{\mathcal{B}}_t \rightarrow \mathcal{B}_t$ can be written as follows

$$\boxed{x = \Phi(X, t) := \Phi_0(X^1, t) + X^2 t_2(X^1, t) ,} \tag{2.11}$$

where Φ_0 represents the deformation map of the beam centroidal line (see Fig. 5). The main difference between relation (2.11) above and a similar relation in [35] is in the expression for $\Phi_0(X^1, t)$, which will be given below shortly.

Let $X_0 = ([X^1 - C(t)], 0) \in \bar{\mathcal{B}}_t$ denote a point on the centroidal line (since $X^2 = 0$); the material position vector of X_0 relative to the material observer O_X, denoted by $\mathbf{X}_0$, is

$$\mathbf{X}_0 := X_0 - O_X = [X^1 - C(t)]\mathbf{E}_1 . \tag{2.12}$$

The image of the centroid X_0 under the deformation Φ is denoted by x_0. We have from (2.11) that

$$x_0 = \Phi(X_0, t) = \Phi_0(X^1, t) . \tag{2.13}$$

The expression for $\Phi_0(X^1, t)$ for each part of the material configuration will be given below. We denote the spatial position vectors of x and x_0 relative to the spatial observer O_x by $\boldsymbol{\Phi}$ and $\boldsymbol{\Phi}_0$, respectively

$$\boldsymbol{\Phi} := x - O_x , \qquad \boldsymbol{\Phi}_0 := x_0 - O_x , \tag{2.14}$$

i.e. Φ is a point-to-point mapping, whereas $\boldsymbol{\Phi}$ is the spatial position vector of the image point under the map Φ; a similar interpretation holds for Φ_0 and $\boldsymbol{\Phi}_0$. Inside the channel, i.e. for $X^1 \in]0, C(t)[$ in (2.12),

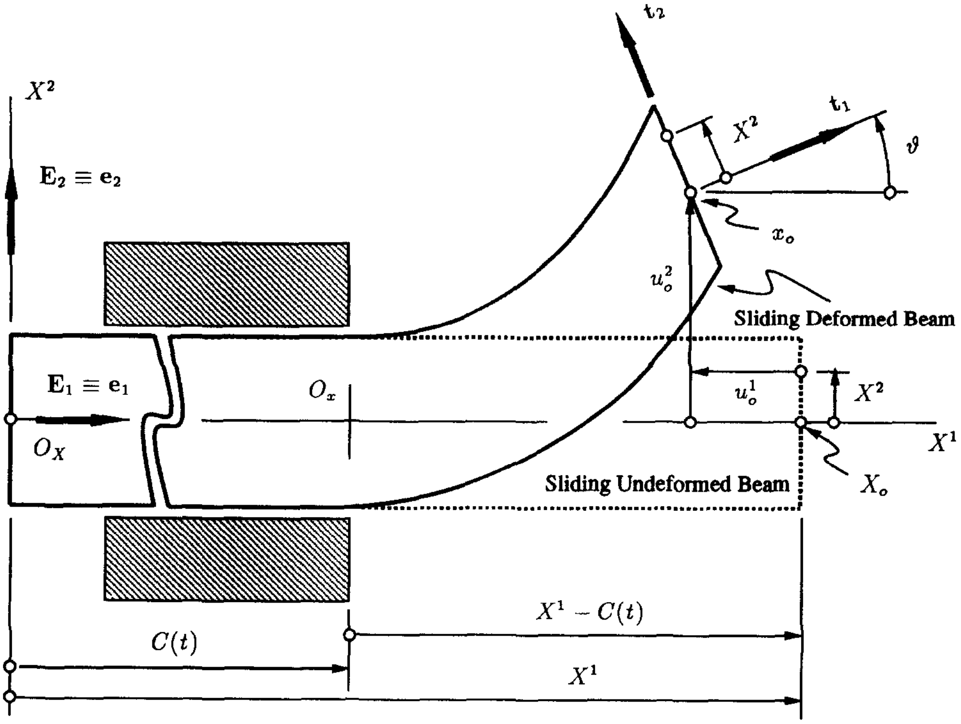

Fig. 5. Sliding beam. Kinematics of deformation. The case with $\vartheta_0 = 0$ is presented above to explain clearly the kinematics of deformation.

the point x_0 is given by a rigid body motion

$$\begin{aligned}\boldsymbol{\Phi}_0(X^1,t) &= [X^1 - C(t)]\boldsymbol{a}_1 \\ &= [X^1 - C(t)]\{\cos(\vartheta_0 + \psi(t))\boldsymbol{e}_1 + \sin(\vartheta_0 + \psi(t))\boldsymbol{e}_2\}\,. \end{aligned} \tag{2.15}$$

Let $\boldsymbol{u}_0(X^1,t) = u_0^\alpha(X^1,t)\boldsymbol{e}_\alpha$ denote the displacement vector of the point X_0 on the centroidal line. Then inside the channel, $\boldsymbol{u}_0 \equiv 0$. Outside the channel, i.e. for $X^1 \in \,]C(t), L[$, the spatial point x_0 is related to the material point X_0 by

$$x_0 = \Phi_0(X^1,t) = X_0 + \boldsymbol{u}_0(X^1,t)\,, \tag{2.16}$$

thus, with the position vector of X_0 defined in (2.12), we have

$$\begin{aligned}\boldsymbol{\Phi}_0(X^1,t) &= [X^1 - C(t)]\boldsymbol{E}_1 + \boldsymbol{u}_0(X^1,t) \\ &= [X^1 - C(t)]\{\cos\vartheta_0\,\boldsymbol{e}_1 + \sin\vartheta_0\,\boldsymbol{e}_2\} + u_0^\alpha(X^1,t)\boldsymbol{e}_\alpha\,, \quad \forall X^1 \in \,]C(t), L[\,. \end{aligned} \tag{2.17}$$

REMARK 2.2. Apart from the time-varying domain $]C(t), L[$, the deformation map for the centroidal line (2.17) accommodates the case where $\vartheta_0 \neq 0$ (i.e. when the material frame is not coincident with spatial frame), whereas Simo and Vu-Quoc [35] consider the particular case where $\vartheta_0 = 0$. A discussion on this aspect in a more general context can be found in [42]. □

2.2. Full Lagrangian equations of motions

We briefly review the derivation of the equations of motion for geometrically-exact beams, with a particular emphasis on sliding beams. Recall that inside the channel, i.e. in $\mathscr{B}_0\backslash\bar{\mathscr{B}}_t$ (see (2.1) and (2.4)), the beam is assumed to be non-deformable. Even though we are considering planar deformation of beams, it is sometimes convenient to think in a 3-D context, where the beam is considered as having a unit width in the $\boldsymbol{E}_3$ direction, such that, e.g. $X^3 \in \,]0,1[$. The area of a cross section in the material configuration is then denoted by

$$\mathscr{A}_0 := \{(X^2, X^3) \in \mathbb{R}^2 \mid X^2 \in \,]-h, h[, X^3 \in \,]0,1[\}\,. \tag{2.18}$$

Let $\boldsymbol{P}(X,t)$ denote the first Piola–Kirchhoff stress (two-point) tensor

$$\boldsymbol{P}(X,t) = \boldsymbol{E}_i \otimes \boldsymbol{T}^i(X,t)\,, \qquad \text{and} \qquad \boldsymbol{T}^i = \boldsymbol{E}^i \cdot \boldsymbol{P}\,, \tag{2.19}$$

where $\boldsymbol{T}^i$ is the spatial traction force corresponding to the material facet with normal $\boldsymbol{E}^i$ (see e.g. [43])[12]. The stress resultant $\boldsymbol{f}$, and the stress couple $\boldsymbol{m}$ with respect to the displaced centroid x_0, per unit of undeformed beam length, are defined as

$$\boldsymbol{f}(X^1,t) := \int_{\mathscr{A}_0} \boldsymbol{T}^1\,\mathrm{d}\mathscr{A}_0\,, \tag{2.20}$$

$$\boldsymbol{m}(X^1,t) := \int_{\mathscr{A}_0} [x - x_0] \times \boldsymbol{T}^1\,\mathrm{d}\mathscr{A}_0 = \int_{\mathscr{A}_0} X^2\boldsymbol{t}_2 \times \boldsymbol{T}^1\,\mathrm{d}\mathscr{A}_0\,, \tag{2.21}$$

where the last equality follows from (2.11) and (2.13).

Consider a spatial control volume $\Omega_t \subset \mathscr{B}_t$ with normal $\boldsymbol{n}$ on the boundary $\partial\Omega_t$. The time rate of the linear momentum, and of the angular momentum with respect to O_x, of Ω_t in terms of the applied forces (i.e. the Euler equations) is given by

$$\frac{\mathrm{d}}{\mathrm{d}t}\int_{\Omega_t} \rho\boldsymbol{v}\,\mathrm{d}(\Omega_t) = \int_{\partial\Omega_t} \boldsymbol{n}\cdot\boldsymbol{\sigma}\,\mathrm{d}(\partial\Omega_t) + \int_{\Omega_t} \rho\boldsymbol{b}\,\mathrm{d}(\Omega_t) \quad \forall\Omega_t \subset \mathscr{B}_t\,, \tag{2.22}$$

$$\frac{\mathrm{d}}{\mathrm{d}t}\int_{\Omega_t} \boldsymbol{\Phi} \times \rho\boldsymbol{v}\,\mathrm{d}(\Omega_t) = \int_{\partial\Omega_t} \boldsymbol{\Phi} \times (\boldsymbol{n}\cdot\boldsymbol{\sigma})\,\mathrm{d}(\partial\Omega_t) + \int_{\Omega_t} \boldsymbol{\Phi} \times \rho\boldsymbol{b}\,\mathrm{d}(\Omega_t) \quad \forall\Omega_t \subset \mathscr{B}_t\,, \tag{2.23}$$

---

[12] The symbol $\boldsymbol{E}^i$ designates a covector, such that $\boldsymbol{E}^i \cdot \boldsymbol{E}_j = \delta^i_j$, where δ^i_j is the Kronecker delta. For Cartesian coordinates, $\boldsymbol{E}^i \equiv \boldsymbol{E}_i$.

where

$$\boldsymbol{v}(x,t) \equiv \boldsymbol{V}(X,t) = \frac{\partial \Phi(X,t)}{\partial t} =: \dot{\boldsymbol{\Phi}} \tag{2.24}$$

is the spatial velocity vector at the spatial point $x = \Phi(X,t) \in \mathscr{B}_t$ (see [43]), $\boldsymbol{\sigma}(x,t)$ is the Cauchy stress tensor, $\boldsymbol{b}(x,t)$ the body force, and $\rho(x,t)$ the mass density. Now let $\bar{\Omega}_0$ be a fixed material volume in the material configuration $\bar{\mathscr{B}}_t$ (see Fig. 2), with normal $N = N_i E^i$ on the boundary $\partial\bar{\Omega}_0$ such that

$$\Omega_t = \Phi(\bar{\Omega}_0, t)\,, \tag{2.25}$$

i.e. Ω_t is the image of $\bar{\Omega}_0$ under the deformation Φ. Even though the boundary of $\bar{\mathscr{B}}_t$ (channel orifice) is changing with time, the material volume $\bar{\Omega}_0$ remains fixed with respect to the coordinates (X^1, X^2), thus the subscript '0' in $\bar{\Omega}_0$. By pulling the integrals in (2.22) and (2.23) back to the material volume $\bar{\Omega}_0$, one obtains (see [43])

$$\frac{\mathrm{d}}{\mathrm{d}t}\int_{\bar{\Omega}_0} \rho_{\mathrm{ref}}\, \dot{\boldsymbol{\Phi}}\, \mathrm{d}(\bar{\Omega}_0) = \int_{\partial\bar{\Omega}_0} \boldsymbol{N}\cdot\boldsymbol{P}\, \mathrm{d}(\partial\bar{\Omega}_0) + \int_{\bar{\Omega}_0} \rho_{\mathrm{ref}}\, \boldsymbol{B}\, \mathrm{d}(\bar{\Omega}_0) \quad \forall \bar{\Omega}_0 \subset \mathscr{B}_t\,, \tag{2.26}$$

$$\frac{\mathrm{d}}{\mathrm{d}t}\int_{\bar{\Omega}_0} \rho_{\mathrm{ref}}\, \boldsymbol{\Phi}\times\dot{\boldsymbol{\Phi}}\, \mathrm{d}(\bar{\Omega}_0) = \int_{\partial\bar{\Omega}_0} \boldsymbol{\Phi}\times(\boldsymbol{N}\cdot\boldsymbol{P})\, \mathrm{d}(\partial\bar{\Omega}_0) + \int_{\bar{\Omega}_0} \boldsymbol{\Phi}\times\rho_{\mathrm{ref}}\boldsymbol{B}\, \mathrm{d}(\bar{\Omega}_0) \quad \forall \bar{\Omega}_0 \subset \bar{\mathscr{B}}_t\,, \tag{2.27}$$

where $\rho_{\mathrm{ref}}(X) = \rho(x,t)J(X,t)$ the mass density per unit volume of undeformed beam, with $J(X,t)$ being the Jacobian determinant of the deformation map $\Phi(X,t)$, and $\boldsymbol{B}(X,t) = \boldsymbol{b}(x,t)$ is the body force.[13] By the divergence theorem, and using $\mathrm{DIV}\boldsymbol{P} = \boldsymbol{T}^i|_i$, the balance of linear and angular momenta (2.26) and (2.27) can be rewritten as

$$\int_{\bar{\Omega}_0} \rho_{\mathrm{ref}}\, \ddot{\boldsymbol{\Phi}}\, \mathrm{d}(\bar{\Omega}_0) = \int_{\bar{\Omega}_0} \mathrm{DIV}\,\boldsymbol{P}\, \mathrm{d}(\bar{\Omega}_0) + \int_{\bar{\Omega}_0} \rho_{\mathrm{ref}}\, \boldsymbol{B}\, \mathrm{d}(\bar{\Omega}_0) \quad \forall \bar{\Omega}_0 \subset \mathscr{B}_t\,, \tag{2.28}$$

$$\int_{\bar{\Omega}_0} \rho_{\mathrm{ref}}\, \boldsymbol{\Phi}\times\ddot{\boldsymbol{\Phi}}\, \mathrm{d}(\bar{\Omega}_0) = \int_{\bar{\Omega}_0} (\boldsymbol{\Phi}\times\boldsymbol{T}^i)|_i\, \mathrm{d}(\bar{\Omega}_0) + \int_{\bar{\Omega}_0} \boldsymbol{\Phi}\times\rho_{\mathrm{ref}}\boldsymbol{B}\, \mathrm{d}(\bar{\Omega}_0) \quad \forall \bar{\Omega}_0 \subset \bar{\mathscr{B}}_t\,. \tag{2.29}$$

We first consider the reduction of the balance of linear momentum (2.28) to a resultant form. From the relation (2.11), we have

$$\ddot{\boldsymbol{\Phi}}(X,t) = \ddot{\boldsymbol{\Phi}}_0(X^1,t) + X^2\ddot{\boldsymbol{t}}_2(X^1,t)\,. \tag{2.30}$$

Let A_ρ be the mass per unit of undeformed beam length, i.e.

$$A_\rho := \int_{\mathscr{A}_0} \rho_{\mathrm{ref}}\, \mathrm{d}\mathscr{A}_0\,, \tag{2.31}$$

and assume that the origin of the X^2 coordinate coincides with the center of mass of a cross section, i.e.

$$\int_{\mathscr{A}_0} \rho_{\mathrm{ref}}\, X^2\, \mathrm{d}\mathscr{A}_0 = 0\,. \tag{2.32}$$

Using (2.30)–(2.32), the inertia operator in (2.28) can be written as

$$\int_{\mathscr{A}_0} \rho_{\mathrm{ref}}\, \ddot{\boldsymbol{\Phi}}\, \mathrm{d}\mathscr{A}_0 = A_\rho\, \ddot{\boldsymbol{\Phi}}_0(X^1,t)\,. \tag{2.33}$$

Next, by the divergence theorem on $\mathscr{A}_0$ and the definition (2.20) of the stress resultant $\boldsymbol{f}$, we can write the divergence term in the balance of linear momentum (2.28) as (cf. [60])

$$\int_{\mathscr{A}_0} \mathrm{DIV}\,\boldsymbol{P}\, \mathrm{d}\mathscr{A}_0 = \frac{\partial \boldsymbol{f}}{\partial X^1} + \int_{\partial\mathscr{A}_0} (N_2\boldsymbol{T}^2 + N_3\boldsymbol{T}^3)\, \mathrm{d}(\partial\mathscr{A}_0)\,. \tag{2.34}$$

---

[13] $\boldsymbol{B}(X,t)$ is the *spatial* body force, parameterized on the material configuration $\mathscr{B}_0$; in other words, $\boldsymbol{B}$ is a spatial vector field covering the deformation map $\boldsymbol{\Phi}$ [43].

The second term in (2.34) is then combined with the body force term in (2.28) to define the applied stress resultant f_r per unit of undeformed beam length

$$f_r := \int_{\partial \mathscr{A}_0} [N_2 \boldsymbol{T}^2 + N_3 \boldsymbol{T}^3] \, \mathrm{d}(\partial \mathscr{A}_0) + \int_{\mathscr{A}_0} \rho_{\mathrm{ref}} \boldsymbol{B} \, \mathrm{d}\mathscr{A}_0 \,. \tag{2.35}$$

Now, since the choice of $\bar{\Omega}_0$ in the balance of linear momentum (2.28) (and also in (2.29)) is completely arbitrary, we can particularize $\bar{\Omega}_0$ to be a transverse slice $\Delta L \times \mathscr{A}_0$ of the material beam $\mathscr{B}_t$, where ΔL is any interval in $]C(t), L[$. The balance of linear momentum (2.28) then becomes

$$\int_{\Delta L} \left(A_\rho \ddot{\boldsymbol{\Phi}}_0 - \frac{\partial \boldsymbol{f}}{\partial X^1} - \boldsymbol{f}_r \right) \mathrm{d}X^1 = 0 \quad \forall \, \Delta L \subset \,]C(t), L[\,. \tag{2.36}$$

With L being a constant, we have from (2.2) that

$$\ddot{C}(t) = -\ddot{\mathscr{L}}(t) \,. \tag{2.37}$$

Then, by using the expression (2.17) for $\boldsymbol{\Phi}_0$ in (2.36), we arrive at the local resultant form of the balance of linear momentum

$$\boxed{A_\rho [\ddot{\boldsymbol{u}}_0 + \ddot{\mathscr{L}} \boldsymbol{E}_1] = \frac{\partial \boldsymbol{f}}{\partial X^1} + \boldsymbol{f}_r \quad \forall X^1 \in \,]C(t), L[\,,} \tag{2.38}$$

by virtue of the du Bois–Reymond lemma (assuming that the integrand in (2.36) is continuous). We now consider the balance of angular momentum (2.29). With the aid of the balance of linear momentum (2.38), and by using the divergence theorem on $\mathscr{A}_0$, the right-hand side of (2.29) can be written as follows (cf. [60])

$$\begin{aligned} &\int_{\partial \bar{\Omega}_0} (\boldsymbol{\Phi} \times \boldsymbol{T}^i)|_i \, \mathrm{d}(\bar{\Omega}_0) + \int_{\bar{\Omega}_0} \boldsymbol{\Phi} \times \rho_{\mathrm{ref}} \boldsymbol{B} \, \mathrm{d}(\bar{\Omega}_0) \\ &= \int_{\Delta L} \left\{ \frac{\partial \boldsymbol{m}}{\partial X^1} + \frac{\partial \boldsymbol{\Phi}_0}{\partial X^1} \times \boldsymbol{f} + \boldsymbol{m}_r + \int_{\mathscr{A}_0} \rho_{\mathrm{ref}} (\boldsymbol{\Phi}_0 \times \ddot{\boldsymbol{\Phi}}_0) \, \mathrm{d}\mathscr{A}_0 \right\} \mathrm{d}X^1 \,, \end{aligned} \tag{2.39}$$

with the applied stress couple $\boldsymbol{m}_r$ defined as

$$\boldsymbol{m}_r := \int_{\partial \mathscr{A}_0} (\boldsymbol{\Phi} - \boldsymbol{\Phi}_0) \times \left[\sum_{\alpha=2}^{3} N_\alpha \boldsymbol{T}^\alpha \right] \mathrm{d}(\partial \mathscr{A}_0) + \int_{\mathscr{A}_0} (\boldsymbol{\Phi} - \boldsymbol{\Phi}_0) \times \rho_{\mathrm{ref}} \boldsymbol{B} \, \mathrm{d}\mathscr{A}_0 \,. \tag{2.40}$$

Now, using (2.11), (2.30), the choice of the X^2 coordinate in (2.32), together with the definition of the mass moment of inertia of a cross section

$$I_\rho := \int_{\mathscr{A}_0} \rho_{\mathrm{ref}} (X^2)^2 \, \mathrm{d}A_0 \,, \tag{2.41}$$

the inertia term (left-hand side) of the balance of angular momentum (2.29) and the inertia (last) term in (2.39), which is shifted to the left-hand side, become

$$\int_{\bar{\Omega}_0} \rho_{\mathrm{ref}} \{ \boldsymbol{\Phi} \times \ddot{\boldsymbol{\Phi}} - \boldsymbol{\Phi}_0 \times \ddot{\boldsymbol{\Phi}}_0 \} \, \mathrm{d}(\bar{\Omega}_0) = \int_{\Delta L} I_\rho \boldsymbol{t}_2 \times \ddot{\boldsymbol{t}}_2 \, \mathrm{d}X^1 = \int_{\Delta L} I_\rho \ddot{\vartheta} \boldsymbol{e}_3 \, \mathrm{d}X^1 \,, \tag{2.42}$$

where the last equality comes from the restriction to the planar sliding motion in the present work, i.e.

$$\ddot{\boldsymbol{t}}_2 = \frac{\mathrm{d}^2}{\mathrm{d}t^2} \boldsymbol{t}_2 = -\ddot{\vartheta} \boldsymbol{t}_1 - \dot{\vartheta}^2 \boldsymbol{t}_2 \,, \tag{2.43}$$

which follows directly from (2.9), and

$$\boldsymbol{t}_1 \times \boldsymbol{t}_2 = \boldsymbol{t}_3 \equiv \boldsymbol{e}_3 \,. \tag{2.44}$$

Using (2.39) and (2.42) in (2.29), and by virtue of the du Bois–Reymond lemma, we arrive at the balance of angular momentum in local resultant form

$$\boxed{I_\rho \ddot{\vartheta} \boldsymbol{e}_3 = \frac{\partial \boldsymbol{m}}{\partial X^1} + \frac{\partial \boldsymbol{\Phi}_0}{\partial X^1} \times \boldsymbol{f} + \boldsymbol{m}_\Gamma \, .} \tag{2.45}$$

For beams with fixed undeformed lengths, we refer the reader to [38] for a detailed literature review on the subject.

With the rotation angles defined in (2.7) and (2.8), and recalling that $\boldsymbol{f} = f^\alpha \boldsymbol{e}_\alpha$, $\boldsymbol{m} = m\boldsymbol{e}_3$, $\boldsymbol{m}_\Gamma = m_\Gamma \boldsymbol{e}_3$, etc., the equations of motion for sliding geometrically-exact beam in component form are summarized below

$$\boxed{\begin{aligned}
&\forall X^1 \in \,]C(t), L[: \\
&A_\rho(\ddot{u}_0^1 + \ddot{\mathscr{L}} \cos \vartheta_0) = \frac{\partial f^1}{\partial X^1} + f_\Gamma^1 \\
&A_\rho(\ddot{u}_0^2 + \ddot{\mathscr{L}} \sin \vartheta_0) = \frac{\partial f^2}{\partial X^1} + f_\Gamma^2 \\
&I_\rho \ddot{\vartheta} = I_\rho(\ddot{\theta} + \ddot{\psi}) = \frac{\partial m}{\partial X^1} + \left(\frac{\partial \boldsymbol{\Phi}_0}{\partial X^1} \times \boldsymbol{f} \right) \cdot \boldsymbol{e}_3 + m_\Gamma
\end{aligned}} \tag{2.46}$$

with the clamped (essential) boundary conditions at $X^1 = C(t)$

$$\boxed{\begin{aligned}
&u_0^1(C(t), t) = 0 \, , \\
&u_0^2(C(t), t) = 0 \, , \\
&\theta(C(t), t) = 0 \, , \qquad \text{or} \qquad \vartheta(C(t), t) = \vartheta_0 + \psi(t)
\end{aligned}} \tag{2.47}$$

where it should be noted that the deformation angle θ is used to specify the clamped boundary condition, and not the angle $\Delta\vartheta$, which includes the rigid body rotation angle ψ. Alternatively, if ϑ is chosen as a primary unknown function—which is the case in our computational formulation and implementation to be discussed in Section 4—then the clamped boundary condition is imposed if ϑ is equal to the rigid body rotation angle $(\vartheta_0 + \psi)$ as indicated in $(2.47)_3$. At $X^1 = L$, the beam tip is subjected to the free (natural) boundary conditions

$$\boxed{\begin{aligned}
&f^1(L, t) = 0 \, , \\
&f^2(L, t) = 0 \, , \\
&m(L, t) = 0 \, .
\end{aligned}} \tag{2.48}$$

REMARK 2.3. By following the above development, one obtains the equations of motion for 3-D sliding geometrically-exact beams below

$$\boxed{\begin{aligned}
&\forall X^1 \in \,]C(t), L[: \\
&A_\rho(\ddot{\boldsymbol{u}}_0 + \ddot{\mathscr{L}} \boldsymbol{E}_1) = \frac{\partial \boldsymbol{f}}{\partial X^1} + \boldsymbol{f}_\Gamma \, , \\
&\boldsymbol{I}_\rho \dot{\boldsymbol{w}} + \boldsymbol{w} \times \boldsymbol{I}_\rho \boldsymbol{w} = \frac{\partial \boldsymbol{m}}{\partial X^1} + \frac{\partial \boldsymbol{\Phi}_0}{\partial X^1} \times \boldsymbol{f} + \boldsymbol{m}_\Gamma \, .
\end{aligned}} \tag{2.49}$$

where $\boldsymbol{w}$ is the angular velocity of the cross section basis vectors $\boldsymbol{t}_i$, for $i = 1, 2, 3$,

$$\dot{\boldsymbol{t}}_i(X^1, t) = \boldsymbol{w} \times \boldsymbol{t}_i(X^1, t) . \tag{2.50}$$

The reader is referred to [44] for more details on the case of beams with fixed undeformed lengths. □

2.3. Equations of motion in stretched coordinate

The equations of motion (2.46) for 2-D sliding geometrically-exact beams are defined on the time-varying material domain $]C(t), L[$. We could devise algorithms that account for time-varying domain to solve (2.46). Evidently, these algorithms must contain the update of the domain with time. There is a number of ways to deal with time-varying domain: Keeping the same number of finite elements, but having the element length changing in time, or increasing with time the number of elements, whose length has an upper limit, etc. There are certainly some complications that must be addressed in the implementation of such algorithms regarding the data structure and data flow when using conventional finite element codes.

To circumvent these difficulties, our approach in the present section is to transform the equations of motion (2.46) to a constant domain by introducing a 'stretched' coordinate. Consider the following *constant* domain

$$\tilde{\mathscr{B}}_0 := \{(\xi^1, \xi^2) \in \mathbb{R}^2 \mid \xi^1 \in]0, 1[, \xi^2 \in]-h, h[\} . \tag{2.51}$$

Let $\xi = (\xi^1, \xi^2) \in \tilde{\mathscr{B}}_0$ be the image of the material point $X = (X^1, X^2) \in \bar{\mathscr{B}}_t$ by the mapping $\phi : \bar{\mathscr{B}}_t \to \tilde{\mathscr{B}}_0$ defined as follows: $\xi = \phi(X, t)$, and

$$\begin{cases} \xi^1 = \phi^1(X, t) = \dfrac{X^1 - C(t)}{\mathscr{L}(t)} = 1 + \dfrac{X^1 - L}{\mathscr{L}(t)} & \in]0, 1[, \\ \xi^2 = \phi^2(X, t) = X^2 & \in]-h, h[. \end{cases} \tag{2.52}$$

In other words, instead of parameterizing the material body $\bar{\mathscr{B}}_t$ using the coordinates (X^1, X^2), we use the coordinates (ξ^1, ξ^2). The same material point $X \in \bar{\mathscr{B}}_t$ can now be described by two coordinate systems (X^1, X^2) and (ξ^1, ξ^2), which are related to each other as in (2.52), or equivalently, with $\phi^{-1} : \tilde{\mathscr{B}}_0 \to \bar{\mathscr{B}}_t$ defined as

$$\begin{cases} X^1 = C(t) + \mathscr{L}(t)\xi^1 & \in]C(t), L[, \\ X^2 = \xi^2 & \in]-h, h[. \end{cases} \tag{2.53}$$

Since the coordinate ξ^1 belongs to a fixed interval $]0, 1[$ for all time t, it is also referred to as the 'stretched' coordinate, with $\mathscr{L}(t)$ as the stretching factor, representing the ratio between the old coordinate X^1 and the new coordinate ξ^1,

$$\mathscr{L}(t) = \frac{X^1 - L}{\xi^1 - 1} . \tag{2.54}$$

We use the superposed tilde on functions that have (X, t) as arguments to indicate that the arguments for these functions are now (ξ, t)

$$\tilde{(\cdot)}(\xi^1, t) \equiv \tilde{(\cdot)}(\phi^1(X^1, t), t) := (\cdot)(X^1, t) . \tag{2.55}$$

Thus, for example

$$\tilde{\boldsymbol{u}}_0(\xi^1, t) \equiv \tilde{\boldsymbol{u}}_0(\phi^1(X^1, t), t) := \boldsymbol{u}_0(X^1, t) , \tag{2.56}$$

$$\tilde{\vartheta}(\xi^1, t) \equiv \tilde{\vartheta}(\phi^1(X^1, t), t) := \vartheta(X^1, t) , \tag{2.57}$$

and similarly for other relevant functions. The time derivatives in the equations of motion (2.46) must now be interpreted as the material time derivatives, keeping the material point X fixed. Thus, in terms of the new variable ξ^1, the balance of momenta (2.38) and (2.45) become

$$\forall \xi^1 \in]0,1[\,,$$

$$A_\rho \left\{ \frac{\partial^2 \tilde{\boldsymbol{u}}_0}{(\partial \xi^1)^2} (\dot{\phi}^1)^2 + 2 \frac{\partial^2 \tilde{\boldsymbol{u}}_0}{\partial \xi^1 \partial t} \dot{\phi}^1 + \frac{\partial \tilde{\boldsymbol{u}}_0}{\partial \xi^1} \ddot{\phi}^1 + \frac{\partial^2 \tilde{\boldsymbol{u}}_0}{\partial t^2} + \ddot{\mathscr{L}} \boldsymbol{E}_1 \right\} = \frac{\partial \tilde{\boldsymbol{f}}}{\partial \xi^1} \frac{\partial \phi^1}{\partial X^1} + \tilde{\boldsymbol{f}}_\Gamma\,, \tag{2.58}$$

$$I_\rho \left\{ \frac{\partial^2 \tilde{\vartheta}}{(\partial \xi^1)^2} (\dot{\phi}^1)^2 + 2 \frac{\partial^2 \tilde{\vartheta}}{\partial \xi^1 \partial t} \dot{\phi}^1 + \frac{\partial \tilde{\vartheta}}{\partial \xi^1} \ddot{\phi}^1 + \frac{\partial^2 \tilde{\vartheta}}{\partial t^2} \right\} \boldsymbol{e}_3 = \frac{\partial \tilde{\boldsymbol{m}}}{\partial \xi^1} \frac{\partial \phi^1}{\partial X^1} + \left(\frac{\partial \tilde{\boldsymbol{\Phi}}_0}{\partial \xi^1} \frac{\partial \phi^1}{\partial X^1} \right) \times \tilde{\boldsymbol{f}} + \tilde{\boldsymbol{m}}_\Gamma\,. \tag{2.59}$$

Elementary manipulations on (2.52) yield the following relations

$$\frac{\partial \phi^1}{\partial X^1} = \frac{1}{\mathscr{L}}\,, \tag{2.60}$$

$$\dot{\phi}^1 := \frac{\partial \phi^1}{\partial t} = \frac{(1-\xi^1)}{\mathscr{L}} \dot{\mathscr{L}}\,, \tag{2.61}$$

$$\ddot{\phi}^1 := \frac{\partial^2 \phi^1}{\partial t^2} = \frac{\{(1-\xi^1)\ddot{\mathscr{L}} - \dot{\mathscr{L}}\dot{\xi}^1\}\mathscr{L} - (1-\xi^1)(\dot{\mathscr{L}})^2}{\mathscr{L}^2}\,. \tag{2.62}$$

Substituting (2.60)–(2.62) into (2.58) and (2.59), and multiplying the resulting equations throughout by $\mathscr{L}^2$ to avoid numerical difficulty when the (undeformed) length $\mathscr{L}(t)$ of the beam outside the channel gets close to zero, we obtain the following full Lagrangian equations of motion in stretched coordinate.

Axial and transversal motion: $\forall \xi^1 \in]0,1[$

$$\boxed{\begin{aligned} A_\rho \Bigg\{ & \underbrace{\frac{\partial}{\partial \xi^1} \left[(1-\xi^1)^2 \dot{\mathscr{L}}^2 \frac{\partial \tilde{\boldsymbol{u}}_0}{\partial \xi^1} \right]}_{(\mathrm{I})} + \underbrace{2(1-\xi^1)\mathscr{L}\dot{\mathscr{L}} \frac{\partial^2 \tilde{\boldsymbol{u}}_0}{\partial \xi^1 \partial t}}_{(\mathrm{II})} + \underbrace{(1-\xi^1)\mathscr{L}\ddot{\mathscr{L}} \frac{\partial \tilde{\boldsymbol{u}}_0}{\partial \xi^1}}_{(\mathrm{III})} + \underbrace{\mathscr{L}^2 \frac{\partial^2 \tilde{\boldsymbol{u}}_0}{\partial t^2}}_{(\mathrm{IV})} + \underbrace{\mathscr{L}^2 \ddot{\mathscr{L}} \boldsymbol{E}_1}_{(\mathrm{V})} \Bigg\} \\ & = \mathscr{L} \frac{\partial \tilde{\boldsymbol{f}}}{\partial \xi^1} + \mathscr{L}^2 \tilde{\boldsymbol{f}}_\Gamma\,, \end{aligned}} \tag{2.63}$$

Flexural motion: $\forall \xi^1 \in]0,1[$

$$\boxed{\begin{aligned} I_\rho \Bigg\{ & \underbrace{\frac{\partial}{\partial \xi^1} \left[(1-\xi^1)^2 \dot{\mathscr{L}}^2 \frac{\partial \tilde{\vartheta}}{\partial \xi^1} \right]}_{(\mathrm{I})} + \underbrace{2(1-\xi^1)\mathscr{L}\dot{\mathscr{L}} \frac{\partial^2 \tilde{\vartheta}}{\partial \xi^1 \partial t}}_{(\mathrm{II})} + \underbrace{(1-\xi^1)\mathscr{L}\ddot{\mathscr{L}} \frac{\partial \tilde{\vartheta}}{\partial \xi^1}}_{(\mathrm{III})} + \underbrace{\mathscr{L}^2 \frac{\partial^2 \tilde{\vartheta}}{\partial t^2}}_{(\mathrm{IV})} \Bigg\} \\ & = \mathscr{L} \frac{\partial \tilde{m}}{\partial \xi^1} + \mathscr{L} \left(\frac{\partial \tilde{\boldsymbol{\Phi}}_0}{\partial \xi^1} \times \tilde{\boldsymbol{f}} \right) \cdot \boldsymbol{e}_3 + \mathscr{L}^2 \tilde{m}_\Gamma\,. \end{aligned}} \tag{2.64}$$

REMARK 2.4. Some rearrangements of terms had been made to obtain the convective terms (I) in the inertia operators of (2.63) and (2.64); these terms will lead to symmetric matrices—in addition to the symmetric matrices resulting from the regular mass terms (IV)—in a Galerkin projection of (2.63)–(2.64). On the other hand, anti-symmetric matrices will result from the convective terms (II) and (III). The fact that we obtain gyroscopic-like anti-symmetry matrices in a (sliding) cantilever beam is a nice feature of the present formulation (see Section 4 for more details). The term (V) in (2.63) is a forcing term. □

REMARK 2.5. It is shown in [35] that by referring the dynamics of geometrically-exact beams in planar motion directly to the inertial frame, the inertia operators become simple, and are devoid of the non-linear, coupling terms that result from referring the dynamics to a floating reference frame or a shadow beam. Even though there are still convective terms due to the sliding motion and the use of a stretched coordinate, the inertia operators in (2.63) and in (2.64) remain linear and uncoupled, because the dynamics is referred to the inertial frame. The use of a shadow beam to describe the dynamics of sliding beams will introduce non-linear, coupling terms in the inertia operators, in addition to the convective terms due to the sliding motion and the use of a stretched coordinate. □

The boundary conditions in the ξ^1 coordinate equivalent to (2.47)–(2.48) are (see also Remark 3.2) At $\xi^1 = 0$:

$$\boxed{\begin{aligned} &\tilde{\boldsymbol{u}}_0(0,t) = \boldsymbol{0}\,, \\ &\tilde{\vartheta}(0,t) = \vartheta_0 + \psi(t)\,. \end{aligned}} \tag{2.65}$$

At $\xi^1 = 1$:

$$\boxed{\begin{aligned} &\tilde{\boldsymbol{f}}(1,t) = \boldsymbol{0}\,, \\ &\tilde{m}(1,t) = 0\,. \end{aligned}} \tag{2.66}$$

REMARK 2.6. A feature of the full Lagrangian formulation is the forcing term (V) in (2.63); this term can be called the material-axial-inertia force due to the sliding motion, because this force remains directed along the axis $\boldsymbol{E}_1$ of the (initial undeformed) material configuration, even though the sliding beam can undergo large angle maneuvers. □

We now need to relate the internal resultant force and moment ($\tilde{\boldsymbol{f}}$ and $\tilde{m}$) to the displacement $\tilde{\boldsymbol{u}}_0$ and the rotation $\tilde{\vartheta}$, which are the three primary unknown functions via the strain measures. The strain measure $\boldsymbol{\gamma}(X^1,t) = \gamma^\alpha(X^1,t)\boldsymbol{e}_\alpha$, employed in [35] and defined as follows

$$\boldsymbol{\gamma}(X^1,t) := \frac{\partial \boldsymbol{\Phi}_0(X^1,t)}{\partial X^1} - \boldsymbol{t}_1(X^1,t)\,, \tag{2.67}$$

now takes the following form in terms of the stretched coordinate ξ^1

$$\boxed{\begin{aligned} \tilde{\boldsymbol{\gamma}}(\xi^1,t) &= \frac{\partial \tilde{\boldsymbol{\Phi}}_0(\phi^1(X^1,t),t)}{\partial X^1} - \tilde{\boldsymbol{t}}_1(\xi^1,t) = \boldsymbol{E}_1 + \frac{\partial \tilde{\boldsymbol{u}}_0^1}{\partial \xi^1}\frac{\partial \phi^1}{\partial X^1} - \tilde{\boldsymbol{t}}_1\,, \\ &= \left[\cos\vartheta_0 + \frac{1}{\mathscr{L}}\frac{\partial \tilde{u}_0^1}{\partial \xi^1} - \cos\tilde{\vartheta}\right]\boldsymbol{e}_1 + \left[\sin\vartheta_0 + \frac{1}{\mathscr{L}}\frac{\partial \tilde{u}_0^2}{\partial \xi^1} - \sin\tilde{\vartheta}\right]\boldsymbol{e}_2\,, \end{aligned}} \tag{2.68}$$

where $\tilde{\boldsymbol{\gamma}}$ and $\tilde{\boldsymbol{t}}_\alpha$ are related to $\boldsymbol{\gamma}$ and $\boldsymbol{t}_\alpha$ as indicated in (2.55), and $\partial\phi^1/\partial X^1$ as given in (2.60). Similarly, the curvature in the ξ^1 coordinate is given by

$$\boxed{\tilde{\kappa}(\xi^1,t) = \frac{\partial \tilde{\vartheta}(\phi^1(X^1,t),t)}{\partial X^1} = \frac{\partial \tilde{\vartheta}}{\partial \xi^1}\frac{\partial \phi^1}{\partial X^1}\,.} \tag{2.69}$$

With the matrix of beam section stiffness coefficients denoted by

$$\boldsymbol{\mathscr{C}} = \mathscr{C}^\alpha_\beta \boldsymbol{E}_\alpha \otimes \boldsymbol{E}^\beta\,, \qquad \text{with } [\mathscr{C}^\alpha_\beta] = \begin{bmatrix} EA & 0 \\ 0 & GA_s \end{bmatrix} \in \mathbb{R}^{2\times 2}\,, \tag{2.70}$$

where EA is the section axial stiffness and GA_s the section shear stiffness, we postulate the following constitutive law relating $\tilde{\boldsymbol{f}}$ to $\tilde{\boldsymbol{\gamma}}$ (see [35])

$$\boxed{\tilde{\boldsymbol{f}} = \tilde{\boldsymbol{\Lambda}} \cdot \boldsymbol{\mathscr{C}} \cdot \tilde{\boldsymbol{\Lambda}}^{\mathrm{T}} \cdot \tilde{\boldsymbol{\gamma}}\,,} \tag{2.71}$$

where the rotation tensor $\tilde{\boldsymbol{\Lambda}}$ is defined similar to (2.9)–(2.10)

$$\tilde{\boldsymbol{\Lambda}} = \tilde{\Lambda}^{\alpha}_{\beta} \boldsymbol{e}_{\alpha} \otimes \boldsymbol{E}^{\beta} , \qquad \text{such that} \qquad \tilde{\boldsymbol{t}}_{\beta} := \tilde{\boldsymbol{\Lambda}} \cdot \boldsymbol{E}_{\beta} = \tilde{t}^{\alpha}_{\beta} \boldsymbol{e}_{\alpha} . \tag{2.72}$$

$$[\tilde{\Lambda}^{\alpha}_{\beta}] = \begin{bmatrix} \cos \tilde{\vartheta} & -\sin \tilde{\vartheta} \\ \sin \tilde{\vartheta} & \cos \tilde{\vartheta} \end{bmatrix} \in \mathbb{R}^{2 \times 2} . \tag{2.73}$$

In component form and in matrix notation, (2.71) reads as follows[14]

$$\tilde{f}^{\alpha} = \tilde{\Lambda}^{\alpha}_{\beta} \mathscr{C}^{\beta}_{\sigma} \tilde{\Lambda}^{\tau}_{\sigma} \tilde{\gamma}^{\tau} , \tag{2.74}$$

$$\{\tilde{f}^{\alpha}\} = [\tilde{\Lambda}^{\alpha}_{\beta}][\mathscr{C}^{\beta}_{\sigma}][\tilde{\Lambda}^{\sigma}_{\tau}]^{\mathrm{T}}\{\tilde{\gamma}^{\tau}\} \in \mathbb{R}^{2 \times 1} , \tag{2.75}$$

respectively. Let EI denote the section bending stiffness; we postulate the following relation between the internal moment $\tilde{m}$ and the curvature $\tilde{\kappa}$

$$\boxed{\tilde{m} = EI \tilde{\kappa} .} \tag{2.76}$$

In summary, the balance equations (2.63)–(2.64), in terms of the stretched coordinate ξ^1 on constant domain $[0, 1]$, together with the relations between the internal stress resultants/couple and the primary unknown functions $\{\tilde{u}^1_0, \tilde{u}^2_0, \tilde{\vartheta}\}$—i.e. relations (2.71) and (2.68), (2.76) and (2.69)—yield the partial differential equations (PDEs) governing the motion of sliding geometrically-exact beams. These PDEs together with the boundary conditions (2.65)–(2.66), and appropriate initial conditions, form a complete mathematical statement for the sliding beam problem considered herein.

Next we will discuss an alternative, but equivalent, formulation for the equations governing the motion of sliding geometrically-exact beams.

3. Alternative approach: Eulerian–Lagrangian formulation

An advantage of restricting the dynamic formulation for sliding beams—viewed as systems with changing mass—to the part outside the joints, is that the formulation remains valid regardless of what happens inside the joint. The formulation presented in Section 2—which can be considered as a full Lagrangian formulation—does possess this advantage, even though we did prescribe 'harmless' assumptions on the beam kinematics (not kinetics) inside the joint.[15] The resulting governing equations (2.63)–(2.64) involve strictly kinematic quantities outside the joint channel.

Instead of the full Lagrangian viewpoint, we present here an Eulerian–Lagrangian viewpoint—which is a 'natural' way to formulate the sliding beam problem as mentioned at the beginning of Section 2—via the introduction of an intermediate configuration between the material (undeformed) configuration and the current (deformed) configuration. This intermediate configuration plays the role of an Eulerian domain with respect to the sliding undeformed beam, and the role of a Lagrangian domain with respect to the beam deformation to the current configuration. We thus distinguish the intermediate configuration—which is *fixed* in the spatial frame—from the sliding undeformed beam, which is translating in the spatial frame. The intermediate configuration has, however, time-varying boundary determined by the tip of the sliding undeformed beam.

3.1. Intermediate configuration

Recall that the material configuration $\mathscr{B}_0$ in (2.1) is chosen to be the same as the initial undeformed configuration; see Fig. 3. The intermediate configuration, denoted by $\hat{\mathscr{B}}_t$, is parameterized by the

---

[14] Strictly speaking, $\tilde{\boldsymbol{\Lambda}}^{-1} = (\tilde{\boldsymbol{\Lambda}}^{-1})^{\alpha}_{\beta} \boldsymbol{E}_{\alpha} \otimes \boldsymbol{e}^{\beta}$, where $[(\tilde{\boldsymbol{\Lambda}}^{-1})^{\alpha}_{\beta}] = [\tilde{\Lambda}^{\alpha}_{\beta}]^{-1}$. Since $[\tilde{\Lambda}^{\alpha}_{\beta}]$ is an orthogonal matrix, we have $[\tilde{\Lambda}^{\alpha}_{\beta}]^{-1} = [\tilde{\Lambda}^{\alpha}_{\beta}]^{\mathrm{T}}$, i.e. $(\tilde{\Lambda}^{-1})^{\alpha}_{\beta} = \tilde{\Lambda}^{\beta}_{\alpha}$. On the other hand, $\tilde{\boldsymbol{\Lambda}}^{\mathrm{T}} = G^{\alpha\tau} \tilde{\Lambda}^{\sigma}_{\tau} g_{\sigma\beta} \boldsymbol{E}_{\alpha} \otimes \boldsymbol{e}^{\beta}$. For Cartesian coordinates, $G^{\alpha\tau} = \delta^{\alpha\tau}$ and $g_{\sigma\beta} = \delta_{\sigma\beta}$, thus leading to the identification $\tilde{\boldsymbol{\Lambda}}^{-1} = \tilde{\Lambda}^{\beta}_{\alpha} \boldsymbol{E}_{\alpha} \otimes \boldsymbol{e}^{\beta} = \tilde{\boldsymbol{\Lambda}}^{\mathrm{T}}$.

[15] The formulation is of a displacement-driven type; thus, the kinetics of the beam part inside the channel is of no consequence anyway.

coordinates (χ^1, χ^2), which are parallel to the coordinates (X^1, X^2), and having the orthonormal basis vectors $(\mathscr{E}_1, \mathscr{E}_2)$, such that $\mathscr{E}_\alpha \equiv \boldsymbol{E}_\alpha$. The origin of the coordinates (χ^1, χ^2) is chosen to be at the channel orifice, i.e. m at the origin O_x of the spatial (inertial) coordinates;[16] we have

$$\check{\mathscr{B}}_t := \{(\chi^1, \chi^2) \in \mathbb{R}^2 \mid \chi^1 \in\,]0, \mathscr{L}(t)[,\ \chi^2 \in\,]-h, h[\} . \tag{3.1}$$

The intermediate configuration $\check{\mathscr{B}}_t$ thus defined has a time-varying boundary.

The mapping from the material configuration $\bar{\mathscr{B}}_t$ to the intermediate configuration $\check{\mathscr{B}}_t$, denoted by φ, is a sliding rigid body motion along the channel axis. Consider a point $\chi = (\chi^1, \chi^2)$ *fixed* in $\check{\mathscr{B}}_t$; therefore χ is also *inertially fixed*. The Eulerian description of the motion of the sliding undeformed beam is as follows: The point $\chi = (\chi^1, \chi^2) \in \check{\mathscr{B}}_t$ being *fixed* in the spatial (inertial) space—i.e. the coordinates (χ^1, χ^2) in (3.3) are constant in time—we look at the material points $X \in \bar{\mathscr{B}}_t$ that pass by and coincide with the point χ at various instants of time such that $\chi = \varphi(X, t)$. The sliding rigid body motion $\varphi : \bar{\mathscr{B}}_t \rightarrow \check{\mathscr{B}}_t$ is given by

$$\begin{cases} \chi^1 = \varphi^1(\chi, t) = X^1 + \mathscr{L}(t) - L\,, & X^1 \in\,]C(t), L[\\ \chi^2 = \varphi^2(\chi, t) = X^2\,, & X^2 \in\,]-h, h[\end{cases} \tag{3.2}$$

With respect to the spatial basis $(\boldsymbol{e}_1, \boldsymbol{e}_2)$, the position vector of the point χ is given by

$$\boldsymbol{\chi} := \chi - O_x = \chi^\alpha \mathscr{E}_\alpha = (\chi^1 \cos \vartheta_0 - \chi^2 \sin \vartheta_0)\boldsymbol{e}_1 + (\chi^1 \sin \vartheta_0 + \chi^2 \cos \vartheta_0)\boldsymbol{e}_2 . \tag{3.3}$$

The intermediate configuration $\check{\mathscr{B}}_t$ can be thought of as coincident with the part outside the channel of the sliding undeformed beam in Fig. 3. The motion of the beam tip of the sliding undeformed beam represents the time-varying boundary of the intermediate configuration $\check{\mathscr{B}}_t$.

Once we have defined the intermediate configuration $\check{\mathscr{B}}_t$ as above, the deformation map from $\check{\mathscr{B}}_t$ to the current configuration $\mathscr{B}_t$ is a Lagrangian description from the *inertially fixed* point $\chi \in \check{\mathscr{B}}_t$ to the spatial point $x \in \mathscr{B}_t$ in a similar manner as for geometrically-exact beams with fixed undeformed length, i.e.

$$x = \boldsymbol{\Phi}(X, t) = \underbrace{\chi_0 + \check{\boldsymbol{u}}_0(\chi^1, t)}_{\check{\boldsymbol{\Phi}}_0(\chi^1, t)} + \chi^2 \check{\boldsymbol{t}}_2(\chi^1, t)\,, \tag{3.4}$$

where $\chi_0 = (\chi^1, 0)$ is a point on the centroidal line of the intermediate configuration $\check{\mathscr{B}}_t$, having the position vector $\chi^1 \mathscr{E}_1$. Relating the above kinematic relations in the χ^α coordinates back to the material point $X = (X^1, X^2)$ that coincides with the point $\chi = (\chi^1, \chi^2)$ at the current instant of time, we can use the relation (3.2) together with the following identification: Similar to (2.55)–(2.57), a superposed check mark on a function having (X, t) as arguments indicates that this function now has (χ, t) as arguments such that

$$(\check{\cdot})(\chi^1, t) \equiv (\check{\cdot})(\varphi^1(X^1, t), t) := (\cdot)(X^1, t) . \tag{3.5}$$

For example

$$\check{\boldsymbol{u}}_0(\chi^1, t) \equiv \check{\boldsymbol{u}}_0(\varphi^1(X^1, t), t) := \boldsymbol{u}_0(X^1, t)\,, \tag{3.6}$$

$$\check{\vartheta}(\chi^1, t) \equiv \check{\vartheta}(\varphi^1(X^1, t), t) := \vartheta(X^1, t)\,, \tag{3.7}$$

and similarly for other relevant functions. The section basis vector $\check{\boldsymbol{t}}_2$ in (3.4) is related to the spatial basis vector $\boldsymbol{e}_2$ via the total rotation angle $\check{\vartheta}$ in the same manner as in (2.9)–(2.10),

$$\check{\boldsymbol{\Lambda}} = \check{\Lambda}^\alpha_\beta \boldsymbol{e}_\alpha \otimes \mathscr{E}^\beta\,, \qquad \text{such that} \qquad \check{\boldsymbol{t}}_\beta := \check{\boldsymbol{\Lambda}} \cdot \mathscr{E}_\beta = \check{t}^\alpha_\beta \boldsymbol{e}_\alpha\,, \tag{3.8}$$

---

[16] The channel orifice can have a prescribed motion in the inertial frame (see Remark 3.2 below). We assume at present that the channel orifice does not translate from, but can rotate about, the spatial observer O_x.

and

$$[\check{\Lambda}^\alpha_\beta] = \begin{bmatrix} \cos\check{\vartheta} & -\sin\check{\vartheta} \\ \sin\check{\vartheta} & \cos\check{\vartheta} \end{bmatrix} \in \mathbb{R}^{2\times 2} . \tag{3.9}$$

3.2. Eulerian–Lagrangian equations of motion

Consider a control volume $\Omega_t \subset \mathscr{B}_t$ as in the balance of linear and angular momenta (2.22)–(2.23), and a volume $\check{\Omega}_t \subset \check{\mathscr{B}}_t$ with normal $\check{\boldsymbol{N}} = \check{N}_i \mathscr{E}^i$ on the boundary $\partial\check{\Omega}_t$ such that

$$\Omega_t = \check{\Phi}(\check{\Omega}_t, t) . \tag{3.10}$$

Now, pulling the balance of linear and angular momenta (2.22)–(2.23) back to the intermediate configuration, we have the counterpart of (2.26)–(2.27), but for the intermediate configuration, as

$$\frac{\mathrm{d}}{\mathrm{d}t} \int_{\check{\Omega}_t} \check{\rho}\check{\boldsymbol{V}}\, \mathrm{d}(\check{\Omega}_t) = \int_{\partial\check{\Omega}_t} \check{\boldsymbol{N}} \cdot \check{\boldsymbol{P}}\, \mathrm{d}(\partial\check{\Omega}_t) + \int_{\check{\Omega}_t} \check{\rho}\check{\boldsymbol{B}}\, \mathrm{d}(\check{\Omega}_t) \quad \forall \check{\Omega}_t \subset \check{\mathscr{B}}_t , \tag{3.11}$$

$$\frac{\mathrm{d}}{\mathrm{d}t} \int_{\check{\Omega}_t} \check{\rho}\check{\boldsymbol{\Phi}} \times \check{\boldsymbol{V}}\, \mathrm{d}(\check{\Omega}_t) = \int_{\partial\check{\Omega}_t} \check{\boldsymbol{\Phi}} \times (\check{\boldsymbol{N}} \cdot \check{\boldsymbol{P}})\, \mathrm{d}(\partial\check{\Omega}_t) + \int_{\check{\Omega}_t} \check{\boldsymbol{\Phi}} \times \check{\rho}\check{\boldsymbol{B}}\, \mathrm{d}(\check{\Omega}_t) \quad \forall \check{\Omega}_t \subset \check{\mathscr{B}}_t , \tag{3.12}$$

where $\check{\boldsymbol{P}} = \mathscr{E}_i \otimes \check{\boldsymbol{T}}^i$ is the first Piola–Kirchhoff stress tensor based on the intermediate configuration, $\check{\rho}(\chi, t) = \rho(x, t)\check{J}(\chi, t)$ the mass density per unit volume of $\check{\mathscr{B}}_t$, with $\check{J}(\chi, t)$ being the Jacobian determinant of the deformation map $\check{\Phi}$, $\check{\boldsymbol{B}}(\chi, t) = \boldsymbol{b}(x, t)$ the body force,[17] $\check{\boldsymbol{V}}$ the spatial velocity field covering the deformation map $\check{\Phi}$ (i.e. parameterized on the intermediate configuration) defined as (cf. (2.24))

$$\check{\boldsymbol{V}}(\chi, t) \equiv \boldsymbol{v}(x, t) \equiv \boldsymbol{V}(X, t) , \tag{3.13}$$

and $\check{\boldsymbol{\Phi}}$ the spatial position vector with respect to the observer O_x

$$\check{\boldsymbol{\Phi}} = x - O_x = \check{\Phi} - O_x . \tag{3.14}$$

The spatial velocity field $\check{\boldsymbol{V}}$ is the material time derivative of $\check{\Phi}$, keeping to the material point X—such that $\chi = \varphi(X, t)$—fixed

$$\check{\boldsymbol{V}}(\chi, t) = \frac{\mathrm{D}}{\mathrm{D}t} \check{\Phi}(\chi, t) = \frac{\mathrm{d}}{\mathrm{d}t} \check{\Phi}(\varphi(X, t), t) = \frac{\partial\check{\Phi}}{\partial\chi^i} \frac{\partial\varphi^i}{\partial t} + \frac{\partial\check{\Phi}}{\partial t} . \tag{3.15}$$

Consider a material domain $\Omega_0 \in \mathscr{B}_0$ such that

$$\check{\Omega}_t = \varphi(\Omega_0, t) , \tag{3.16}$$

with φ defined in (3.2) as the sliding rigid body motion. Then by standard procedure,[18] the time rate of the linear and angular momenta in (3.11)–(3.12) is given by

$$\frac{\mathrm{d}}{\mathrm{d}t} \int_{\check{\Omega}_t} \check{\rho}\check{\boldsymbol{V}}\, \mathrm{d}(\check{\Omega}_t) = \int_{\check{\Omega}_t} \check{\rho} \frac{\mathrm{D}^2\check{\Phi}}{\mathrm{D}t^2}\, \mathrm{d}(\check{\Omega}_t) , \tag{3.17}$$

$$\frac{\mathrm{d}}{\mathrm{d}t} \int_{\check{\Omega}_t} \check{\rho}\check{\boldsymbol{\Phi}} \times \check{\boldsymbol{V}}\, \mathrm{d}(\check{\Omega}_t) = \int_{\check{\Omega}_t} \check{\rho}\check{\boldsymbol{\Phi}} \times \frac{\mathrm{D}^2\check{\Phi}}{\mathrm{D}t^2}\, \mathrm{d}(\check{\Omega}_t) . \tag{3.18}$$

From the sliding motion φ as defined in (3.2), it follows from (3.15) that

$$\frac{\mathrm{D}\check{\Phi}}{\mathrm{D}t} = \frac{\partial\check{\Phi}}{\partial\chi^1} \frac{\partial\varphi^1}{\partial t} + \frac{\partial\check{\Phi}}{\partial t} = \frac{\partial\check{\Phi}}{\partial\chi^1} \dot{\mathscr{L}} + \frac{\partial\check{\Phi}}{\partial \mathrm{t}} , \tag{3.19}$$

---

[17] $\check{\boldsymbol{B}}(\chi, t)$ is the *spatial* body force, parameterized on the intermediate configuration.

[18] I.e., pulling the integrals on the right-hand sides of (3.11)–(3.12) back to Ω_0, taking the time derivative, and push forward the resulting integrals to $\check{\Omega}_t$ (see [43]).

$$\frac{\mathrm{D}^2\check{\boldsymbol{\Phi}}}{\mathrm{D}t^2}=\frac{\partial^2\check{\boldsymbol{\Phi}}}{(\partial\chi^1)^2}(\dot{\mathscr{L}})^2+\frac{\partial\check{\boldsymbol{\Phi}}}{\partial\chi^1}\ddot{\mathscr{L}}+2\frac{\partial^2\check{\boldsymbol{\Phi}}}{\partial\chi^1\,\partial t}\dot{\mathscr{L}}+\frac{\partial^2\check{\boldsymbol{\Phi}}}{\partial t^2}\,. \tag{3.20}$$

Now, following essentially the same argument as for the full Lagrangian formulation in Section 2, we arrive at the following governing PDEs for the Eulerian–Lagrangian formulation $\forall\chi^1\in\,]0,\mathscr{L}(t)[$,

$$\boxed{\begin{aligned}&\check{A}_\rho\left\{\frac{\partial^2\check{\boldsymbol{u}}_0}{(\partial\chi^1)^2}(\dot{\mathscr{L}})^2+2\frac{\partial^2\check{\boldsymbol{u}}_0}{\partial\chi^1\,\partial t}\dot{\mathscr{L}}+\frac{\partial\check{\boldsymbol{u}}_0}{\partial\chi^1}\ddot{\mathscr{L}}+\frac{\partial^2\check{\boldsymbol{u}}_0}{\partial t^2}\right\}=\frac{\partial\check{\boldsymbol{f}}}{\partial\chi^1}+\check{\boldsymbol{f}}_\Gamma\,,\\&\check{I}_\rho\left\{\frac{\partial^2\check{\vartheta}}{(\partial\chi^1)^2}(\dot{\mathscr{L}})^2+2\frac{\partial^2\check{\vartheta}}{\partial\chi^1\,\partial t}\dot{\mathscr{L}}+\frac{\partial\check{\vartheta}}{\partial\chi^1}\ddot{\mathscr{L}}+\frac{\partial^2\check{\vartheta}}{\partial t^2}\right\}\boldsymbol{e}_3=\frac{\partial\check{\boldsymbol{m}}}{\partial\chi^1}+\frac{\partial\check{\boldsymbol{\Phi}}_0}{\partial\chi^1}\times\check{\boldsymbol{f}}+\check{\boldsymbol{m}}_\Gamma\,,\end{aligned}} \tag{3.21}$$

where the inertia operators had been particularized to planar sliding motion, with[19]

$$\check{A}_\rho:=\int_{\mathscr{A}_0}\check{\rho}\,\mathrm{d}\mathscr{A}_0\,,\qquad\check{I}_\rho:=\int_{\mathscr{A}_0}(\chi^2)^2\check{\rho}\,\mathrm{d}\mathscr{A}_0\,, \tag{3.22}$$

and with the position vector $\check{\boldsymbol{\Phi}}_0$ and the displacement vector $\check{\boldsymbol{u}}_0$ of the centroidal line related to each other as indicated in (3.4); the stress resultant $\check{\boldsymbol{f}}$ and stress couple $\check{\boldsymbol{m}}$ are defined similar to (2.20)–(2.21)

$$\check{\boldsymbol{f}}(\chi^1,t):=\int_{\mathscr{A}_0}\check{\boldsymbol{T}}^1\,\mathrm{d}\mathscr{A}_0\,,\qquad\check{\boldsymbol{m}}(\chi^1,t):=\int_{\mathscr{A}_0}\chi^2\check{\boldsymbol{t}}_2\times\check{\boldsymbol{T}}^1\,\mathrm{d}\mathscr{A}_0\,; \tag{3.23}$$

the applied stress resultant $\check{\boldsymbol{f}}_\Gamma$ and applied stress couple $\check{\boldsymbol{m}}_\Gamma$ are defined similar to (2.35) and to (2.40), respectively

$$\check{\boldsymbol{f}}_\Gamma:=\int_{\partial\mathscr{A}_0}[\check{N}_2\check{\boldsymbol{T}}^2+\check{N}_3\check{\boldsymbol{T}}^3]\,\mathrm{d}(\partial\mathscr{A}_0)+\int_{\mathscr{A}_0}\check{\rho}\check{\boldsymbol{B}}\,\mathrm{d}\mathscr{A}_0\,, \tag{3.24}$$

$$\check{\boldsymbol{m}}_\Gamma:=\int_{\partial\mathscr{A}_0}(\check{\boldsymbol{\Phi}}-\check{\boldsymbol{\Phi}}_0)\times\left[\sum_{\alpha=2}^{3}\check{N}_\alpha\check{\boldsymbol{T}}^\alpha\right]\mathrm{d}(\partial\mathscr{A}_0)+\int_{\mathscr{A}_0}(\check{\boldsymbol{\Phi}}-\check{\boldsymbol{\Phi}}_0)\times\check{\rho}\check{\boldsymbol{B}}\,\mathrm{d}\mathscr{A}_0\,. \tag{3.25}$$

A similar procedure can be followed to obtain the equations for the 3-D sliding motion (see Remark 2.3).

REMARK 3.1. If ρ_{ref} is a constant, then so will be the mass per unit length $\check{A}_\rho$ and the section mass moment of inertia $\check{I}_\rho$ in the intermediate configuration. On the other hand, if ρ_{ref} is a function of X^1, then so will be A_ρ and I_ρ, while $\check{A}_\rho$ and $\check{I}_\rho$ will be functions of (χ^1,t). □

The boundary conditions in the χ^1 coordinate equivalent to (2.65)–(2.66) are (see also Remark 3.2)
At $\chi^1=0$:

$$\boxed{\begin{aligned}&\check{\boldsymbol{u}}_0(0,t)=0\,,\\&\check{\vartheta}(0,t)=\vartheta_0+\psi(t)\end{aligned}} \tag{3.26}$$

At $\chi^1=\mathscr{L}(t)$:

$$\boxed{\begin{aligned}&\check{\boldsymbol{f}}(\mathscr{L}(t),t)=0\,,\\&\check{\boldsymbol{m}}(\mathscr{L}(t),t)=0\,.\end{aligned}} \tag{3.27}$$

---

[19] By virtue $(3.2)_2$, we can identify the cross section $\mathscr{A}_t$ with $\mathscr{A}_0$.

REMARK 3.2. Of course the displacement boundary conditions in (2.47), (2.65) and (3.26) need not be zero, i.e. one can prescribe arbitrary displacement pattern for the channel

$$\boldsymbol{u}_0(C(t),t) = \tilde{\boldsymbol{u}}_0(0,t) = \check{\boldsymbol{u}}_0(0,t) = \hat{\boldsymbol{u}}_0(t)\,, \tag{3.28}$$

where $\hat{\boldsymbol{u}}_0(t)$ is some given function in time. Such prescription of the channel displacement can be used to simulate for example the translational motion of a robot manipulator arm or the orbital motion of a satellite. Likewise, one could consider to have a concentrated force $\hat{f}(t)$ and a concentrated couple $\hat{m}(t)$ applied at the beam tip, i.e.

$$f(L,t) = \tilde{f}(1,t) = \check{f}(\mathscr{L}(t),t) = \hat{f}(t)\,, \tag{3.29}$$

$$m(L,t) = \tilde{m}(1,t) = \check{m}(\mathscr{L}(t),t) = \hat{m}(t)\,, \tag{3.30}$$

instead of the free end conditions in (2.48), (2.66) and (3.27). □

In the coordinates (χ^1, χ^2) of the intermediate configuration $\check{\mathscr{B}}_t$, the strain measure $\boldsymbol{\gamma}$ as defined in (2.67) becomes

$$\boxed{\begin{aligned} \check{\boldsymbol{\gamma}}(\xi^1,t) &= \frac{\partial \check{\boldsymbol{\Phi}}_0(\varphi^1(X^1,t),t)}{\partial X^1} - \check{\boldsymbol{t}}_1(\chi^1,t) \\ &= \left[\cos\vartheta_0 + \frac{\partial \check{u}_0^1}{\partial \chi^1} - \cos\check{\vartheta}\right]\boldsymbol{e}_1 + \left[\sin\vartheta_0 + \frac{\partial \check{u}_0^2}{\partial \chi^1} - \sin\check{\vartheta}\right]\boldsymbol{e}_2\,, \end{aligned}} \tag{3.31}$$

since

$$\frac{\partial \varphi^1}{\partial X^1} = 1 \tag{3.32}$$

according to (3.5). Likewise, the curvature $\check{\kappa}$ is given by

$$\boxed{\check{\kappa}(\chi^1,t) = \frac{\partial \check{\vartheta}(\varphi^1(X^1,t),t)}{\partial X^1} = \frac{\partial \check{\vartheta}}{\partial \chi^1}\,.} \tag{3.33}$$

The expressions (3.31) for $\check{\boldsymbol{\gamma}}$ and (3.33) for $\check{\kappa}$ are the counterparts of $\tilde{\boldsymbol{\gamma}}$ in (2.68) and of $\tilde{\boldsymbol{\kappa}}$ in (2.69). The constitutive laws equivalent to (2.71) and (2.76) are

$$\boxed{\check{f} = \check{\Lambda}\cdot\mathscr{C}\cdot\check{\Lambda}^{\mathrm{T}}\cdot\check{\boldsymbol{\gamma}}\,,} \tag{3.34}$$

having the component form—based on (3.8)–(3.9)—similar to (2.74)–(2.75) and

$$\boxed{\check{m} = EI\check{\kappa}\,.} \tag{3.35}$$

In summary, the balance equations (3.21), in terms of the χ^1 coordinate of the intermediate configuration $\check{\mathscr{B}}_t$, together with the relations between the internal stress resultants/couple and the primary unknown functions $\{\check{u}_0^1, \check{u}_0^2, \check{\vartheta}\}$—i.e. relations (3.34) and (3.31), (3.35) and (3.33)—yield the partial differential equations (PDEs) governing the motion of sliding geometrically-exact beams. These PDEs together with the boundary conditions (3.26)–(3.27), and appropriate initial conditions, form a complete mathematical statement for the sliding beam problem considered herein.

3.3. Comparison of formulations

Of course, one expects that the full Lagrangian formulation and the Eulerian–Lagrangian formulation are equivalent in that the equations from one formulation can be transformed to those from the other. The (Lagrangian) deformation map $\Phi : \bar{\mathscr{B}}_t \rightarrow \mathscr{B}_t$ can be written as a composition of $\tilde{\Phi} : \tilde{\mathscr{B}}_0 \rightarrow \mathscr{B}_t$ with $\phi : \bar{\mathscr{B}}_t \rightarrow \tilde{\mathscr{B}}_0$ for the full Lagrangian formulation in stretched coordinate, i.e.

$$\Phi = \tilde{\Phi} \circ \phi : \bar{\mathscr{B}}_t \rightarrow \mathscr{B}_t \,, \tag{3.36}$$

and as a composition of $\check{\Phi} : \check{\mathscr{B}}_t \rightarrow \mathscr{B}_t$ with $\varphi : \bar{\mathscr{B}}_t \rightarrow \check{\mathscr{B}}_t$ for the Eulerian–Lagrangian formulation, i.e.

$$\Phi = \check{\Phi} \circ \varphi : \bar{\mathscr{B}}_t \rightarrow \mathscr{B}_t \,. \tag{3.37}$$

It follows from (3.36) and (3.37) that we can obtain $\check{\Phi}$ from $\tilde{\Phi}$, and vice versa, by

$$\tilde{\Phi} = \check{\Phi} \circ \varphi \circ \phi^{-1} = \Phi \circ \phi^{-1} : \tilde{\mathscr{B}}_0 \rightarrow \mathscr{B}_t \,, \tag{3.38}$$

$$\tilde{\Phi} = \tilde{\Phi} \circ \phi \circ \varphi^{-1} = \Phi \circ \varphi^{-1} : \check{\mathscr{B}}_t \rightarrow \mathscr{B}_t \,. \tag{3.39}$$

Thus, from (3.39), Eqs. (3.21) of the Eulerian–Lagrangian formulation can be obtained from Eqs. (2.46) of the full Lagrangian formulation by composing $\Phi : \bar{\mathscr{B}}_t \rightarrow \mathscr{B}_t$ with $\varphi^{-1} : \check{\mathscr{B}}_t \rightarrow \bar{\mathscr{B}}_t$ defined as (see (3.2))

$$\begin{cases} X^1 = \chi^1 - \mathscr{L}(t) + L \,, \\ X^2 = \chi^2 \,, \end{cases} \tag{3.40}$$

With $\varphi : \bar{\mathscr{B}}_t \rightarrow \check{\mathscr{B}}_t$ defined in (3.2) and $\phi^{-1} : \tilde{\mathscr{B}}_0 \rightarrow \bar{\mathscr{B}}_t$ defined in (2.53), the transformation $\varphi \circ \phi^{-1} : \tilde{\mathscr{B}}_0 \rightarrow \check{\mathscr{B}}_t$ defined as

$$\begin{cases} \chi^1 = \mathscr{L}(t)\xi^1 \,, \\ \chi^2 = \xi^2 \,, \end{cases} \tag{3.41}$$

when composed with $\check{\Phi} : \check{\mathscr{B}}_t \rightarrow \mathscr{B}_t$ as indicated in (3.38) will allow a recovery of the full Lagrangian equations in stretched coordinate (2.58)–(2.59) from the Eulerian–Lagrangian equations (3.21), and vice versa—i.e. (3.21) can be obtained from (2.58)–(2.59)—by virtue of (3.39).

Even though from the theoretical formulation standpoint, the governing equations for sliding geometrically-exact beams can have various equivalent forms as just indicated above, a comparison of the two formulations from the computational standpoint offers a markedly different picture. By discretizing the Eulerian–Lagrangian equations (3.21), one has to deal with a time-varying domain, thus affecting the data structure and the data flow in conventional finite element codes, similar to the case of the full Lagrangian equations (2.46) as already remarked at the beginning of Section 2.3. But then little can be gained by working with the Eulerian–Lagrangian equations (3.21) instead of the full Lagrangian equations (2.46): The Eulerian–Lagrangian equations contain convective terms; the full Lagrangian equations do not. In addition, as pointed out in Remark 3.1, the full Lagrangian formulation—particularly the one in stretched coordinate—offers a definite advantage over the others when the mass per unit length A_ρ and mass moment of inertia I_ρ are not uniform along the beam (undeformed) length (i.e. A_ρ and I_ρ are functions of X^1).

4. Algorithmic treatment of the full Lagrangian equations in stretched coordinate

In the present section, we discuss the Galerkin projection of the full Lagrangian equations (2.63)–(2.64) in terms of the stretched coordinate ξ^1, leading to a system of semi-discrete equations. The constancy of the domain of ξ^1 makes the computational algorithm simpler, as mentioned in Section 3.3. A post-processing is necessary to express the computational results back in the actual physical (spatial) space. The discrete inertia operator has a structure similar to that found in the equations describing the dual problem (see Section 1) of dynamic interaction between high-speed vehicles and flexible guideways

[4, 5]. Namely, the convective terms in the inertia operator lead to a velocity-convection term and the stiffness-convection term in the semi-discrete equations. In particular, an elegant feature of the present formulation is that the inertia operator can be decomposed into a symmetric (self-adjoint) part and an anti-symmetric (non-self-adjoint) part (see Remark 2.4), thus making the semi-discrete equations having a structure similar to those of a gyroscopic elastic system, even though there is no rotating, but only sliding, motion.

4.1. Weak form and decomposition of operators

We will consider first the common part of the inertia operators in (2.63)–(2.64), where it can be noticed that the second material time derivative of a function $(\tilde{\cdot})(\xi^1, t)$ as defined in (2.55) can be written as

$$\mathscr{L}^2 \frac{\mathrm{D}^2(\tilde{\cdot})}{\mathrm{D}t^2} = \frac{\partial}{\partial \xi^1}\left[(1-\xi^1)^2(\dot{\mathscr{L}})^2 \frac{\partial(\tilde{\cdot})}{\partial \xi^1}\right] + 2(1-\xi^1)\mathscr{L}\dot{\mathscr{L}} \frac{\partial^2(\tilde{\cdot})}{\partial \xi^1\, \partial t} + (1-\xi^1)\mathscr{L}\ddot{\mathscr{L}} \frac{\partial(\tilde{\cdot})}{\partial \xi^1} + \mathscr{L}^2 \frac{\partial^2(\tilde{\cdot})}{\partial t^2}\,, \tag{4.1}$$

where $(\tilde{\cdot})(\phi^1(X^1, t), t)$ can be either $\tilde{\boldsymbol{u}}_0$ or $\tilde{\vartheta}$. By the clamped boundary conditions (2.65) and the order of the PDEs in (2.63)–(2.64), we consider the space of admissible variations, satisfying the homogeneous essential boundary condition,[20] defined as (see e.g. [45])

$$\mathscr{V} := \{w \in H^1(]0, 1[) \mid w(0) = 0\}\,, \tag{4.2}$$

for the operator (4.1) whose weighted residual form is

$$\int_{]0,1[} w \mathscr{L}^2 \frac{\mathrm{D}^2(\tilde{\cdot})}{\mathrm{D}t^2}\, \mathrm{d}\xi^1\,. \tag{4.3}$$

The weak form of operator (4.1) results from the integration by parts of the first three terms; the result for each term is as follows. For the first term

$$\begin{aligned}
&\int_{]0,1[} w \frac{\partial}{\partial \xi^1}\left[(1-\xi^1)^2(\dot{\mathscr{L}})^2 \frac{\partial(\tilde{\cdot})}{\partial \xi^1}\right] \mathrm{d}\xi^1 \\
&\quad = \underbrace{w(1-\xi^1)^2(\dot{\mathscr{L}})^2 \frac{\partial(\tilde{\cdot})}{\partial \xi^1}\bigg|_{\xi^1=0}^{\xi^1=1}}_{=0} - (\dot{\mathscr{L}})^2 \int_{]0,1[} \frac{\partial w}{\partial \xi^1}(1-\xi^1)^2 \frac{\partial(\tilde{\cdot})}{\partial \xi^1}\, \mathrm{d}\xi^1\,.
\end{aligned} \tag{4.4}$$

Similar to the vanishing of the (underbraced) boundary terms in (4.4) above, the boundary terms in the weak forms of the other terms in the operator (4.1) also vanish (see Remark 4.1). The second term in (4.1) can be decomposed into two equal terms, with integration by parts on its weighted residual form performed only on one of the two terms to obtain

$$2\int_{]0,1[} w(1-\xi^1)\mathscr{L}\dot{\mathscr{L}} \frac{\partial^2(\tilde{\cdot})}{\partial \xi^1\, \partial t}\, \mathrm{d}\xi^1 = \mathscr{L}\dot{\mathscr{L}} \int_{]0,1[} (1-\xi^1)\left[w \frac{\partial^2(\tilde{\cdot})}{\partial \xi^1\, \partial t} - \frac{\partial w}{\partial \xi^1} \frac{\partial(\tilde{\cdot})}{\partial t}\right] \mathrm{d}\xi^1\,. \tag{4.5}$$

For the third term in (4.1), we have

$$\int_{]0,1[} w(1-\xi^1)\mathscr{L}\ddot{\mathscr{L}} \frac{\partial(\tilde{\cdot})}{\partial \xi^1}\, \mathrm{d}\xi^1 = \frac{1}{2}\mathscr{L}\ddot{\mathscr{L}} \int_{]0,1[} (1-\xi^1)\left[w \frac{\partial(\tilde{\cdot})}{\partial \xi^1} - \frac{\partial w}{\partial \xi^1}(\tilde{\cdot})\right] \mathrm{d}\xi^1\,. \tag{4.6}$$

Thus, gathering the results in (4.4)–(4.6) together, the weighted residual form (4.3) of the operator (4.1) has the following weak form

---

[20] Homogeneous essential boundary conditions are also imposed on the variations even when there are the type of prescribed large overall motions for the channel as noted in Remark 3.2, i.e. the choice of $\mathscr{V}$ as in (4.2) is valid for both (2.65) and (3.28).

$$\boxed{\begin{aligned}\int_{]0,1[} w\mathscr{L}^2 \frac{\mathrm{D}^2(\tilde{\cdot})}{\mathrm{D}t^2}\,\mathrm{d}\xi^1 = {} & \underbrace{\mathscr{L}^2 \int_{]0,1[} w \frac{\partial^2(\tilde{\cdot})}{\partial t^2}\,\mathrm{d}\xi^1}_{\text{Mass}} + \underbrace{\mathscr{L}\dot{\mathscr{L}} \int_{]0,1[} (1-\xi^1)\left[w \frac{\partial^2(\tilde{\cdot})}{\partial \xi^1\,\partial t} - \frac{\partial w}{\partial \xi^1}\frac{\partial(\tilde{\cdot})}{\partial t}\right]\mathrm{d}\xi^1}_{\text{Velocity-convection: Anti-symmetric}} \\ & \underbrace{\underbrace{- (\dot{\mathscr{L}})^2 \int_{]0,1[} \frac{\partial w}{\partial \xi^1}(1-\xi^1)^2 \frac{\partial(\tilde{\cdot})}{\partial \xi^1}\,\mathrm{d}\xi^1}_{\text{Symmetric}} + \underbrace{\frac{1}{2}\mathscr{L}\ddot{\mathscr{L}} \int_{]0,1[} (1-\xi^1)\left[w \frac{\partial(\tilde{\cdot})}{\partial \xi^1} - \frac{\partial w}{\partial \xi^1}(\tilde{\cdot})\right]\mathrm{d}\xi^1}_{\text{Anti-symmetric}}}_{\text{Stiffness-convection}} ,\end{aligned}} \tag{4.7}$$

showing the clear structure of the mass, velocity-convection, and stiffness-convection operators.

Remark 4.1. The validity of the weak form (4.7) for both $\tilde{\boldsymbol{u}}_0$ and $\tilde{\vartheta}$ is somewhat fortuitous due to the following reason. The boundary terms in (4.4)–(4.6) vanish because of the vanishing of the factor $(1-\xi^1)$ at $\xi^1 = 1$, and because of the homogeneous essential boundary condition $w(0) = 0$ at $\xi^1 = 0$, as reflected in the definition of $\mathscr{V}$ in (4.2). It should be noted that the free end condition (2.66) does *not* lead to

$$\left.\frac{\partial(\tilde{\cdot})}{\partial \xi^1}\right|_{\xi^1=1} = 0 \tag{4.8}$$

in general. In fact, condition $\tilde{\boldsymbol{f}}(1,t) = \boldsymbol{0}$ leads to $\tilde{\boldsymbol{\gamma}}(1,t) = \boldsymbol{0}$ by (2.71), and thus

$$\frac{\partial \tilde{\boldsymbol{u}}_0(1,t)}{\partial \xi^1} = \mathscr{L}(t)[\tilde{\boldsymbol{t}}_1(1,t) - \boldsymbol{E}_1] \neq \boldsymbol{0} \tag{4.9}$$

by (2.68). On the other hand, we do have

$$\frac{\partial \tilde{\vartheta}(1,t)}{\partial \xi^1} = 0 , \tag{4.10}$$

from the condition $\tilde{m}(1,t) = 0$, the constitutive law (2.76), and the curvature (2.69). For the same reasons as just discussed, one does not obtain the antisymmetric weak form of the operator

$$2\frac{\partial^2(\cdot)}{\partial \chi^1\,\partial t}\dot{\mathscr{L}} + \frac{\partial(\cdot)}{\partial \chi^1}\ddot{\mathscr{L}} \tag{4.11}$$

in the Eulerian–Lagrangian equations (3.21) for $\chi^1 \in]0, \mathscr{L}(t)[$ because of the non-vanishing of the boundary terms. □

Now consider the admissible variations $\boldsymbol{w} = w^\alpha \boldsymbol{e}_\alpha$, with $w^\alpha \in \mathscr{V}$, for $\tilde{\boldsymbol{u}}_0$ and $w^3 \in \mathscr{V}$ for $\tilde{\vartheta}$. Using the definition of the following pseudo displacement vectors and its corresponding variation

$$\tilde{\boldsymbol{U}} := \tilde{u}_0^\alpha \boldsymbol{e}_\alpha + \tilde{\vartheta}\boldsymbol{e}_3 , \qquad \boldsymbol{W} := \boldsymbol{w} + w^3 \boldsymbol{e}_3 \in \mathscr{V}^3 , \tag{4.12}$$

and the section inertia tensor

$$\boldsymbol{I}_\rho := I_\rho^{ij} \boldsymbol{e}_i \otimes \boldsymbol{e}_j , \qquad [I_\rho^{ij}] = \begin{bmatrix} A_\rho & & \\ & A_\rho & \\ & & I_\rho \end{bmatrix} \in \mathbb{R}^{3\times 3} , \tag{4.13}$$

we can write the weighted residual form of the full Lagrangian equations (2.63)–(2.64) in stretched coordinate as follows:

$$\boxed{G_{\mathrm{dyn}}(\boldsymbol{W}, \tilde{\boldsymbol{U}}) := G_{\mathrm{I}} \cdot (\boldsymbol{W}, \tilde{\boldsymbol{U}}) + G_{\mathrm{S}}(\boldsymbol{W}, \tilde{\boldsymbol{U}}) + G_{\mathrm{F}} \cdot \boldsymbol{W} = 0\,, \quad \forall \boldsymbol{W} \in \mathcal{V}^3\,,} \tag{4.14}$$

where

$$G_{\mathrm{I}} \cdot (\boldsymbol{W}, \tilde{\boldsymbol{U}}) := \int_{]0,1[} \boldsymbol{W} \cdot \boldsymbol{I}_\rho \cdot \mathscr{L}^2 \left\{ \frac{\mathrm{D}^2 \tilde{\boldsymbol{U}}}{\mathrm{D}t^2} + \ddot{\mathscr{L}} \boldsymbol{E}_1 \right\} \mathrm{d}\xi^1 \tag{4.15}$$

corresponds to the linear inertia operator,[21] and

$$G_{\mathrm{S}}(\boldsymbol{W}, \tilde{\boldsymbol{U}}) := -\mathscr{L} \int_{]0,1[} \left[\boldsymbol{w} \cdot \frac{\partial \tilde{\boldsymbol{f}}}{\partial \xi^1} + w^3 \left\{ \frac{\partial \tilde{m}}{\partial \xi^1} + \left(\frac{\partial \tilde{\boldsymbol{\Phi}}_0}{\partial \xi^1} \times \tilde{\boldsymbol{f}} \right) \cdot \boldsymbol{e}_3 \right\} \right] \mathrm{d}\xi^1 \tag{4.16}$$

corresponds to the non-linear stiffness operator, and

$$G_{\mathrm{F}} \cdot \boldsymbol{W} := -\mathscr{L}^2 \int_{]0,1[} \{ \boldsymbol{w} \cdot \tilde{\boldsymbol{f}}_\Gamma + w^3 \tilde{m}_\Gamma \} \, \mathrm{d}\xi^1 \tag{4.17}$$

the applied force/moment operator. Next, using the weak form (4.7), we obtain the following decomposition of the weak form of the inertia operator (4.15) for sliding beams

$$\boxed{G_{\mathrm{I}} \cdot (\boldsymbol{W}, \tilde{\boldsymbol{U}}) := \{ G_{\mathrm{I,M}} + G_{\mathrm{I,V}} + G_{\mathrm{I,S}} \} \cdot (\boldsymbol{W}, \tilde{\boldsymbol{U}}) + G_{\mathrm{I,F}} \cdot \boldsymbol{W}\,,} \tag{4.18}$$

where

$$G_{\mathrm{I,M}} \cdot (\boldsymbol{W}, \tilde{\boldsymbol{U}}) := \mathscr{L}^2 \int_{]0,1[} \boldsymbol{W} \cdot \boldsymbol{I}_\rho \cdot \frac{\partial^2 \tilde{\boldsymbol{U}}}{\partial t^2} \, \mathrm{d}\xi^1 \tag{4.19}$$

is the mass operator,

$$G_{\mathrm{I,V}} \cdot (\boldsymbol{W}, \tilde{\boldsymbol{U}}) := \mathscr{L} \dot{\mathscr{L}} \int_{]0,1[} (1 - \xi^1) \left[\boldsymbol{W} \cdot \boldsymbol{I}_\rho \cdot \frac{\partial^2 \tilde{\boldsymbol{U}}}{\partial \xi^1 \, \partial t} - \frac{\partial \boldsymbol{W}}{\partial \xi^1} \cdot \boldsymbol{I}_\rho \cdot \frac{\partial \tilde{\boldsymbol{U}}}{\partial t} \right] \mathrm{d}\xi^1 \tag{4.20}$$

the velocity-convection operator,

$$\begin{aligned} G_{\mathrm{I,S}} \cdot (\boldsymbol{W}, \tilde{\boldsymbol{U}}) := {} & -(\dot{\mathscr{L}})^2 \int_{]0,1[} (1 - \xi^1)^2 \frac{\partial \boldsymbol{W}}{\partial \xi^1} \cdot \boldsymbol{I}_\rho \cdot \frac{\partial \tilde{\boldsymbol{U}}}{\partial \xi^1} \, \mathrm{d}\xi^1 \\ & + \frac{1}{2} \mathscr{L} \ddot{\mathscr{L}} \int_{]0,1[} (1 - \xi^1) \left[\boldsymbol{W} \cdot \boldsymbol{I}_\rho \cdot \frac{\partial \tilde{\boldsymbol{U}}}{\partial \xi^1} - \frac{\partial \boldsymbol{W}}{\partial \xi^1} \cdot \boldsymbol{I}_\rho \cdot \tilde{\boldsymbol{U}} \right] \mathrm{d}\xi^1 \end{aligned} \tag{4.21}$$

the stiffness-convection operator, and

$$\begin{aligned} G_{\mathrm{I,F}} \cdot \boldsymbol{W} & := \mathscr{L}^2 \ddot{\mathscr{L}} \int_{]0,1[} \boldsymbol{W} \cdot A_\rho \boldsymbol{E}_1 \, \mathrm{d}\xi^1 \\ & = \mathscr{L}^2 \ddot{\mathscr{L}} \int_{]0,1[} A_\rho (w^1 \cos \vartheta_0 \, \boldsymbol{e}_1 + w^2 \sin \vartheta_0 \, \boldsymbol{e}_2) \, \mathrm{d}\xi^1 \end{aligned} \tag{4.22}$$

the inertia force due to sliding motion. All of these operators are explicitly time-dependent because they contain $\mathscr{L}(t)$ and/or its time derivatives. We now look at the weighted residual form (4.16) of the non-linear stiffness operator. The boundary terms resulting from the integration by parts of the first two terms in the stiffness operator (4.16) vanish by the homogeneous essential boundary condition on the variations, i.e. $\boldsymbol{W}(0) = 0$, and by the free-end condition (2.66). We therefore obtain the following weak form of the non-linear stiffness operator

---

[21] The dot '·' in $G_{\mathrm{I}} \cdot (\boldsymbol{W}, \tilde{\boldsymbol{U}})$ is used to indicate that the operator G_{I} is linear with respect to both arguments $(\boldsymbol{W}, \tilde{\boldsymbol{U}})$.

$$\boxed{\begin{aligned} G_S(\boldsymbol{W}, \tilde{\boldsymbol{u}}) &= \mathscr{L} \int_{]0,1[} \left\{ \frac{\partial \boldsymbol{w}}{\partial \xi^1} \cdot \tilde{\boldsymbol{f}} + \frac{\partial w^3}{\partial \xi^1} \tilde{m} - w^3 \left(\frac{\partial \tilde{\boldsymbol{\Phi}}_0}{\partial \xi^1} \times \tilde{\boldsymbol{f}} \right) \cdot \boldsymbol{e}_3 \right\} \mathrm{d}\xi^1 \\ &= \mathscr{L} \int_{]0,1[} [\mathscr{D}(\tilde{\boldsymbol{U}}) \cdot \boldsymbol{W}] \cdot \boldsymbol{p}(\tilde{\boldsymbol{U}})\, \mathrm{d}\xi^1 , \end{aligned}} \tag{4.23}$$

where the time-dependent differential operator $\mathscr{D}$ is defined as follows

$$\mathscr{D} = \mathscr{D}^{ij} \boldsymbol{e}_i \otimes \boldsymbol{e}_j , \qquad [\mathscr{D}^{ij}] = \begin{bmatrix} \dfrac{\partial}{\partial \xi^1} & 0 & \dfrac{\partial \tilde{\Phi}_0^2}{\partial \xi^1} \\ 0 & \dfrac{\partial}{\partial \xi^1} & -\dfrac{\partial \tilde{\Phi}_0^1}{\partial \xi^1} \\ 0 & 0 & \dfrac{\partial}{\partial \xi^1} \end{bmatrix} , \tag{4.24}$$

with

$$\frac{\partial \tilde{\boldsymbol{\Phi}}_0}{\partial \xi^1} = \frac{\partial \tilde{\Phi}_0^\alpha}{\partial \xi^1} \boldsymbol{e}_\alpha = \mathscr{L}(t) \boldsymbol{E}_1 + \frac{\partial \tilde{\boldsymbol{u}}_0}{\partial \xi^1} = \left\{ \mathscr{L} \cos \vartheta_0 + \frac{\partial \tilde{u}_0^1}{\partial \xi^1} \right\} \boldsymbol{e}_1 + \left\{ \mathscr{L} \sin \vartheta_0 + \frac{\partial \tilde{u}_0^2}{\partial \xi^1} \right\} \boldsymbol{e}_2 , \tag{4.25}$$

by virtue of (2.18) and (2.53), and where $\boldsymbol{p}(\tilde{\boldsymbol{U}})$ is a pseudo resultant force vector defined as

$$\boldsymbol{p} := \tilde{\boldsymbol{f}} + \tilde{m} \boldsymbol{e}_3 . \tag{4.26}$$

REMARK 4.2. Concentrated force/couple at beam tip. In the case where there are a concentrated force $\hat{\boldsymbol{f}}(t)$ and a concentrated couple $\hat{m}(t)$ at the beam tip, as described in (3.29)–(3.30) of Remark 3.2, we then have the following additional boundary terms in the weak form (4.23) denoted by $G_S(\boldsymbol{W}, \tilde{\boldsymbol{U}})$, as a result of the integration by parts,

$$-\mathscr{L}(t)\{\boldsymbol{w}(1) \cdot \hat{\boldsymbol{f}}(t) + w^3(1) \hat{m}(t)\} . \tag{4.27}$$

The above weighted residual form (4.27) for concentrated force/couple can also be obtained from the weighted residual form (4.17) for distributed force/couple as follows. By letting

$$\boldsymbol{f}_\Gamma(X^1, t) = \hat{\boldsymbol{f}}(t) \delta(X^1 - L) , \qquad m_\Gamma(X^1, t) = \hat{m}(t) \delta(X^1 - L) , \tag{4.28}$$

where δ is the Kronecker delta, and by noting that

$$\mathrm{d}\xi^1 = \frac{\mathrm{d}X^1}{\mathscr{L}} , \tag{4.29}$$

which follows from (2.52), we obtain from (4.17)

$$-\mathscr{L}^2 \int_{]0,1[} \{\boldsymbol{w} \cdot \tilde{\boldsymbol{f}}_\Gamma + w^3 \tilde{m}_\Gamma\}\, \mathrm{d}\xi^1 = -\mathscr{L}(t)\{\boldsymbol{w}(1) \cdot \hat{\boldsymbol{f}}(t) + w^3(1) \hat{m}(t)\} . \tag{4.30}$$

Thus, while the distributed force/couple is multiplied by the factor $\mathscr{L}^2(t)$, the concentration force/couple is only multiplied by the factor $\mathscr{L}(t)$. An example of sliding beam with an applied concentrated force at the beam tip will be given in Section 5. □

4.2. Linearization of weak form

The non-linear equation (4.14) can be solved using Newton's method, which requires a linearization of (4.14). Consider a fixed state $\tilde{\boldsymbol{U}} = {}^*\tilde{\boldsymbol{U}}$ and a variation (direction) $\boldsymbol{q} \in \mathscr{V}^3$. Then the linearization of the dynamic weak form G_{dyn} at ${}^*\tilde{\boldsymbol{U}}$ is

$$L[G_{\mathrm{dyn}}(\boldsymbol{W}, {}^*\tilde{\boldsymbol{U}})] := G_{\mathrm{dyn}}(\boldsymbol{W}, {}^*\tilde{\boldsymbol{U}}) + DG_{\mathrm{dyn}}({}^*\tilde{\boldsymbol{U}}) \cdot (\boldsymbol{W}, \boldsymbol{q}) , \tag{4.31}$$

where $DG_{\text{dyn}}({}^*\tilde{\boldsymbol{U}})\cdot(\boldsymbol{W},\boldsymbol{q})$ is the tangent dynamic operator, and is the directional derivative of G_{dyn} at ${}^*\tilde{\boldsymbol{U}}$, in the direction $\boldsymbol{q}$ (e.g. [46]). The direction $\boldsymbol{q}$ can be thought of as an incremental pseudo displacement—in the sense of (4.12)—at ${}^*\tilde{\boldsymbol{U}}$. We have

$$DG_{\text{dyn}}({}^*\tilde{\boldsymbol{U}})\cdot(\boldsymbol{W},\boldsymbol{q}) = G_{\text{I}}\cdot(\boldsymbol{W},\boldsymbol{q}) + DG_{\text{S}}({}^*\tilde{\boldsymbol{U}})\cdot(\boldsymbol{W},\boldsymbol{q})\,, \tag{4.32}$$

where $DG_{\text{S}}({}^*\tilde{\boldsymbol{U}})$, the tangent stiffness operator at ${}^*\tilde{\boldsymbol{U}}$, is obtained from (4.23) as

$$\begin{aligned} &DG_{\text{S}}({}^*\tilde{\boldsymbol{U}})\cdot(\boldsymbol{W},\boldsymbol{q}) \\ &\quad = \int_{]0,1[} [D\mathscr{D}({}^*\tilde{\boldsymbol{U}})\cdot(\boldsymbol{W},\boldsymbol{q})]\cdot \boldsymbol{p}({}^*\tilde{\boldsymbol{U}})\,\mathrm{d}\xi^1 + \int_{]0,1[} [\mathscr{D}({}^*\tilde{\boldsymbol{U}})\cdot\boldsymbol{W}]\cdot D\boldsymbol{p}({}^*\tilde{\boldsymbol{U}})\cdot(\boldsymbol{W},\boldsymbol{q})\,\mathrm{d}\xi^1\,. \end{aligned} \tag{4.33}$$

The tangent stiffness operator DG_{S} can be decomposed into two parts: The tangent geometric stiffness operator $D^{\text{g}}G_{\text{S}}$ and the tangent material stiffness operator $D^{\text{m}}G_{\text{S}}$

$$DG_{\text{S}}({}^*\tilde{\boldsymbol{U}})\cdot(\boldsymbol{W},\boldsymbol{q}) = [D^{\text{g}} + D^{\text{m}}]G_{\text{S}}({}^*\tilde{\boldsymbol{U}})\cdot(\boldsymbol{W},\boldsymbol{q})\,. \tag{4.34}$$

It should be noted that the tangent geometric stiffness operator includes not only the first term in (4.33), but also part of the second term in (4.33). In a similar manner as in [35], we obtain the expression for the tangent geometric stiffness operator $D^{\text{g}}G_{\text{S}}$ as follows

$$\boxed{D^{\text{g}}G_{\text{S}}({}^*\tilde{\boldsymbol{U}})\cdot(\boldsymbol{W},\boldsymbol{q}) = \mathscr{L}\int_{]0,1[} [\boldsymbol{\Upsilon}\cdot\boldsymbol{W}]\cdot[\boldsymbol{B}({}^*\tilde{\boldsymbol{U}})\cdot\boldsymbol{\Upsilon}\cdot\boldsymbol{q}]\,\mathrm{d}\xi^1\,,} \tag{4.35}$$

where the operators $\boldsymbol{\Upsilon} = \Upsilon^{ij}\boldsymbol{e}_i\otimes\boldsymbol{e}_j$ and $\boldsymbol{B} = B^{ij}\boldsymbol{e}_i\otimes\boldsymbol{e}_j$ have the following matrices of components

$$[\Upsilon^{ij}] = \begin{bmatrix} \dfrac{\mathrm{d}}{\partial\xi^1} & & \\ & \dfrac{\mathrm{d}}{\partial\xi^1} & \\ & & 1 \end{bmatrix}, \quad [B^{ij}({}^*\tilde{\boldsymbol{U}})] = \begin{bmatrix} 0 & 0 & -{}^*\tilde{f}^2 \\ 0 & 0 & {}^*\tilde{f}^1 \\ -{}^*\tilde{f}^2 & {}^*\tilde{f}^1 & -\left(\dfrac{\partial{}^*\tilde{\Phi}_0^1}{\partial\xi^1}\,{}^*\tilde{f}^1 + \dfrac{\partial{}^*\tilde{\Phi}_0^2}{\partial\xi^1}\,{}^*\tilde{f}^2\right) \end{bmatrix}, \tag{4.36}$$

where ${}^*\widetilde{(\cdot)}$ designates that the quantity $\widetilde{(\cdot)}$ is to be evaluated at the state $\tilde{\boldsymbol{U}} = {}^*\tilde{\boldsymbol{U}}$.

REMARK 4.3. Note the difference between the tangent geometric stiffness (4.35), expression (4.36) for $[B^{ij}]$ and their counterparts in [35]. The operator in (4.35) is explicitly time dependent by the presence of the factor $\mathscr{L}(t)$, and $\vartheta_0 \neq 0$ in general here (see (4.25)), whereas $\vartheta_0 = 0$ in [35]. □

The tangent material stiffness operator $D^{\text{m}}G_{\text{S}}$ is given by

$$\boxed{D^{\text{m}}G_{\text{S}}({}^*\tilde{\boldsymbol{U}})\cdot(\boldsymbol{W},\boldsymbol{q}) = \mathscr{L}\int_{]0,1[} [\mathscr{D}({}^*\tilde{\boldsymbol{U}})\cdot\boldsymbol{W}]\cdot[\boldsymbol{\Lambda}({}^*\tilde{\vartheta})\cdot\boldsymbol{C}\cdot\boldsymbol{\Lambda}^{\text{T}}({}^*\tilde{\vartheta})\cdot\mathscr{D}({}^*\tilde{\boldsymbol{U}})\cdot\boldsymbol{q}]\,\mathrm{d}\xi^1\,.} \tag{4.37}$$

Thus, the linearized weak form (4.31) at ${}^*\tilde{\boldsymbol{U}}$, to be solved in a Newton iteration,

$$\forall \boldsymbol{W}\in\mathscr{V}^3\,,\qquad L[G_{\text{dyn}}(\boldsymbol{W},{}^*\tilde{\boldsymbol{U}})] = 0 \tag{4.38}$$

can now be written as

$$\boxed{\begin{aligned} &\forall \boldsymbol{W}\in\mathscr{V}^3\,, \\ &[G_{\text{I,M}} + G_{\text{I,V}} + \underbrace{G_{\text{I,S}} + D^{\text{g}}G_{\text{S}}({}^*\tilde{\boldsymbol{U}}) + D^{\text{m}}G_{\text{S}}({}^*\tilde{\boldsymbol{U}})}_{\text{Total tangent stiffness}}]\cdot(\boldsymbol{W},\boldsymbol{q}) = -G_{\text{dyn}}(\boldsymbol{W},{}^*\tilde{\boldsymbol{U}})\,. \end{aligned}} \tag{4.39}$$

REMARK 4.4. The total tangent stiffness operator in (4.39) evaluated at $^*\tilde{U}$ contains three components: the *convection stiffness* $G_{\mathrm{I,S}}$ (which in turn contains a symmetric part and an anti-symmetric part), the *tangent geometric stiffness* $D^{\mathrm{g}}G_{\mathrm{S}}(^*\tilde{U})$ (symmetric) and the *tangent material stiffness* $D^{\mathrm{m}}G_{\mathrm{S}}(^*\tilde{U})$ (symmetric). □

REMARK 4.5. Eq. (4.39) has a similar structure to the equation of motion for the dual problem of dynamic vehicle/structure interaction formulated in [4, 5]. □

4.3. *Semi-discrete equations*

Consider the following approximation

$$\begin{aligned} \boldsymbol{W}(\xi^1) &\approx \boldsymbol{W}^h(\xi^1) := \sum_{A=1}^{n} N_A(\xi^1)\boldsymbol{c}_A \qquad \in (\mathcal{V}^h)^3 \subset \mathcal{V}^3 , \\ \tilde{\boldsymbol{U}}(\xi^1, t) &\approx \tilde{\boldsymbol{U}}^h(\xi^1, t) := \sum_{B=1}^{n} N_B(\xi^1)\boldsymbol{d}_B(t) \in (\mathcal{V}^h)^3 \subset \mathcal{V}^3 , \end{aligned} \tag{4.40}$$

where $N_A, \boldsymbol{c}_A = c_A^i \boldsymbol{e}_i \in \mathbb{R}^3$, and $\boldsymbol{d}_A(t) = d_A^i(t)\boldsymbol{e}_i \in \mathbb{R}^3$, for $A = 1, \ldots, n$, are a set of basis functions with their associated pseudo vectors, and $\mathcal{V}^h$ a finite-dimensional subspace of $\mathcal{V}$ spanned by these chosen basis functions. In particular, for a Galerkin nodal finite element method, the following discretization of the interval $[0, 1]$ can be considered

$$\xi_0^1 \equiv 0 < \xi_1^1 < \cdots < \xi_A^1 < \cdots < \xi_n^1 \equiv 1 , \quad \text{with } A = 1, \ldots, n . \tag{4.41}$$

Define the global column matrices[22]

$$\boldsymbol{c} := \{\boldsymbol{c}_A\} \equiv \{\boldsymbol{c}_1, \ldots, \boldsymbol{c}_n\}^{\mathrm{T}} \in \mathbb{R}^{3n\times 1} , \qquad \boldsymbol{d} := \{\boldsymbol{d}_A\} \equiv \{\boldsymbol{d}_1, \ldots, \boldsymbol{d}_n\}^{\mathrm{T}} \in \mathbb{R}^{3n\times 1} , \tag{4.42}$$

and the unit tensor

$$\mathbf{1} := \delta^{ij}\boldsymbol{e}_i \otimes \boldsymbol{e}_j , \tag{4.43}$$

with δ^{ij} being a Kronecker delta. We proceed to obtain the discrete operators for the weak form $G_{\mathrm{dyn}}(\boldsymbol{W}, \tilde{\boldsymbol{U}})$ in (4.14). For the mass operator (4.19), we have

$$\boxed{\begin{aligned} &G_{\mathrm{I,M}} \cdot (\boldsymbol{W}^h, \tilde{\boldsymbol{U}}^h) = \boldsymbol{c}^{\mathrm{T}}\boldsymbol{M}(t)\ddot{\boldsymbol{d}}(t) , \qquad \boldsymbol{M}(t) = \mathscr{L}^2[\boldsymbol{M}_{AB}] \in \mathbb{R}^{3n\times 3n} , \\ &\boldsymbol{M}_{AB} = \int_{]0,1[} [N_A\mathbf{1}] \cdot \boldsymbol{I}_\rho \cdot [N_B\mathbf{1}] \,\mathrm{d}\xi^1 \in \mathbb{R}^{3\times 3} , \end{aligned}} \tag{4.44}$$

where $\boldsymbol{M}(t)$ is the time-dependent mass matrix. For the velocity-convection operator (4.20),

$$\boxed{\begin{aligned} &G_{\mathrm{I,V}} \cdot (\boldsymbol{W}^h, \tilde{\boldsymbol{U}}^h) = \boldsymbol{c}^{\mathrm{T}}\boldsymbol{V}(t)\dot{\boldsymbol{d}}(t) , \qquad \boldsymbol{V}(t) = \mathscr{L}\dot{\mathscr{L}}[\boldsymbol{V}_{AB}] \in \mathbb{R}^{3n\times 3n} , \\ &\boldsymbol{V}_{AB} = \int_{]0,1[} (1 - \xi^1)\{[N_A\mathbf{1}] \cdot \boldsymbol{I}_\rho \cdot [N_{B,\xi}\mathbf{1}] - [N_{A,\xi}\mathbf{1}] \cdot \boldsymbol{I}_\rho \cdot [N_B\mathbf{1}]\} \,\mathrm{d}\xi^1 \in \mathbb{R}^{3\times 3} , \end{aligned}} \tag{4.45}$$

where

$$N_{A,\xi} := \frac{\mathrm{d}N_A(\xi^1)}{\mathrm{d}\xi^1} , \tag{4.46}$$

---

[22] From here on, we often identify a tensor quantity to its matrix of components to simplify the exposition.

and $V(t)$ is the time-dependent velocity-convection matrix. For the stiffness-convection operator (4.21)

$$\boxed{\begin{aligned}
&G_{\mathrm{I,S}}\cdot(\boldsymbol{W}^h, \tilde{\boldsymbol{U}}^h) = \boldsymbol{c}^{\mathrm{T}}\boldsymbol{S}^c(t)\boldsymbol{d}(t)\,, \qquad \boldsymbol{S}^c = \boldsymbol{S}^{c1} + \boldsymbol{S}^{c2} \in \mathbb{R}^{3n\times 3n}\,,\\
&\boldsymbol{S}^{c\alpha} = [\boldsymbol{S}^{c\alpha}_{AB}] \in \mathbb{R}^{3n\times 3n}\,, \quad \alpha = 1, 2\,,\\
&\boldsymbol{S}^{c1}_{AB}(t) = -(\dot{\mathscr{L}})^2 \int_{]0,1[} (1-\xi^1)^2\{[N_{A,\xi}\mathbf{1}]\cdot\boldsymbol{I}_\rho\cdot[N_{B,\xi}\mathbf{1}]\}\,\mathrm{d}\xi^1 \in \mathbb{R}^{3\times 3}\,,\\
&\boldsymbol{S}^{c2}_{AB}(t) = \frac{1}{2}\mathscr{L}\ddot{\mathscr{L}}\boldsymbol{V}_{AB} \in \mathbb{R}^{3\times 3}\,,
\end{aligned}} \tag{4.47}$$

where the stiffness matrices S^{c1} and S^{c2} correspond to the symmetric part and the anti-symmetric part of the stiffness-convection operator, respectively. For the inertia force due to sliding motion (4.22),

$$\boxed{\begin{aligned}
&G_{\mathrm{I,F}}\cdot\boldsymbol{W}^h = \boldsymbol{c}^{\mathrm{T}}\boldsymbol{F}^{\mathrm{slid}}(t)\,, \qquad \boldsymbol{F}^{\mathrm{slid}}(t) = \{\boldsymbol{F}^{\mathrm{slid}}_A(t)\} \in \mathbb{R}^{3n\times 1}\,,\\
&\boldsymbol{F}^{\mathrm{slid}}_A(t) = \mathscr{L}^2\ddot{\mathscr{L}} \int_{]0,1[} A_\rho[N_A\mathbf{1}]\cdot\boldsymbol{E}_1\,\mathrm{d}\xi^1 \in \mathbb{R}^{3\times 1}\,,
\end{aligned}} \tag{4.48}$$

where $F^{\mathrm{slid}}(t)$ is the time-dependent inertia force column matrix due to sliding motion. For the nonlinear stiffness operator (4.23)

$$\boxed{\begin{aligned}
&G_{\mathrm{I,S}}\cdot(\boldsymbol{W}^h, \tilde{\boldsymbol{U}}^h) = \boldsymbol{c}^{\mathrm{T}}\mathscr{F}(\boldsymbol{d}, t)\,, \qquad \mathscr{F} = \{\mathscr{F}_A\} \in \mathbb{R}^{3n\times 1}\,,\\
&\mathscr{D}^h(\boldsymbol{d}) := \mathscr{D}(\tilde{\boldsymbol{U}}^h) \equiv \mathscr{D}\Big(\sum_B N_B\boldsymbol{d}_B\Big)\,,\\
&\boldsymbol{p}^h(\boldsymbol{d}) := \boldsymbol{p}(\tilde{\boldsymbol{U}}^h) \equiv \boldsymbol{p}\Big(\sum_B N_B\boldsymbol{d}_B\Big)\,,\\
&\mathscr{F}_A(\boldsymbol{d}, t) = \mathscr{L} \int_{]0,1[} \{\mathscr{D}^h(\boldsymbol{d})\cdot[N_A\mathbf{1}]\}^{\mathrm{T}}\cdot\boldsymbol{p}^h(\boldsymbol{d})\,\mathrm{d}\xi^1 \in \mathbb{R}^{3\times 1}\,,
\end{aligned}} \tag{4.49}$$

where $\mathscr{F}(d, t)$ is the column matrix of nonlinear internal force/moment. For the applied force/moment operator (4.17),

$$\boxed{\begin{aligned}
&G_{\mathrm{F}}\cdot\boldsymbol{W}^h = -\boldsymbol{c}^{\mathrm{T}}\boldsymbol{F}^{\mathrm{appl}}(t)\,, \qquad \boldsymbol{F}^{\mathrm{appl}} = \{\boldsymbol{F}^{\mathrm{appl}}_A\} \in \mathbb{R}^{3n\times 1}\,,\\
&\boldsymbol{p}_\Gamma := \tilde{\boldsymbol{f}}_\Gamma + \tilde{m}_\Gamma\boldsymbol{e}_3\,,\\
&\boldsymbol{F}^{\mathrm{appl}}_A(t) = \mathscr{L}^2 \int_{]0,1[} [N_A\mathbf{1}]\cdot\boldsymbol{p}_\Gamma\,\mathrm{d}\xi^1 \in \mathbb{R}^{3\times 1}\,,
\end{aligned}} \tag{4.50}$$

where $F^{\mathrm{appl}}(t)$ is the column matrix of applied force/moment. The above discrete approximation of the weak form G_{dyn} in (4.14) leads to the following semi-discrete equation

$$\boxed{\boldsymbol{M}(t)\ddot{\boldsymbol{d}} + \boldsymbol{V}(t)\dot{\boldsymbol{d}} + \boldsymbol{S}^c(t)\boldsymbol{d} + \mathscr{F}(\boldsymbol{d}, t) = \underbrace{-\boldsymbol{F}^{\mathrm{slid}}(t) + \boldsymbol{F}^{\mathrm{appl}}(t)}_{\boldsymbol{F}(t)}\,,} \tag{4.51}$$

a set of non-linear ODEs, which together with appropriate initial conditions for $d(0)$ and $\dot{d}(0)$ govern the dynamic behavior of geometrically-exact sliding beams.

4.4. Time discretization: conceptual algorithm and algebraic equation

Our emphasis here is not on any particular time discretization algorithm. The reader is referred to, e.g. Smolinski et al. [47] and the references therein for various time-stepping algorithms. Our goal is to present a conceptual procedure that would cover a large class of time-stepping algorithms for solving the structural dynamics equation (4.51). The approximations for the acceleration, velocity and displacement at time t_k are denoted by

$$\boldsymbol{a}_k \approx \boldsymbol{a}(t_k) := \ddot{\boldsymbol{d}}(t_k)\,, \qquad \boldsymbol{v}_k \approx \boldsymbol{v}(t_k) := \dot{\boldsymbol{d}}(t_k)\,, \qquad \boldsymbol{d}_k \approx \boldsymbol{d}(t_k)\,. \tag{4.52}$$

Assume that the solutions $\{\boldsymbol{a}_i, \boldsymbol{v}_i, \boldsymbol{d}_i \,|\, \text{for } i = 1, \ldots, k\}$, had been known; we are looking for the solution at time t_{k+1}. Equilibrium of the system at time t_{k+1} dictates that $\{\boldsymbol{a}_{k+1}, \boldsymbol{v}_{k+1}, \boldsymbol{d}_{k+1}\}$ must satisfy (4.51), i.e.

$$\boldsymbol{M}_{k+1}\boldsymbol{a}_{k+1} + \boldsymbol{V}_{k+1}\boldsymbol{v}_{k+1} + \boldsymbol{S}^c_{k+1}\boldsymbol{d}_{k+1} + \mathscr{F}_{k+1}(\boldsymbol{d}_{k+1}) = \boldsymbol{F}_{k+1}\,, \tag{4.53}$$

where it is clear that $\boldsymbol{M}_{k+1} := \boldsymbol{M}(t_{k+1})$, $\boldsymbol{V}_{k+1} := \boldsymbol{V}(t_{k+1})$, etc. Thus, we consider here a conceptual time-stepping algorithm defined as follows

$$\boxed{\boldsymbol{a}_{k+1} = \mathfrak{A}(\boldsymbol{d}_{k+1})\,, \qquad \boldsymbol{v}_{k+1} = \mathfrak{B}(\boldsymbol{d}_{k+1})\,,} \tag{4.54}$$

where $\mathfrak{A}$ and $\mathfrak{B}$ are functions of $\{\boldsymbol{a}_i, \boldsymbol{v}_i, \boldsymbol{d}_i \,|\, \text{for } i = k+1, k, k-1, \ldots\}$, i.e. the unknown solution at t_{k+1} and the known solutions at previous time steps.

REMARK 4.6. For example, for the Newmark algorithm, the conceptual algorithm (4.54) takes the form

$$\boldsymbol{a}_{k+1} = \mathfrak{A}(\boldsymbol{d}_{k+1}) := \frac{\boldsymbol{d}_{k+1} - \boldsymbol{d}_k}{h^2\beta} - \frac{\boldsymbol{v}_k}{h\beta} - \frac{\frac{1}{2} - \beta}{\beta}\boldsymbol{a}_k\,, \tag{4.55}$$

$$\boldsymbol{v}_{k+1} = \mathfrak{B}(\boldsymbol{d}_{k+1}) := \boldsymbol{v}_k + h[(1-\gamma)\boldsymbol{a}_k + \gamma\mathfrak{A}(\boldsymbol{d}_{k+1})]\,, \tag{4.56}$$

where h is the current time step size, $\beta \in [0, \frac{1}{2}]$, and $\gamma \in [0, 1]$. The Newmark algorithm involves only the unknown solution at t_{k+1} and only the known solution at t_k, i.e. a single-step algorithm. The algorithm proposed by Hoff and Pahl [48] is yet another algorithm belonging to the category described by the conceptual algorithm (4.54).

More generally, equilibrium can be considered at a time $\tau \in]t_k, t_{k+1}[$, instead of at t_{k+1} as in (4.53),

$$\boldsymbol{M}(\tau)\boldsymbol{a}(\tau) + \boldsymbol{V}(\tau)\boldsymbol{v}(\tau) + \boldsymbol{S}^c(\tau)\boldsymbol{d}(\tau) + \mathscr{F}(\boldsymbol{d}(\tau), \tau) = \boldsymbol{F}(\tau)\,. \tag{4.57}$$

Now, if $\boldsymbol{M}, \boldsymbol{V}, \boldsymbol{S}$, and $\mathscr{F}$ do not depend explicitly on time t, then approximations for $\{\boldsymbol{a}(\tau), \boldsymbol{v}(\tau), \boldsymbol{d}(\tau)\}$ in terms of $\{\boldsymbol{a}_i, \boldsymbol{v}_i, \boldsymbol{d}_i \,|\, \text{for } i = k+1, k, k-1, \ldots\}$ are introduced conceptually as follows

$$\boldsymbol{a}(\tau) = \mathfrak{A}(\boldsymbol{d}_{k+1})\,, \qquad \boldsymbol{v}(\tau) = \mathfrak{B}(\boldsymbol{v}_{k+1})\,, \qquad \boldsymbol{d}(\tau) = \mathfrak{D}(\boldsymbol{d}_{k+1})\,. \tag{4.58}$$

Examples of this class of algorithms are the one proposed by Hilber et al. [49] and more recently the one by Hulbert and Chung [50]. The main goal of these last two algorithms and the Hoff and Pahl [48] algorithm mentioned above is to damp out the high-frequency oscillations in the numerical results.

In the case of the Hulbert and Chung [50] algorithm, $\boldsymbol{a}(\tau)$ is a linear combination of $\boldsymbol{a}_{k+1}$ and $\boldsymbol{a}_k$; similarly for $\boldsymbol{v}(\tau)$ and for $\boldsymbol{d}(\tau)$. Then the Newmark algorithm (4.55)–(4.56) is used to relate $\boldsymbol{a}_{k+1}$ and $\boldsymbol{v}_{k+1}$ to $\boldsymbol{d}_{k+1}$, i.e. to obtain explicit expressions for $\mathfrak{A}$ and for $\mathfrak{B}$ in $(4.58)_1$ and in $(4.58)_2$, respectively. The operator $\mathfrak{D}$ in $(4.58)_3$, as just mentioned, is a linear combination of $\boldsymbol{d}_{k+1}$ and $\boldsymbol{d}_k$.

Note however, that if $\boldsymbol{M}, \boldsymbol{V}, \boldsymbol{S}$, and $\mathscr{F}$ depend explicitly on time t, then these algorithms are not convenient because one has to interpolate in time the mentioned matrices, in addition to the fact that the analyses of these algorithms were performed and tested only for the case of time-invariant coefficients. We will use the conceptual algorithm (4.54) for our numerical examples in Section 5, and thus will restrict our attention in what follows to the conceptual algorithm (4.54). ☐

Using (4.54), the equilibrium equation (4.53) becomes a nonlinear matrix algebraic equation in terms of the primary unknown $\boldsymbol{d}_{k+1}$:

$$\boxed{\boldsymbol{R}_{k+1}(\boldsymbol{d}_{k+1}) := \boldsymbol{M}_{k+1}\mathfrak{A}(\boldsymbol{d}_{k+1}) + \boldsymbol{V}_{k+1}\mathfrak{B}(\boldsymbol{d}_{k+1}) + \boldsymbol{S}^{c}_{k+1}\boldsymbol{d}_{k+1} + \boldsymbol{\mathcal{F}}_{k+1}(\boldsymbol{d}_{k+1}) - \boldsymbol{F}_{k+1} = 0\,.} \tag{4.59}$$

Newton's method for solving (4.59) then takes the form

$$\boxed{\begin{aligned} &\boldsymbol{d}^{(i+1)}_{k+1} = \boldsymbol{d}^{(i)}_{k+1} + \Delta\boldsymbol{d}^{(i+1)}_{k+1}\,, \\ &\boldsymbol{R}_{k+1}(\boldsymbol{d}^{(i)}_{k+1}) + D\boldsymbol{R}_{k+1}(\boldsymbol{d}^{(i)}_{k+1})\cdot\Delta\boldsymbol{d}^{(i+1)}_{k+1} = 0\,, \end{aligned}} \tag{4.60}$$

where the derivative of the residue $\boldsymbol{R}_{k+1}$ at $\boldsymbol{d}^{(i)}_{k+1}$—i.e. $D\boldsymbol{R}_{k+1}(\boldsymbol{d}^{(i)}_{k+1}) \in \mathbb{R}^{3n\times 3n}$ in the last term of $(4.60)_2$—is the dynamic tangent stiffness matrix. We have

$$\boxed{\begin{aligned} &D\boldsymbol{R}_{k+1}(\boldsymbol{d}^{(i)}_{k+1}) = \boldsymbol{M}_{k+1}D\mathfrak{A}(\boldsymbol{d}^{(i)}_{k+1}) + \boldsymbol{V}_{k+1}D\mathfrak{B}(\boldsymbol{d}^{(i)}_{k+1}) + \boldsymbol{S}^{c}_{k+1} + D\boldsymbol{\mathcal{F}}_{k+1}(\boldsymbol{d}^{(i)}_{k+1})\,, \\ &D\boldsymbol{\mathcal{F}}_{k+1}(\boldsymbol{d}^{(i)}_{k+1}) = [D^{\mathrm{g}} + D^{\mathrm{m}}]\boldsymbol{\mathcal{F}}_{k+1}(\boldsymbol{d}^{(i)}_{k+1})\,, \end{aligned}} \tag{4.61}$$

where $D\boldsymbol{\mathcal{F}}_{k+1}(\boldsymbol{d}^{(i)}_{k+1}) \in \mathbb{R}^{3n\times 3n}$ is the tangent stiffness matrix at time t_{k+1}, evaluated at the current iterate $\boldsymbol{d}^{(i)}_{k+1}$, and contains the tangent geometric stiffness matrix $D^{\mathrm{g}}\boldsymbol{\mathcal{F}}_{k+1}(\boldsymbol{d}^{(i)}_{k+1})$, and the tangent material stiffness matrix $D^{\mathrm{m}}\boldsymbol{\mathcal{F}}_{k+1}(\boldsymbol{d}^{(i)}_{k+1})$, as per (4.34).

REMARK 4.7. For the Newmark algorithm (4.55)–(4.56), we have

$$D\mathfrak{A}(\boldsymbol{d}^{(i)}_{k+1}) = \frac{1}{h^2\beta}\,, \qquad D\mathfrak{B}(\boldsymbol{d}^{(i)}_{k+1}) = \frac{\gamma}{h\beta}\,. \tag{4.62}$$

The update of the acceleration and velocity is carried out as follows

$$\boldsymbol{a}^{(i+1)}_{k+1} = \boldsymbol{a}^{(i)}_{k+1} + \frac{1}{h^2\beta}\Delta\boldsymbol{d}^{(i+1)}_{k+1}\,, \tag{4.63}$$

$$\boldsymbol{v}^{(i+1)}_{k+1} = \boldsymbol{v}^{(i)}_{k+1} + \frac{\gamma}{h\beta}\Delta\boldsymbol{d}^{(i+1)}_{k+1}\,. \tag{4.64}$$

Also, the initial guess at the beginning of each time step is chosen to be

$$\boldsymbol{d}^{(0)}_{k+1} = \boldsymbol{d}_k\,, \tag{4.65}$$

$$\boldsymbol{a}^{(0)}_{k+1} = -\left[\frac{\boldsymbol{v}_k}{h\beta} + \frac{\frac{1}{2}-\beta}{\beta}\boldsymbol{a}_k\right], \tag{4.66}$$

$$\boldsymbol{v}^{(0)}_{k+1} = \boldsymbol{v}_k + h[(1-\gamma)\boldsymbol{a}_k + \gamma\boldsymbol{a}^{(0)}_{k+1}]\,. \tag{4.67}$$

□

The expression for the tangent geometric stiffness matrix is given by

$$\boxed{\begin{aligned} &D^{\mathrm{g}}\boldsymbol{\mathcal{F}}_{k+1}(\boldsymbol{d}^{(i)}_{k+1}) =: \boldsymbol{S}^{\mathrm{g}}_{k+1}(\boldsymbol{d}^{(i)}_{k+1})\,, \qquad \boldsymbol{S}^{\mathrm{g}}_{k+1} = [\boldsymbol{S}^{\mathrm{g}}_{AB,(k+1)}] \in \mathbb{R}^{3n\times 3n}\,, \\ &\boldsymbol{S}^{\mathrm{g}}_{AB,(k+1)}(\boldsymbol{d}^{(i)}_{k+1}) = \mathscr{L}_{k+1}\int_{]0,1[}\{\boldsymbol{Y}[N_A\boldsymbol{1}]\}^{\mathrm{T}}\{\boldsymbol{B}(\tilde{\boldsymbol{U}}^{h(i)}_{k+1})\boldsymbol{Y}[N_B\boldsymbol{1}]\}\,\mathrm{d}\xi^1 \in \mathbb{R}^{3\times 3}\,, \end{aligned}} \tag{4.68}$$

according to (4.35), and where $\mathscr{L}_{k+1} := \mathscr{L}(t_{k+1})$. The tangent stiffness matrix is given by

$$\boxed{\begin{aligned}&D^{\mathrm{m}}\boldsymbol{\mathcal{F}}_{k+1}(\boldsymbol{d}^{(i)}_{k+1}) =: \boldsymbol{S}^{\mathrm{m}}_{k+1}(\boldsymbol{d}^{(i)}_{k+1})\,, \qquad \boldsymbol{S}^{\mathrm{m}}_{k+1} = [\boldsymbol{S}^{\mathrm{m}}_{AB,(k+1)}] \in \mathbb{R}^{3n\times 3n}\,,\\ &\boldsymbol{S}^{\mathrm{m}}_{AB,(k+1)}(\boldsymbol{d}^{(i)}_{k+1}) = \mathscr{L}_{k+1}\int_{]0,1[}\{\mathfrak{D}(\tilde{\boldsymbol{U}}^{h(i)}_{k+1})[N_A\mathbf{1}]\}^{\mathrm{T}}\cdot\{\boldsymbol{\Lambda}(\tilde{\boldsymbol{\vartheta}}^{h(i)}_{k+1})\boldsymbol{C}\boldsymbol{\Lambda}^{\mathrm{T}}(\tilde{\boldsymbol{\vartheta}}^{h(i)}_{k+1})\mathfrak{D}(\tilde{\boldsymbol{U}}^{h(i)}_{k+1})\}\,\mathrm{d}\xi^1 \in \mathbb{R}^{3\times 3}\end{aligned}} \tag{4.69}$$

according to (4.37).

The reader is referred to Li [51] for a discussion on time discretization specifically based on the Newmark algorithm, which is used to produce the numerical results in Section 5.

5. Numerical examples

We present here results of numerical simulations of sliding beams undergoing large deformation and large overall motion. The examples are selected with emphasis placed on their important engineering applicability, and on their significance from the applied mechanics viewpoint. The numerical results are obtained using the space–time discretization procedure presented in Section 4. A sliding geometrically-exact beam element is implemented in the finite element analysis program (FEAP) developed by R.L. Taylor; a simplified version of FEAP is described in [52]. The program was run on a DEC 5000 workstation under the Ultrix 4.2 operating system. Throughout this section, linear or quadratic finite element functions are used for the spatial discretization (4.40), and the Newmark method (4.55)–(4.56), with $\beta = \frac{1}{4}$ and $\gamma = \frac{1}{2}$ for the time discretization. Uniformly reduced integration is used to evaluate the static residual force and the tangent stiffness matrix, while exact integration is used to evaluate all other matrices.

5.1. The spaghetti problem

As mentioned in Section 1, Carrier [8]'s study of the spaghetti problem (the dynamics of a cord being drawn into an orifice) was based on the linear string theory to model the cord. He observed that near the end of the motion 'the amplitude of the oscillation usually increases sufficiently so that the cord frequently 'slaps' the plate containing the orifice.' Anyone who had played with a handyman's retractable tape rule for measuring would have experienced the 'slapping' of the metallic tape on his hand when the tape is retracted quickly into its canister. Mansfield and Simmonds [33], motivated by the dynamics of papers in copy machines, provide a nice explanation to Carrier's observation: 'If the string has an initial transverse motion, the associated kinetic energy, in the linear theory employed by Carrier, does not change, so as the string moves into the hole, its kinetic energy is squeezed into an ever shrinking piece. On reaching the hole, the tail of the string must therefore have infinite transverse velocity.'

The slapping of the tail of a string under retrieval cannot be described using linear theory. However, none of the previous studies using non-linear theories exhibit the slapping phenomenon. The present example will do just that, using the proposed sliding geometrically-exact beam formulation (see Figs. 6 and 7).[23] We are considering here a highly flexible beam, with shear deformation accounted for, having large deformation and being retrieved into a prismatic joint. The beam has an initial undeformed length L = 10, with mechanical properties set to

$$A_p = 2\,, \qquad I_p = 10\,, \tag{5.1}$$

$$EA = 10\,000\,, \qquad GA_s = 10\,000\,, \qquad EI = 500\,. \tag{5.2}$$

The beam is uniformly discretized using 10 linear elements, i.e. n = 10 in (4.41). A uniformly reduced integration with one Gauss point is used for evaluating the static residual force $\boldsymbol{\mathcal{F}}_{k+1}$ in (4.59) and the

---

[23] The first author thanks his student, Kyle Thornton, for producing these figures.

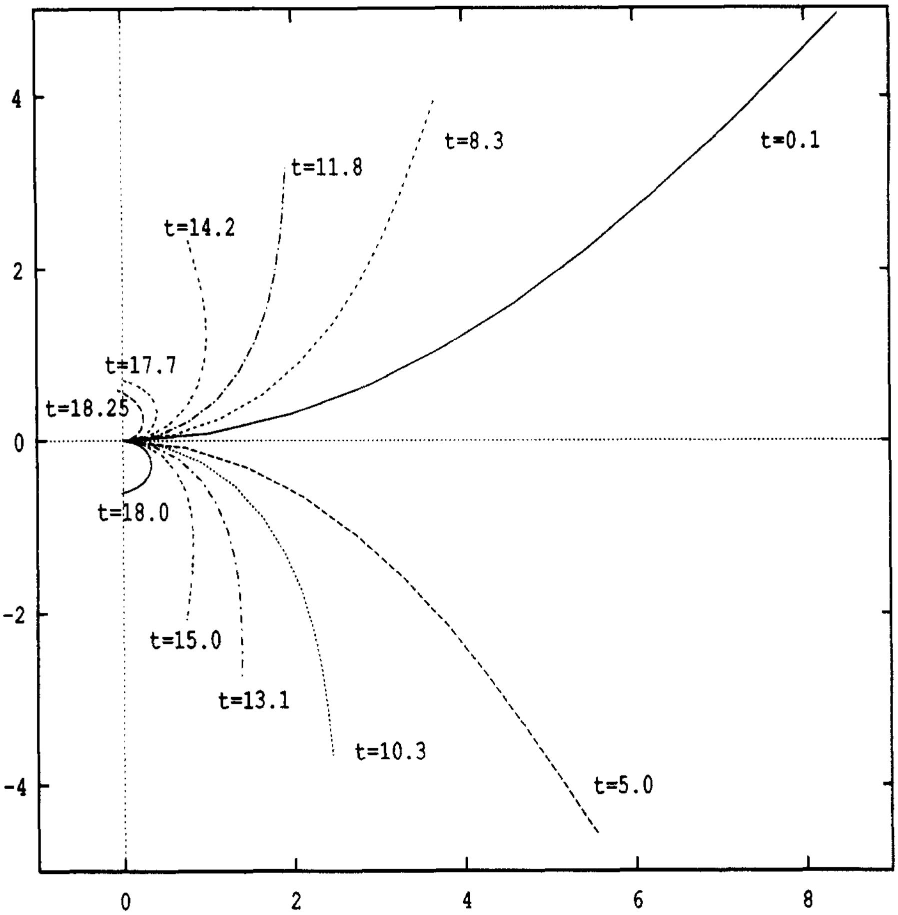

Fig. 6. Spaghetti problem. Sequence of snapshots of the beam deflected shapes at different time stations. Slapping phenomenon toward the end of the retrieval.

tangent stiffness matrix $D\mathcal{F}_{k+1}$ in $(4.61)_2$; all other matrices in $(4.61)_1$ are evaluated with two Gauss points. A transverse load with increasing magnitude is applied statically at the tip of the beam until the transverse tip deflection is close to 5, i.e. about half the initial length. Fig. 6 shows this initial deflected shape ($t = 0.1$) in the same scale as for the undeformed beam, with no magnification. The tip load is then completely released to begin the dynamic retrieval process. We implemented a quadratic sliding motion of the form

$$\mathcal{L}(t) = \frac{1}{2} a_1 t^2 + a_2 t + a_3 . \tag{5.3}$$

The following parameters

$$a_1 = 0 , \quad a_2 = -0.5 , \quad a_3 = 10 , \tag{5.4}$$

are used in the quadratic sliding motion (5.3) for the present example. Thus, according to (5.4), the beam is being retrieved at a constant rate of 0.5 unit of undeformed length per unit of time. We use a time step size of $h = 0.005$ for integrating the equations of motion over the time interval $[0, 20]$.

In addition to the initial deflected shape at $t = 0.1$, a sequence of snapshots of the deflected shapes of the beam at ten other time stations during the retrieval are shown in Fig. 6; the deflected shapes are plotted without artificial magnification of the displacement. In Fig. 6, one can clearly see the slapping phenomenon at the end of the retrieval. At this point, the beam tip begins to flip completely backward to face the orifice wall (or prismatic joint). The curvatures in the deformed shapes in Fig. 6 do not appear to change sign. However, a change in sign of the curvature of the deformed beam is clearly shown[24] in Fig. 7, which is a zoomed-in on a half-cycle of the slapping process toward the end of the

---

[24] Look at the deformed beam, e.g. at time $t = 18.635$ in Fig. 7.

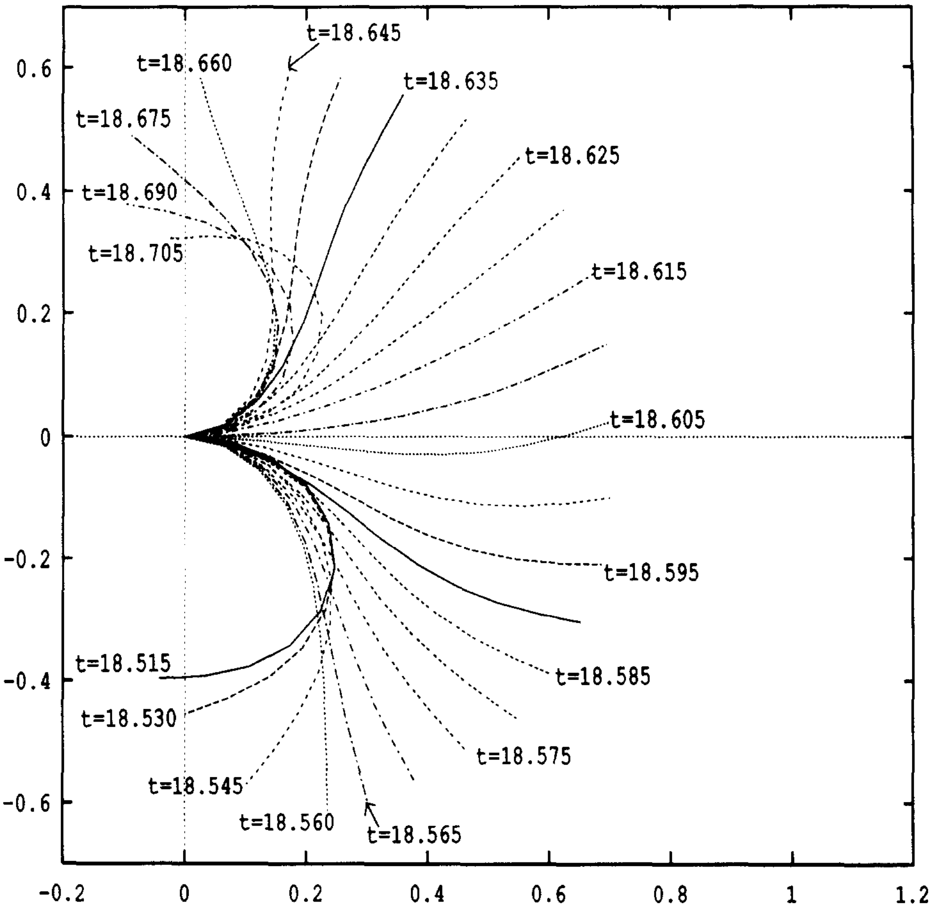

Fig. 7. Spaghetti problem. A zoomed-in on a half-cycle of slapping phenomenon for $t \in [18.515, 18.705]$. Sequence of snapshots of deformed shapes, exhibiting the change in sign of the curvature along the beam.

retrieval, from $t = 18.515$ to $t = 18.705$. The slapping phenomenon increases in frequency as the beam length gets shorter, as can be seen from the time history of the transverse displacement of the beam tip in Fig. 8. Rather than snapshots of the deformed shapes at discrete time stations, a better feeling of the dynamic motion in the present spaghetti problem can be obtained by looking at the continuous trace of the beam tip throughout the retrieval operation, as recorded in Fig. 9. For a diner who is improperly ingesting spaghetti, the quickening of the slapping of the tail of the spaghetti as the length gets shorter—as can be visualized from Fig. 9—will scatter tomato sauce on his shirt.

5.2. The reverse spaghetti problem

The term 'reverse spaghetti problem' refers to the reverse of the retrieval process, i.e. the deployment of the sliding beam. The sliding beam considered in this example has the same mechanical properties as in (5.1)–(5.2). We will consider the case without tip loading and the case with tip loading.

5.2.1. Without tip loading

The numerical simulations are performed using two different sliding (deployment) motions as defined by two different sets of coefficients a_i's for (5.3). Each deployment motion will be described shortly.

The sliding beam will be subjected to an initial transverse velocity distribution as part of the initial conditions. A practical situation corresponding to such initial transverse velocity distribution can be found, for example, in the deployment of flexible appendages from a satellite. As pointed out by Creamer [19] and others, when a long flexible appendage is axially deployed from a satellite canister, the functioning of the internal motor will produce some initial perturbations on the appendage. Such

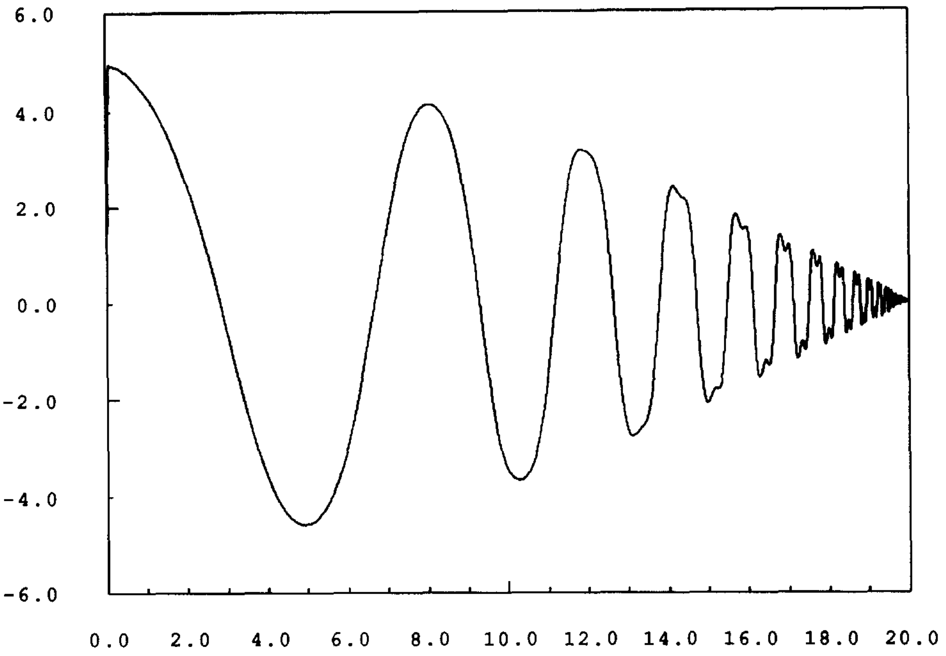

Fig. 8. Spaghetti problem. Time history of the transverse tip displacement. Increasing vibration frequency with the shortening of beam length.

perturbations can be modeled in simulations as an initial transverse displacement or transverse velocity distribution on the beam, or as an initial angular velocity imparted at the clamped end of the beam. In the present example, we choose a perturbation in velocity. In practical calculations, the sliding beam has a small initial length (i.e. a_3 is small). The initial transverse perturbation velocity is then distributed linearly on that small initial length of the beam.

The beam considered here has an initial length of $L = 10$, which is uniformly discretized using 10

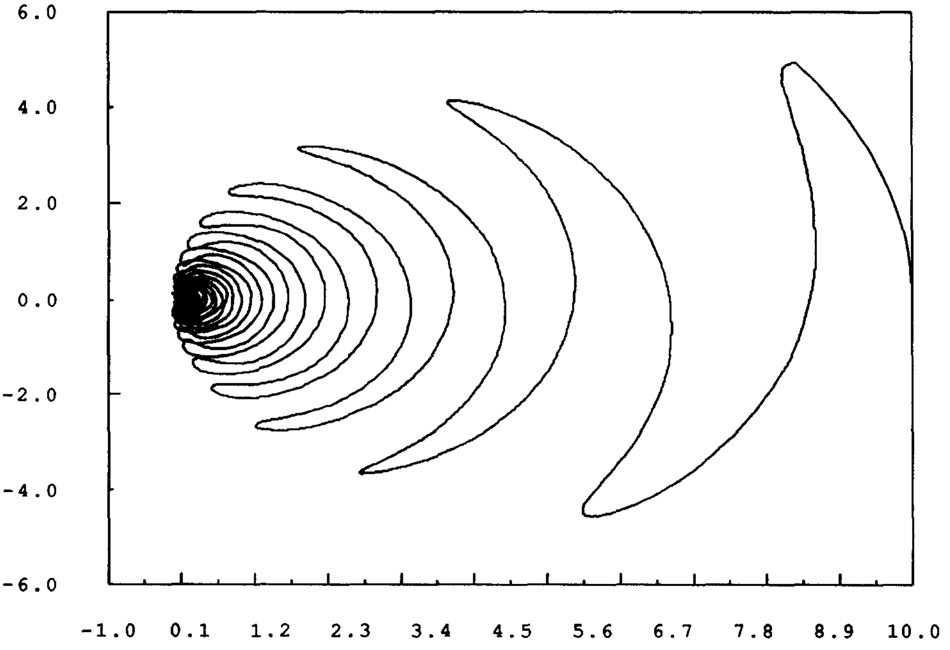

Fig. 9. Spaghetti problem. Motion of the beam tip throughout the retrieval. Slapping phenomenon with increasing frequency toward the end of the retrieval.

linear elements, i.e. $n = 10$ in (4.41). The numerical integration of the element matrices is as in Section 5.1 for the spaghetti problem. The initial transverse velocity is distributed linearly over the beam in ξ^1 coordinate according to

$$\left.\frac{\partial \tilde{u}^2(\xi^1, t)}{\partial t}\right|_{t=0} = c_1\xi^1 + c_2\,, \quad \forall \xi^1 \in [0, 1]\,, \tag{5.5}$$

with c_1 and c_2 being the parameters to be specified as input data. Note that in (5.5) the left-hand side is the velocity with respect to the ξ^1 coordinate (i.e. the partial time derivative of $\tilde{u}^2(\xi^1, t)$ keeping ξ^1 fixed) and not the actual velocity with respect to the material coordinate X^1 (i.e. the material time derivative of $\tilde{u}^2(\xi^1(X^1, t), t)$, keeping X^1 fixed). However, with the initial condition

$$\tilde{u}^2(\xi^1, 0) \equiv 0\,, \quad \forall \xi^1 \in]0, 1[\;\Rightarrow\; \frac{\partial \tilde{u}^2(\xi^1, 0)}{\partial \xi^1} \equiv 0\,, \quad \forall \xi^1 \in]0, 1[\tag{5.6}$$

it follows that

$$\frac{\mathrm{D}\tilde{u}^2(\xi^1, 0)}{\mathrm{D}t} = \frac{\partial \tilde{u}^2(\xi^1, 0)}{\partial \xi^1}\frac{\partial \phi^1(0)}{\partial t} + \frac{\partial \tilde{u}^2(\xi^1, 0)}{\partial t} = \frac{\partial \tilde{u}^2(\xi^1, 0)}{\partial t}\,. \tag{5.7}$$

In the computation, we set all components of the initial velocity $\boldsymbol{v}_0$ defined in $(4.52)_2$ to zero, except for the components

$$v^2_{0,A} = c_1\xi^1_A + c_2\,, \quad \text{for } A = 1, \ldots, n\,, \tag{5.8}$$

where ξ^1_A is the coordinate of node A defined in (4.41).

The first deployment motion corresponds to the parameters

$$a_1 = 0\,, \qquad a_2 = 0.5\,, \qquad a_3 = 0.1 \tag{5.9}$$

in the quadratic sliding-motion (5.3), i.e. the beam is being deployed with no acceleration, at a constant velocity of 0.5, and with an initial length of 0.1. The computation is performed over the time interval of $[0, 30]$. Thus, the final (undeformed) length of the sliding beam is 15. Compared to this value, the initial length of 0.1 is small. The linear distribution of the initial transverse perturbation velocity is chosen to be

$$\left.\frac{\partial \tilde{u}^2(\xi^1, t)}{\partial t}\right|_{t=0} = 0.02\xi^1\,, \quad \forall \xi^1 \in [0, 1]\,. \tag{5.10}$$

We use a time step size of $h = 0.01$ for the computation. The time history of the transverse displacement of the beam tip is given in Fig. 10, and the rotation of the section at the beam tip in Fig. 11. It can be seen from these two figures that, as expected, the amplitude of vibration increases as the beam slides out of the channel.

The second deployment motion corresponds to the parameters

$$a_1 = 0.0\,, \qquad a_2 = 0.5\,, \qquad a_3 = 0.01 \tag{5.11}$$

in the quadratic sliding-motion (5.3). A difference between the second deployment and the first deployment is the initial length of the beam, i.e. $a_3 = 0.01$ in (5.11) versus $a_3 = 0.1$ in (5.9). Another difference is in the initial transverse perturbation velocity coordinate

$$\left.\frac{\partial \tilde{u}^2(\xi^1, t)}{\partial t}\right|_{t=0} = 0.2\xi^1\,, \quad \forall \xi^1 \in [0, 1]\,. \tag{5.12}$$

However, the magnitude of the velocity perturbation as measured by the area of the velocity distribution curve (i.e. $V_{\max} \times a_3 = 0.2 \times 0.01$) remains the same as in the first deployment (i.e. 0.02×0.1). The computation is performed with a time step size of $h = 0.002$ over a time interval of $[0, 10]$. Fig. 12 shows the time history of the transverse displacement at the beam tip, with increasing vibration amplitude. Comparing Fig. 12 to its counterpart Fig. 10, one can see that the amplitude of vibration at $t = 10$ is larger in the second deployment. In Fig. 13, we superpose the transverse

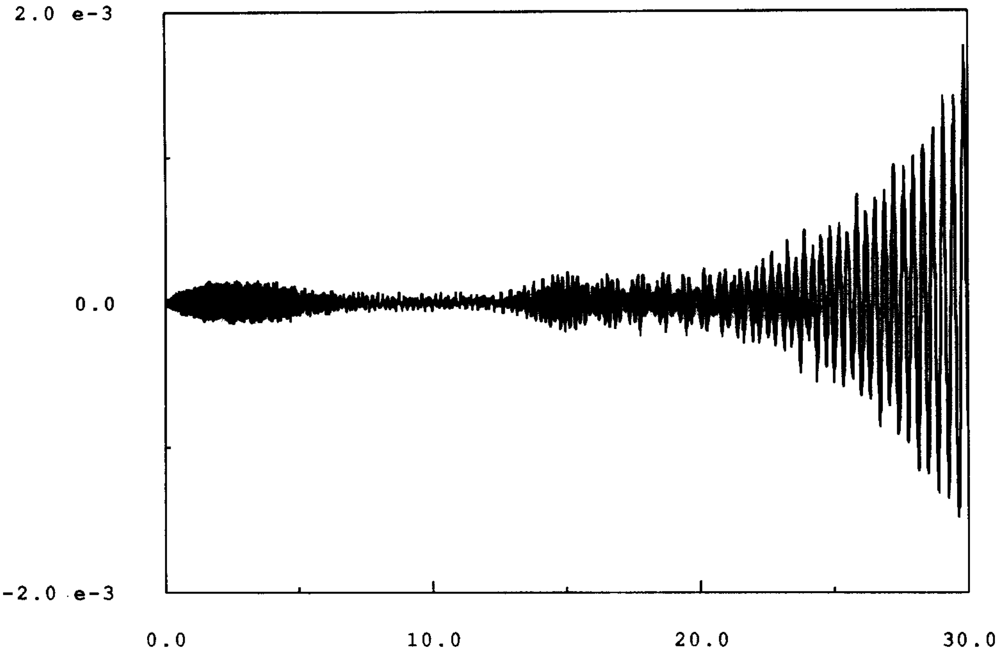

Fig. 10. Reverse spaghetti problem without tip loading. First deployment. Time history of transverse tip deflection.

displacement of the beam tip during the time interval [0, 1] and during the time interval [8, 9] to display the increase in the vibration period with the increase in beam length.

5.2.2. With transverse tip loading

To simulate a load that the sliding beam may be required to carry at its tip, we now impose a vertical, constant, concentrated force at the beam tip, and this without an initial velocity perturbation. The beam tip is expected to vibrate about the static deflection position, as recorded in Fig. 14. Unlike the previous

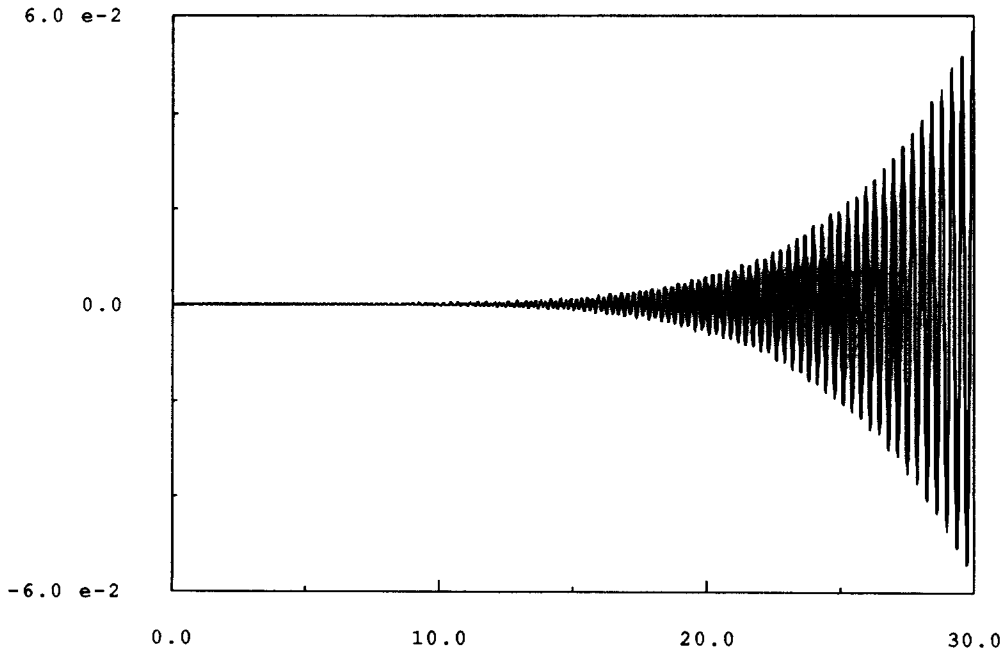

Fig. 11. Reverse spaghetti problem without tip loading. First deployment. Time history of rotation of tip cross section.

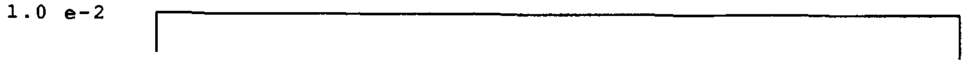

where L_{final} and ψ_{final} are the final length and the final angle of rotation of the joint.[27] Here, we prescribe the following motion parameters

$$\begin{aligned} &L_{\text{final}} = 10\,, \quad && a_2 = 0.4\,, \quad && L_{\text{initial}} = 0.001\,, \\ &\Psi_{\text{final}} = 2.5\pi\,, && b_2 = 0.4\,. && \end{aligned} \tag{5.19}$$

Fig. 15 depicts the time history of the angle $\psi(t)$ as expressed by (5.18), where it can be seen that the angle $\psi(t)$ rises rapidly to an angle of about 360° (i.e. ≈6 rad), at about 4 computational time units, then slows down to reach the angle 450° asymptotically. The time history of the effective length $\mathcal{L}(t)$ described by (5.17) is similar.

The mechanical properties of the beam in the present example are the same as in (5.1)–(5.2), except for a stiffer bending stiffness $EI = 800$. The computation is performed with a time step size of $h = 0.01$ over the time interval $[0, 40]$. A sequence of snapshots of the deformed shapes of the beam at different time stations is depicted in Fig. 16, where large deformation in the beam can be noticed with little difficulty even though there is no magnification of the deformation. In particular, it can be observed that the beam bends backward as the base rotates from $\psi = 0°$ through to about 360°; then the beam bends forward as the base rotation slows down from 360° to 450°; finally, vibration with large amplitude can be seen when the rotation comes virtually close to a halt at $450° = 2.5\pi$. Fig. 17, depicting the trace (or orbit) of the beam tip, provides a better visualization of the simultaneous deployment and large angle maneuver in this example.

With respect to the shadow beam (see Fig. 3) or the nominal position of the beam, the beam tip experiences a transverse motion with time as depicted in Fig. 18 for the time interval $[0, 40]$: Indeed, as observed above, the beam bends backward (negative values) when the rotation angle $\psi(t)$ is between 0° and approximately 360°, or equivalently the time parameter t is between 0 and approximately 4 computational time units (see Fig. 15). The amplitude of displacement during this time interval is small compared to that in subsequent vibration; this is because the effective length $\mathcal{L}$ of the beam in this time interval is smaller than the beam length one in subsequent time interval. At the stop angle $450° = 2.5\pi$ rad, the beam settles into a steady-state vibration regime with a rather large amplitude of about 2 (recall that the fully extended length of the beam is 10).

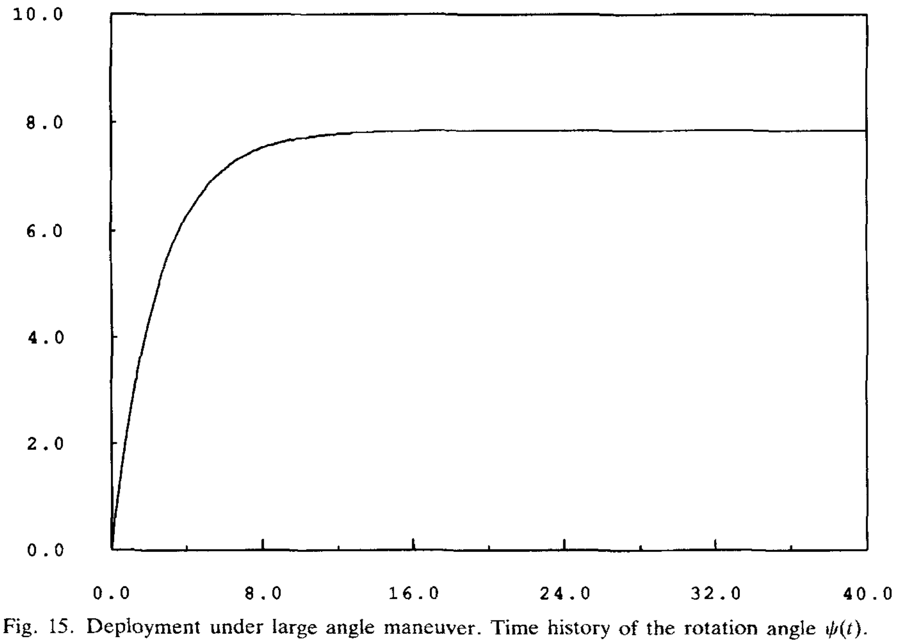

Fig. 15. Deployment under large angle maneuver. Time history of the rotation angle $\psi(t)$.

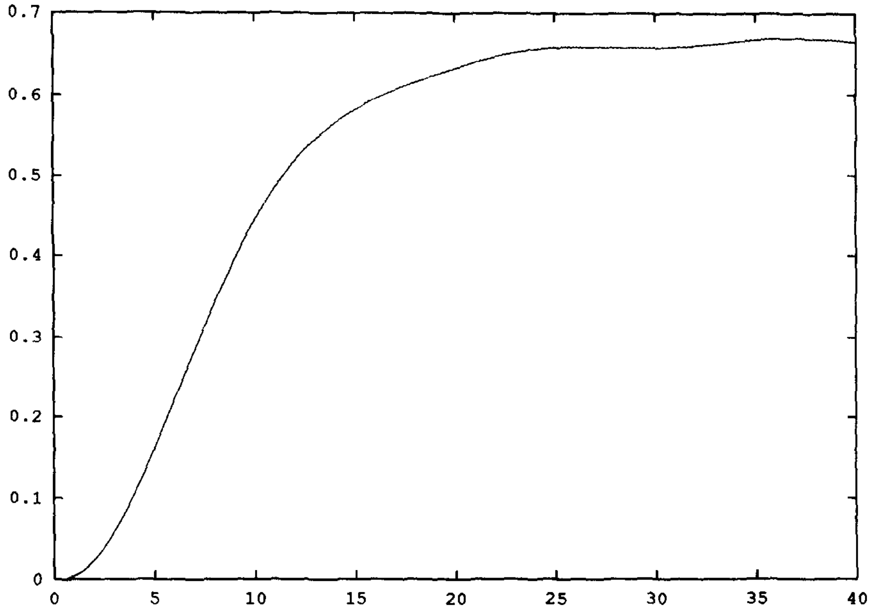

Fig. 14. Reverse spaghetti problem with transverse tip loading. Transverse displacement of beam tip versus time.

to produce Fig. 14.[25] With the exponential sliding motion (5.13), the sliding beam starts from its initial length a_3, and approaches asymptotically its final length a_1. The computation is performed over the time interval $[0, 40]$ with a time step size of $h = 0.005$. The transverse load has its amplitude increased linearly over the interval $[0, 0.1]$, and remained constant over the remainder of the time interval $]0.1, 40]$: Thus, all components of the applied force $F^{\text{appl}}(t)$ in (4.51) are zero except for

$$F_n^{2,\text{appl}}(t) = \begin{cases} 30t & \text{for } t \in [0, 0.1]\,, \\ 1 & \text{for } t \in \,]0.1, 40]\,, \end{cases} \tag{5.15}$$

where $n = 10$ is the node number at the beam tip. There is a sudden decrease in the load amplitude from 3 to 1 at $t = 0.1$. The maximum deflection as shown in Fig. 14 compares well with the static deflection of the tip for an Euler–Bernoulli cantilever beam under a unit tip load

$$\frac{PL^3}{3EI} \approx 0.67\,, \tag{5.16}$$

where $P = 1$, $L = 10$ and $EI = 500$.

5.3. Deployment under large angle maneuver

The sliding beam is subjected to a simultaneous deployment motion and large overall rotation (large angle maneuver) of the prismatic joint about the joint orifice.[26] This problem of engineering significance is encountered in many robotic systems and spacecraft systems, as indicated in Section 1. Simo and Vu-Quoc [36] present results for the case of beams with fixed lengths. We consider here a combined deployment motion $\mathscr{L}(t)$ and large overall rotation angle $\psi(t)$ (defined in (2.8) and in Fig. 4) of the exponential form as follows

$$\mathscr{L}(t) = L_{\text{final}}[1 - \exp(-a_2 t)] + L_{\text{initial}}\,, \tag{5.17}$$

$$\psi(t) = \psi_{\text{final}}[1 - \exp(-b_2 t)]\,, \tag{5.18}$$

---

[25] The first author thanks his students, Kyle Thornton and Hui Deng, for their help in regenerating the correct results presented here.

[26] More general motions of the prismatic joint can be prescribed as noted in Remark 3.2.

where L_{final} and ψ_{final} are the final length and the final angle of rotation of the joint.[27] Here, we prescribe the following motion parameters

$$\begin{aligned} &L_{\text{final}} = 10\,, \quad && a_2 = 0.4\,, \quad && L_{\text{initial}} = 0.001\,, \\ &\Psi_{\text{final}} = 2.5\pi\,, && b_2 = 0.4\,. && \end{aligned} \tag{5.19}$$

Fig. 15 depicts the time history of the angle $\psi(t)$ as expressed by (5.18), where it can be seen that the angle $\psi(t)$ rises rapidly to an angle of about 360° (i.e. ≈ 6 rad), at about 4 computational time units, then slows down to reach the angle 450° asymptotically. The time history of the effective length $\mathscr{L}(t)$ described by (5.17) is similar.

The mechanical properties of the beam in the present example are the same as in (5.1)–(5.2), except for a stiffer bending stiffness $EI = 800$. The computation is performed with a time step size of $h = 0.01$ over the time interval $[0, 40]$. A sequence of snapshots of the deformed shapes of the beam at different time stations is depicted in Fig. 16, where large deformation in the beam can be noticed with little difficulty even though there is no magnification of the deformation. In particular, it can be observed that the beam bends backward as the base rotates from $\psi = 0°$ through to about 360°; then the beam bends forward as the base rotation slows down from 360° to 450°; finally, vibration with large amplitude can be seen when the rotation comes virtually close to a halt at $450° = 2.5\pi$. Fig. 17, depicting the trace (or orbit) of the beam tip, provides a better visualization of the simultaneous deployment and large angle maneuver in this example.

With respect to the shadow beam (see Fig. 3) or the nominal position of the beam, the beam tip experiences a transverse motion with time as depicted in Fig. 18 for the time interval $[0, 40]$: Indeed, as observed above, the beam bends backward (negative values) when the rotation angle $\psi(t)$ is between 0° and approximately 360°, or equivalently the time parameter t is between 0 and approximately 4 computational time units (see Fig. 15). The amplitude of displacement during this time interval is small compared to that in subsequent vibration; this is because the effective length $\mathscr{L}$ of the beam in this time interval is smaller than the beam length one in subsequent time interval. At the stop angle $450° = 2.5\pi$ rad, the beam settles into a steady-state vibration regime with a rather large amplitude of about 2 (recall that the fully extended length of the beam is 10).

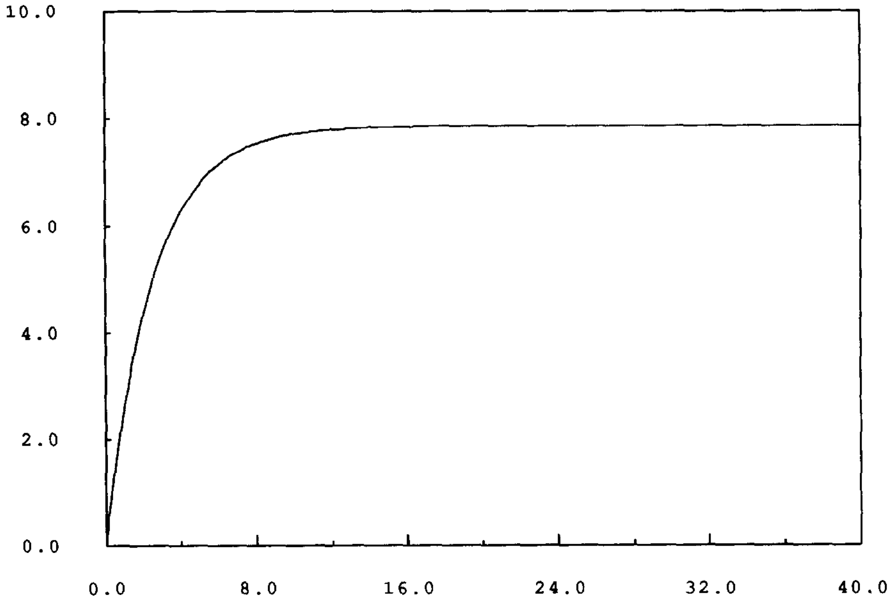

Fig. 15. Deployment under large angle maneuver. Time history of the rotation angle $\psi(t)$.

---

[27] By the definition of $\psi(t)$ and of ϑ_0 as shown in Fig. 4, we do not have to account for the constant ψ_{initial}, which is in fact ϑ_0, in (5.18). The angle ϑ_0 is, on the other hand, determined by the initial configuration of the beam.

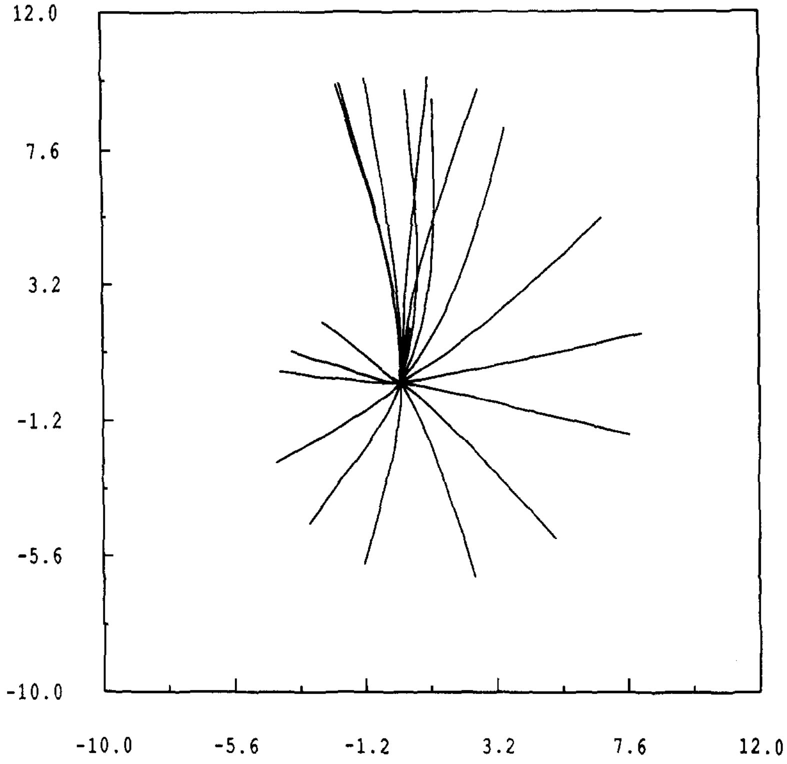

Fig. 16. Deployment under large angle maneuver. Sequence of snapshots of deformed shapes at different time stations. $EI = 800$.

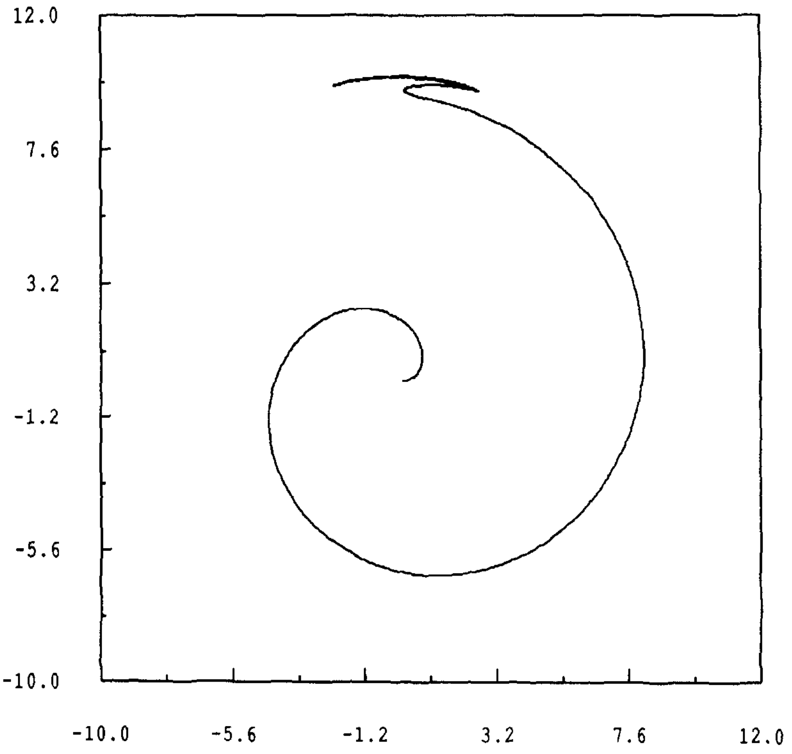

Fig. 17. Deployment under large angle maneuver. Trace (or orbit) of the beam tip.

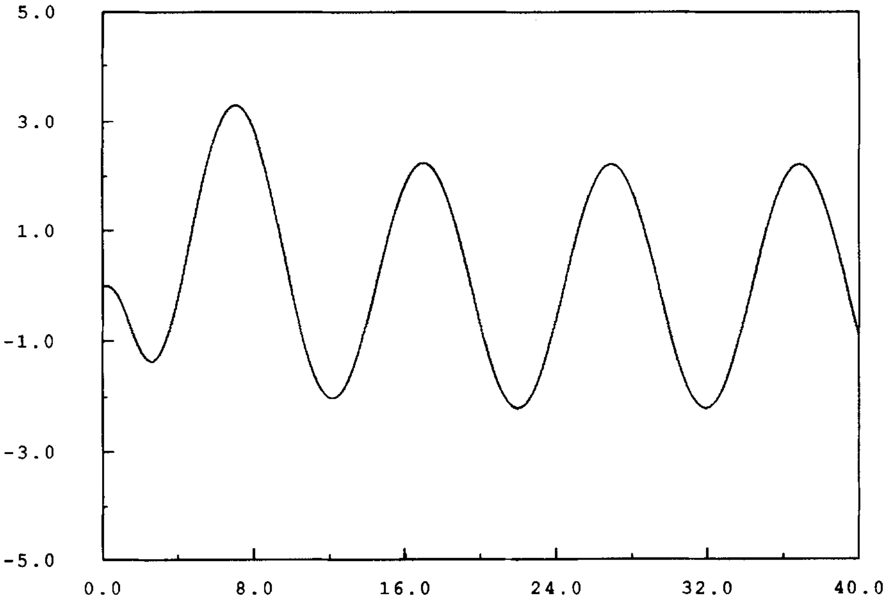

Fig. 18. Deployment under large angle maneuver. Time history of the transverse displacement of the beam tip with respect to the nominal position (shadow beam).

Using the more flexible beam of previous examples (i.e. with $EI = 500$), subjected to the same combined deployment and large angle maneuver, one can see clearly the large deformation in Fig. 19.

5.4. Parametric resonance

The beam is now subjected to a sinusoidal sliding motion of the form

$$\mathscr{L}(t) = \mathscr{L}_0 + \mathscr{L}_1 \sin \omega t . \tag{5.20}$$

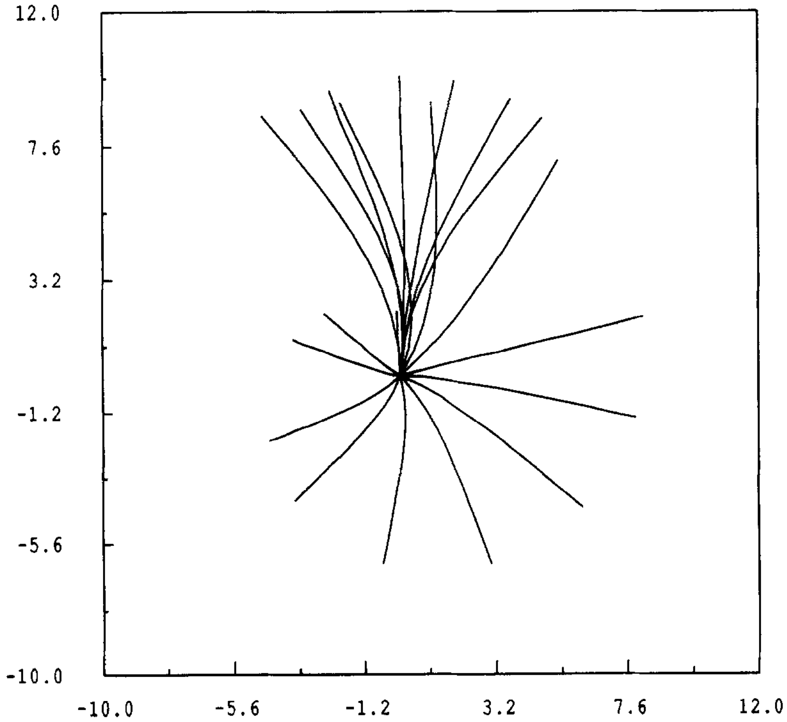

Fig. 19. Deployment under large angle maneuver. Sequence of snapshots of deformed shapes at different time stations. $EI = 500$.

Depending on the parameters $\mathscr{L}_0, \mathscr{L}_1, \omega$, the dynamic behavior of the beam can change drastically. Resonance occurs for a given set of beam properties and appropriate parameters in (5.20). As mentioned in Section 1, stability analysis of periodically sliding Euler–Bernoulli beams were performed in [22–24]; numerical simulations of a more complex Euler–Bernoulli model were given in [26]. We provide here some results on parametric resonance obtained with the present geometrically-exact sliding beam. A general feature in the results obtained with geometrically-exact theory is that, unlike results from stability analyses using linearized theories where the displacement of the beam tip at resonance blows up to infinity, we have here contained resonance, i.e. even though there are strong vibrations with large amplitude at resonance, the magnitude of the displacement remains finite. Contained resonance is a consequence of fully-non-linear theory. It follows that the system would not have clear-cut stability regions and boundaries—within which the displacement is finite, and beyond which the displacement blows up to infinity—as obtained with linearized theories (see e.g. [23, 24]). On the other hand, considerable difficulties are encountered in the numerical integration (convergence failure in Newton iterative process) when the dynamic behavior of the sliding beam changes drastically. Two sets of numerical simulations are performed.

5.4.1. *First set of simulations*

The beam mechanical properties are chosen to be

$$A_\rho = 12.23 , \qquad I_\rho = 0.001631 , \tag{5.21}$$

$$EA = 2\,049\,840\,000 , \qquad GA_s = 694\,861\,017 , \qquad EI = 273\,312 . \tag{5.22}$$

The beam is discretized uniformly using 5 quadratic elements, instead of 10 linear elements as in previous examples. The number of nodes (11) remains, however, the same as in previous examples. A uniformly reduced integration with 2 Gauss points were used for the tangent stiffness matrix in $(4.61)_2$; an integration with 3 Gauss points is used for all other matrices in $(4.61)_1$. The sliding-motion parameters in (5.20) are taken to be

$$\mathscr{L}_0 = 16 , \qquad \mathscr{L}_1 = 6 , \qquad \omega \in \left[\frac{\pi}{6}, \frac{9\pi}{10} \right] . \tag{5.23}$$

An initial perturbation in displacement and velocity is introduced to induce subsequent vibrations as follows. At $t = 0$, we have $\mathscr{L}(0) = 16$; the mass matrix at $t = 0$ in (4.61) is $\boldsymbol{M}_0$, and tangent material stiffness matrix is $\boldsymbol{S}_0^{\mathrm{m}}$ according to (4.69). Let $\boldsymbol{\Psi}_1$ be the eigenvector corresponding to the lowest eigenvalue μ_1 of the eigenvalue problem

$$[\boldsymbol{M}_0 - \mu \boldsymbol{S}_0^{\mathrm{m}}] \boldsymbol{\Psi} = 0 , \tag{5.24}$$

with $\boldsymbol{\Psi}_1$ being normalized so that it has a unit transverse displacement at the tip. The initial (perturbation) displacement $\boldsymbol{d}_0$ and velocity $\boldsymbol{v}_0$ for the equation of motion (4.53) are as follows

$$\boldsymbol{d}_0 = -0.01 \boldsymbol{\Psi}_1 , \qquad \boldsymbol{v}_0 = 0.0005 \boldsymbol{\Psi}_1 . \tag{5.25}$$

Specifically, for complete documentation, we use the following numerical values for the initial perturbation in displacement (Table 1) and in velocity (Table 2).[28]

The computation is carried out over the time interval [0, 30], with time step sizes varying from 0.01 to 0.004. Fig. 20(a, b) is obtained with $h = 0.01$ over the whole time interval [0, 30]; Fig. 20(c,d) and Fig. 21(a,b) with $h = 0.01$ over [0, 20], then with $h = 0.004$ over [20, 30]. For $\omega = 0.90\pi$, the last time-stepping strategy leads to a numerical instability (i.e. an increase of the amplitude without bounds) at about time $t = 22$ as shown in Fig. 21(c). A further refined time-stepping strategy[29] of $h = 0.01$ over [0, 10], then $h = 0.005$ over [10, 20], then $h = 0.0025$ over [20, 30] still leads to a numerical instability at about time $t = 24$ (Fig. 21(c)). Finally, a converged solution over the interval [0, 30] for $\omega = 0.9\,\pi$ shown

---

[28] From Table 1, it can be seen that the transverse tip displacement in $\boldsymbol{\Psi}_1$ is *not* exactly one (0.99935) due to round-off error.

[29] For the present set of simulations, from here on, the results were generated by two students of the first author, Kyle Thornton and Hui Deng. Their help is appreciated.

Table 1
Parametric resonance. Initial perturbation in displacement

Node	u_0^1	u_0^2	θ
1	0.0	0.0000000	0.0000000
2	0.0	−0.0001681	−0.0002051
3	0.0	−0.0006401	−0.0003798
4	0.0	−0.0013673	−0.0005243
5	0.0	−0.0023022	−0.0006396
6	0.0	−0.0033991	−0.0007270
7	0.0	−0.0046148	−0.0007887
8	0.0	−0.0059110	−0.0008280
9	0.0	−0.0072548	−0.0008491
10	0.0	−0.0086210	−0.0008570
11	0.0	−0.0099935	−0.0008580

in dotted line in Fig. 21(c) is obtained with a refined time-stepping strategy of $h = 0.005$ over [0, 10], then $h = 0.0025$ over [10, 20], and then $h = 0.00125$ over [20, 30]. One can see that even though the previous two time-stepping strategies lead to numerical instability beyond a certain time, the responses are similar to the converged solution obtained from the last time-stepping strategy. The same can also be seen from Fig. 22 describing the projection of the position of the beam tip along the axial direction as a function in time. Fig. 22 gives an idea on the sliding motion defined in (5.20), particularly at the beginning of the motion, i.e. prior to $t = 21$, where the large transverse displacement toward the end does not have yet a significant effect, at this scale, on the axial position of the beam tip.

Thus, it can be seen from the results that as the sliding frequency ω in (5.23) varies, the dynamic behavior of the beam changes back and forth through various moods from quiescent to agitated, as testified by Figs. 20 and 21. At $\omega = 0.5\pi$ rad/s, Fig. 21(c), the vibration amplitude of the beam tip increase with time to a relatively large value. At $\omega = 0.9\pi$ rad/s, Fig. 21(c), large amplitude vibration is observed within a short time. The complex pattern of combined large transverse deflection and sliding motion, together with the trace of the beam tip, are delineated in Fig. 23 (without magnification of the transverse deflection as compared to beam geometry), for the time interval [19.6, 24.6]. Subharmonic resonance can be seen by comparing Fig. 21(c) and Fig. 22: Toward the end of the time interval [0, 30], the fundamental frequency of transverse vibration is about half of the sliding excitation frequency $\omega = 0.9\pi$ rad/s. At this sliding excitation frequency, the amplitude of transverse vibration becomes very large (greater than 10) as compared to the length of the beam. However, due to the full non-linearity of the model, the transverse vibration remains bounded (contained resonance), as shown in Fig. 24 (without magnification), instead of increasing without bounds as would be predicted from a linearized formulation. At the beginning, since the transverse vibration is small, the motion of the beam remains close to the horizontal axis, and the beam (underformed) length varies between 10 and 22. The beam

Table 2
Parametric resonance. Initial perturbation in velocity

Node	$\dot{u}_0^1$	$\dot{u}_0^2$	$\dot{\theta}$
1	0.0	0.0000000	0.0000000
2	0.0	0.0000084	0.0000103
3	0.0	0.0000320	0.0000190
4	0.0	0.0000684	0.0000262
5	0.0	0.0001151	0.0000320
6	0.0	0.0001700	0.0000363
7	0.0	0.0002307	0.0000394
8	0.0	0.0002956	0.0000414
9	0.0	0.0003627	0.0000425
10	0.0	0.0004310	0.0000428
11	0.0	0.0004997	0.0000429

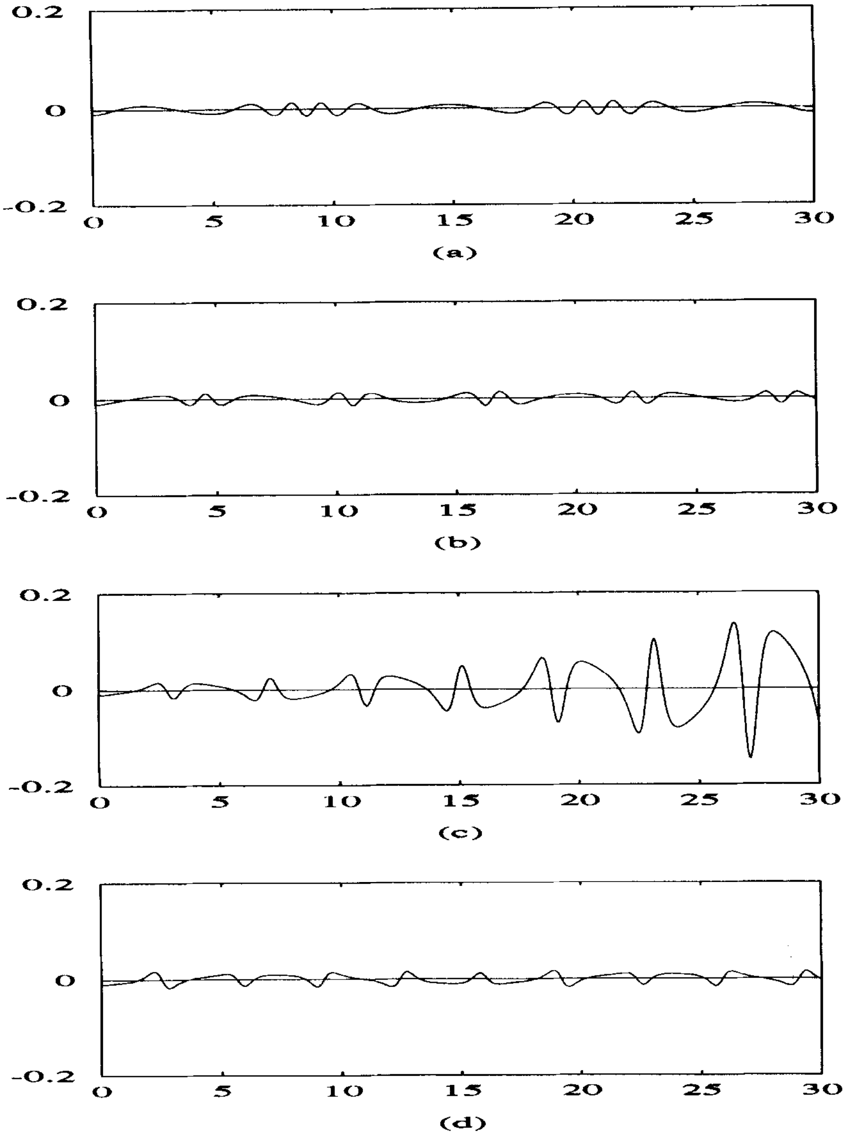

Fig. 20. Parametric resonance. First set of simulations. (a) $\omega = \pi/6$, (b) $\omega = \pi/3$, (c) $\omega = 0.5\pi$ and (d) $\omega = 0.6\pi$.

tip can be seen to detach completely from the horizontal axis toward the end; the amplitude of transverse vibration amplitude exceeds 10. The origin of the coordinate system in Figs. 23 and 24 is the location of the orifice of the beam channel.

5.4.2. Second set of simulations

We now decrease the mass per unit underformed length A_ρ and the mass moment of inertia I_ρ of the cross section by ten times to

$$A_\rho = 1.223\,, \qquad I_\rho = 0.0001631\,. \tag{5.26}$$

The frequency of sliding motion ω is varied between 2π rad/s and 3π rad/s. The same spatial discretization and numerical integration are used as in the first set of simulations. The computation is carried over a time interval of $[0, 20]$ with the time step size $h = 0.005$ to produce Figs. 25 and 26. Similar to the first set of simulations, although with a different characteristic, the dynamic behavior of the sliding beam goes through various moods from quiescent to agitated, depending on the value of ω.

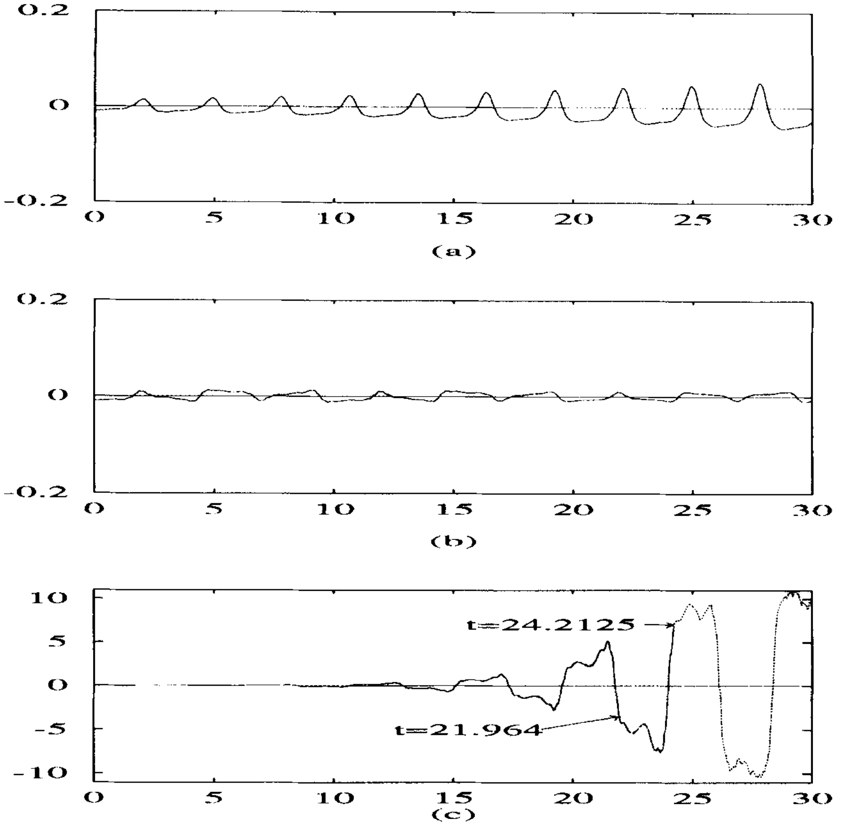

Fig. 21. Parametric resonance. First set of simulations (Contd.). (a) $\omega = 0.7\pi$, (b) $\omega = 0.8\pi$, and (c) $\omega = 0.9\pi$ (Dotted line: Converged solution with the third time-stepping strategies; the beginning of numerical instability is indicated for the first two time-stepping strategies).

In particular, numerical difficulties are encountered for the values of ω at 2.6π rad/s and at 2.7π rad/s as shown in Fig. 26(b, c): The dynamic response is apparently very quiescent for a long period of time; then at a finite time, a failure in the numerical convergence occurs for the chosen time step size. In Fig. 26(d), resonance can be observed for $\omega = 2.8\pi$ rad/s, with an apparent blow-up in the numerical results at about $t = 8$.

To investigate the behavior of the system for the last three values of ω, we decrease the time step size using a number of different time-stepping strategies.[30] For the two cases with $\omega = 2.6\pi$ rad/s and

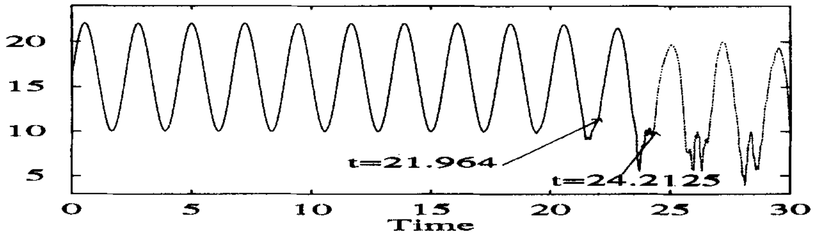

Fig. 22. Parametric resonance. First set of simulation (Contd.). Position of beam tip along the axial direction versus time. Dotted line: Converged solution with the third time-stepping strategies. The beginning of numerical instability is indicated for the first two time-stepping strategies.

---

[30] From here on, the two students of the first author, Kyle Thornton and Hui Deng, helped in generating the results presented. Their help is very much appreciated.

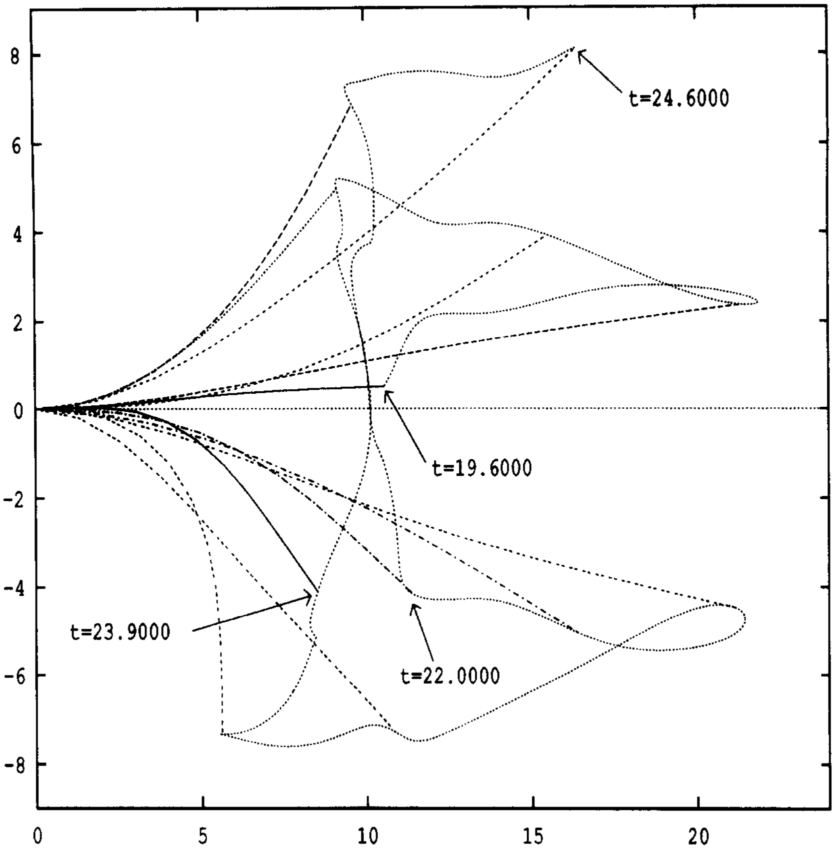

Fig. 23. Parameteric resonance. First set of simulation (Contd.). Deformed shapes and trace of beam tip in the time interval [19.6, 24.6] for $\omega = 0.9\pi$ rad/s.

$\omega = 2.7\pi$ rad/s, it is sufficient to halve the time step size (i.e. $h = 0.0025$) to have numerical convergence over the whole interval [0, 20]. The results, presented in Fig. 27, can be seen to be similar to that in Fig. 26(a).

The resonance case with $\omega = 2.8\pi$ rad/s is more difficult, and does take some trial and error to arrive at an acceptable strategy within the time interval of interest, i.e. [0, 20]. We made maximum use of the restart capability of FEAP to store partial results corresponding to subintervals of [0, 20]. We begin with a time step size of $h = 0.0003125$, and decrease it to $h = 0.0000390625$ at the end. The acceptable time-stepping strategy is as follows: (i) $h = 0.0003125$ in the time interval [0, 10] (or 32 000 steps), (ii) $h = 0.000078125$ (i.e. divided by four) in the time interval]10, 15] (or 64 000 steps), (iii) $h = 0.0000390625$ (i.e. divided by two) in the time interval]15, 20] (or 128 000 steps).

The results are presented in Figs. 28 to 31. The time histories of the axial displacement and the transverse displacement of the beam tip are given in Fig. 28(a, b), respectively. In Fig. 28(a), one can see that the beam tip follow the prescribed sliding motion (5.20) and (5.23) up to about time $t = 11$. Meanwhile, the amplitude of the transverse displacement increase gradually as shown in Fig. 28(b). Between $t = 11$ and $t = 16$, considerable non-linear effects can be observed in both axial displacement and transverse displacement of the beam tip. The trace of the beam tip within the time interval [0, 16.29] is plotted in Fig. 29,[31] where it can be seen that the beam tip follows the prescribed axial sliding motion at the beginning, with a gradual increase in the amplitude of the transverse displacement to the same order of the beam length. While Fig. 29 has a similar feature as Fig. 24, the trace of the beam tip becomes wild beyond the time $t = 16$ as shown in Fig. 30. A sequence of snapshots of the

---

[31] The same scale is used for both axial and transverse directions. The orifice of the channel is at the origin of the coordinate system.

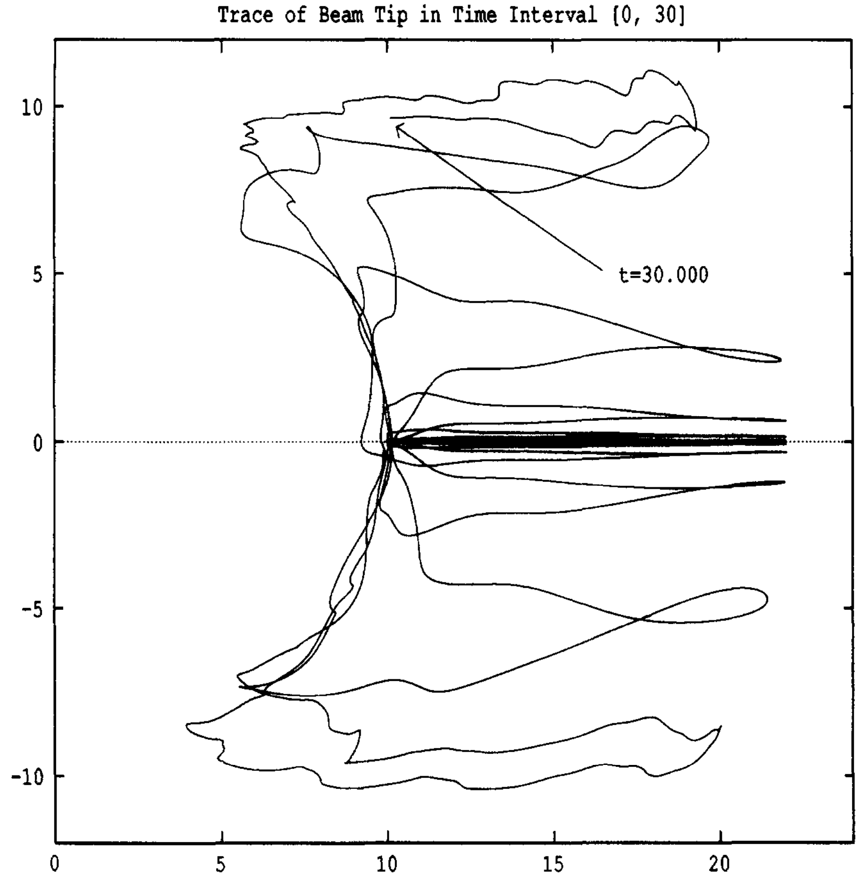

Fig. 24. Parametric resonance. First set of simulation (Contd.). Trace of beam tip in time interval [0, 30] for $\omega = 0.9\pi$ rad/s.

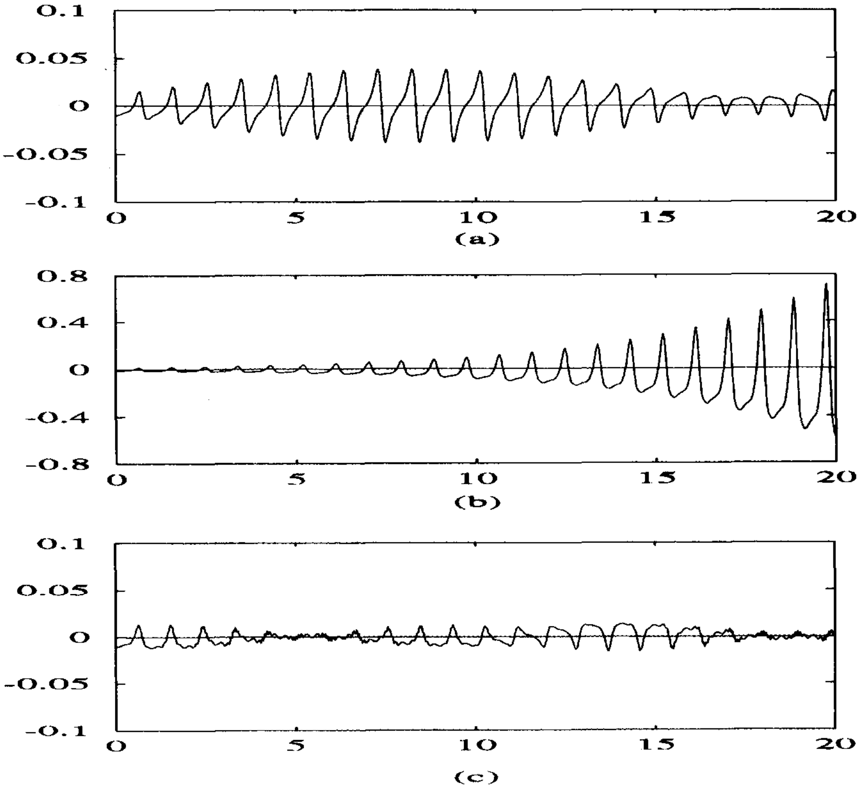

Fig. 25. Parametric resonance. Second set of simulations. Time step size $h = 0.005$. (a) $\omega = 2.1\pi$, (b) $\omega = 2.2\pi$ and (c) $\omega = 2.3\pi$.

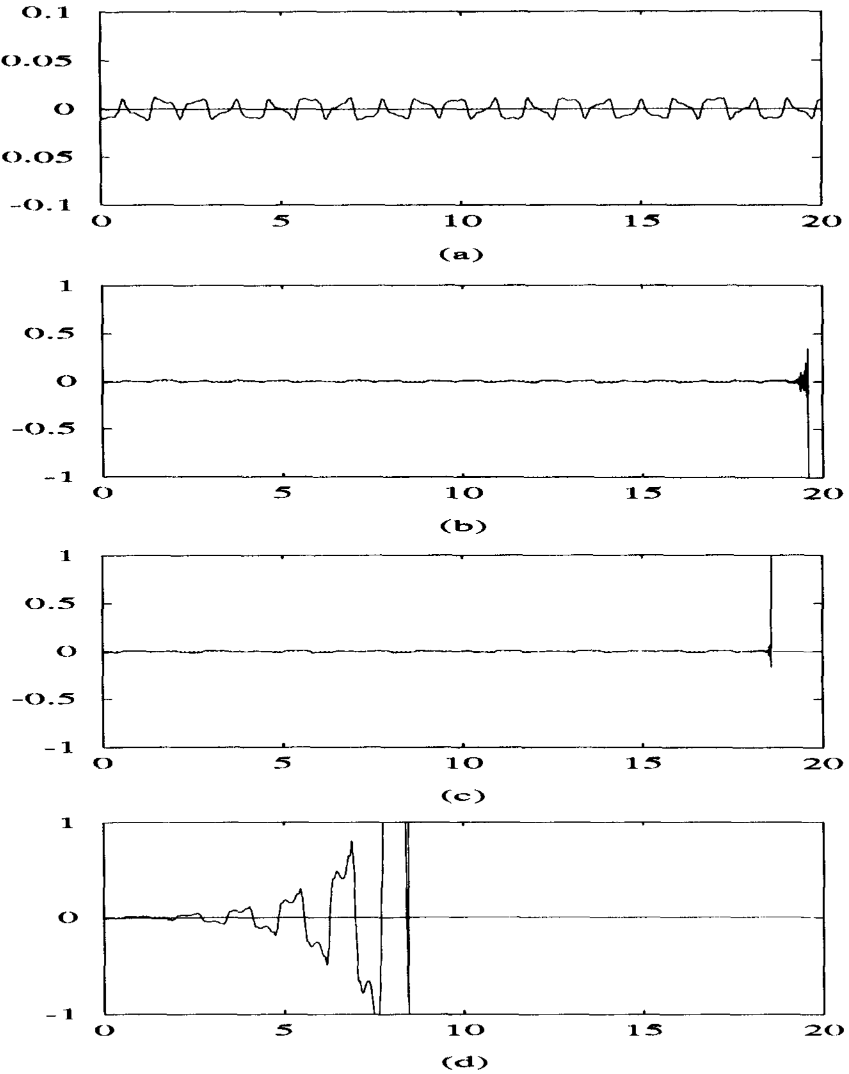

Fig. 26. Parametric resonance. Second set of simulations (Contd.). Time step size $h = 0.005$. (a) $\omega = 2.5\pi$, (b) $\omega = 2.6\pi$, (c) $\omega = 2.7\pi$ and (d) $\omega = 2.8\pi$.

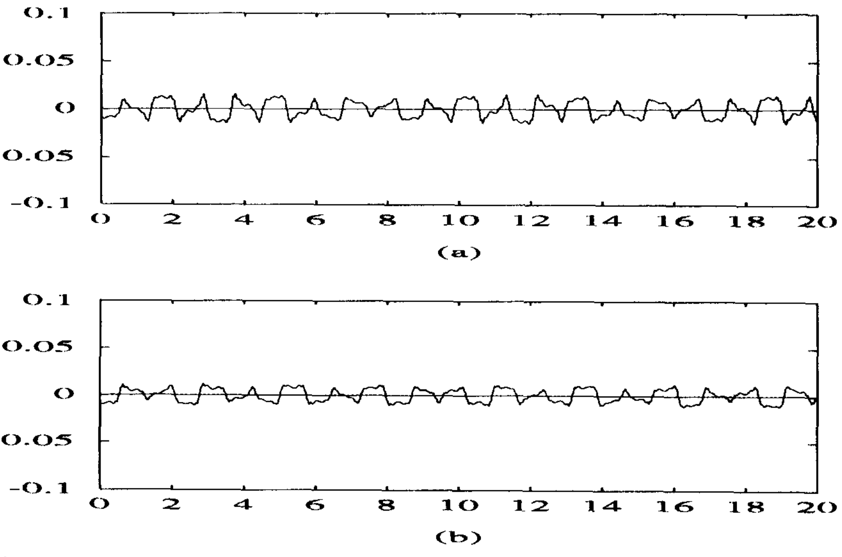

Fig. 27. Parametric resonance. Second set of simulations (Contd.). Time step size $h = 0.0025$. (a) $\omega = 2.6\pi$, (b) $\omega = 2.7\pi$.

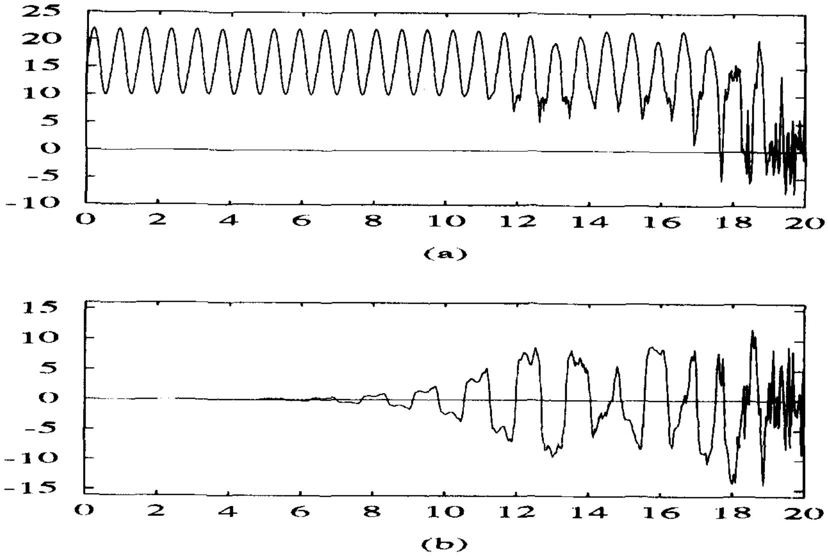

Fig. 28. Parametric resonance. Second set of simulations (Contd.). $\omega = 2.8\pi$. Time histories of beam tip displacement: (a) axial, (b) transverse.

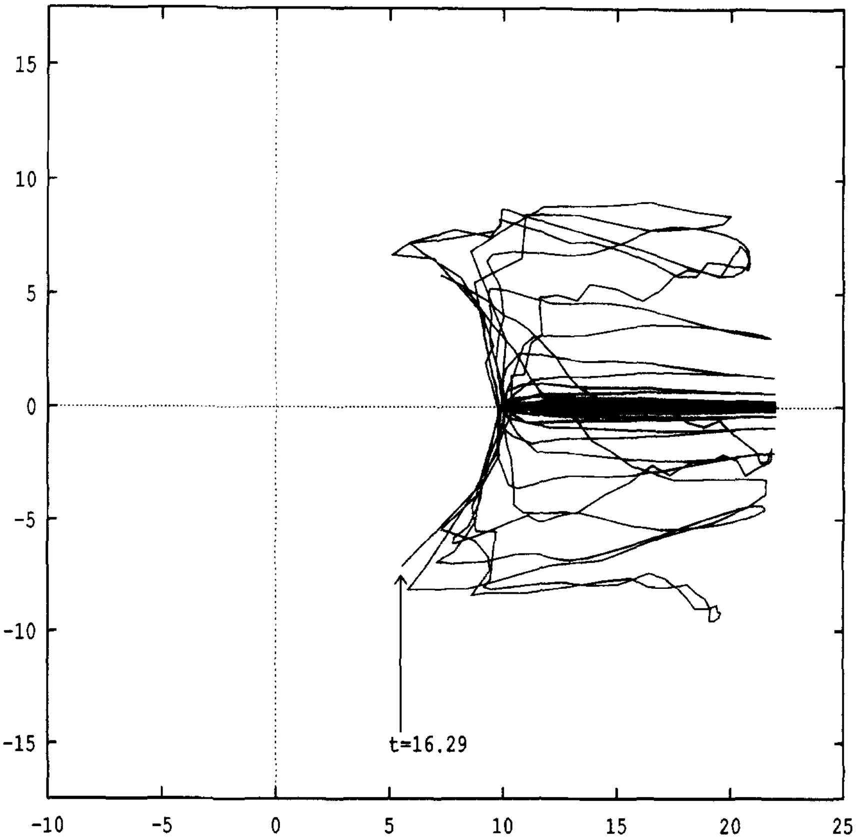

Fig. 29. Parametric resonance. Second set of simulations (Contd.). $\omega = 2.8\pi$. Trace of beam tip within time interval [0, 16.29].

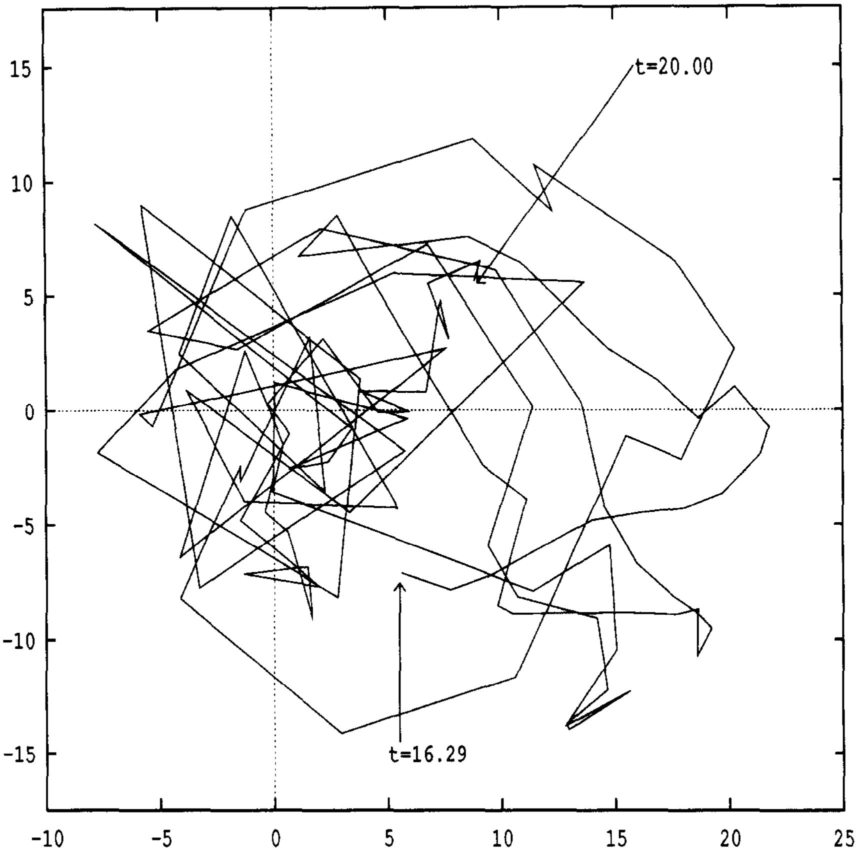

Fig. 30. Parametric resonance. Second set of simulations (Contd.). $\omega = 2.8\pi$. Trace of beam tip within time interval [16.29, 20].

deformed shapes about the time $t = 18$ presented in Fig. 31 shows some of the very peculiar deformed shapes during this wild motion.[32]

In summary, from Figs. 20 to 31, a qualitative observation consistent with results from linearized theories (e.g. [23, 24]) is that increasingly agitated behavior in the beam vibration is encountered at higher sliding frequencies ω.

6. Closure

We have presented two formulations for sliding geometrically-exact beams. In addition to the sliding motion, the beam can undergo large deformation, large overall motion, with shear deformation accounted for. Both the sliding motion of the beam and the rigid body motion of the prismatic joint can be prescribed. The first formulation is based on a full Lagrangian description of the motion, leading to a set of PDEs defined on a time-varying domain. A stretched coordinate is introduced to map the resulting equations of motion to a constant domain. The second formulation is based on the Eulerian–Lagrangian description with the introduction of an intermediate configuration, and is shown to be theoretically equivalent to the full Lagrangian formulation. The Eulerian–Lagrangian equations, defined on a time-varying domain, do not offer much more of an advantage over the original full Lagrangian equations (in material coordinates), also defined on time-varying domain. Here, we adopt the full Lagrangian equations in stretched coordinate, defined on constant domain, for the computational works. The inertia operator of these equations has a structure similar to that found in the equations

---

[32] Further investigations need to be carried out to determine whether the wild motion of the beam in the interval [16.29, 20] is due to numerical instability.

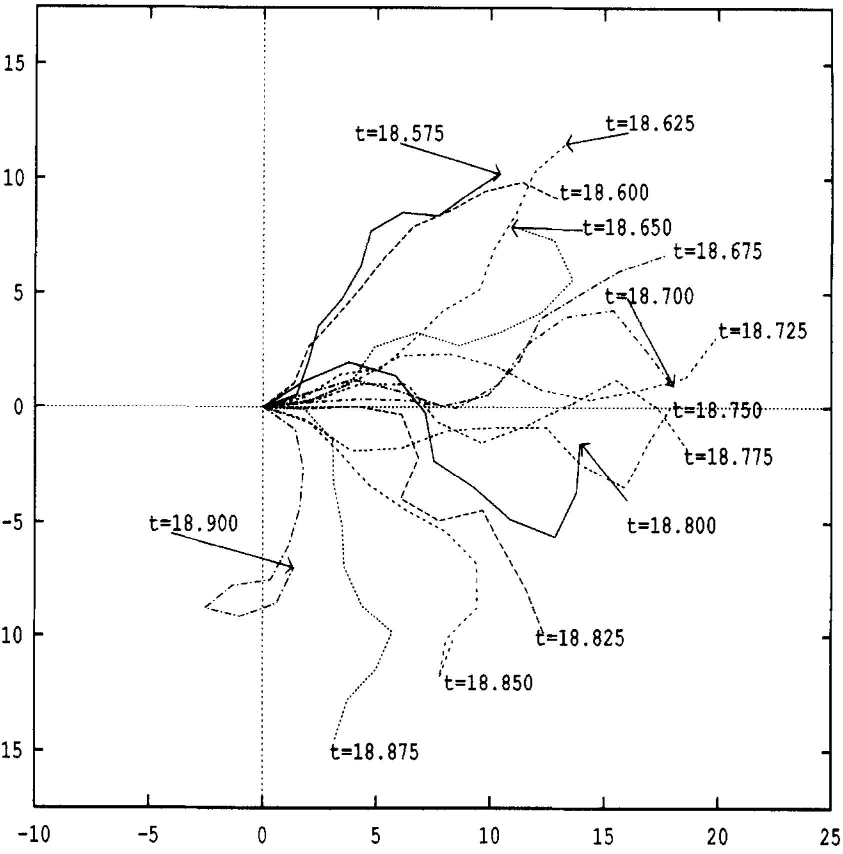

Fig. 31. Parametric resonance. Second set of simulations (Contd.). $\omega = 2.8\pi$. Sequence of snapshots of deformed shapes about time $t = 18$.

of motion for the class of problems dual to the sliding beam problem, e.g. the dynamic interaction of high-speed vehicles on flexible guideways. That the inertia operator is, however, decomposable into a symmetric part and an anti-symmetric part, despite the absence of any rotating motion found in gyroscopic systems, is a distinct feature of the present formulation. A Galerkin projection of the full Lagrangian equations in stretched coordinate leads to a set of semi-discrete equations having time-varying coefficients, and with clear identification of various terms: Mass, velocity-convection, stiffness convection, non-linear internal force, inertia force due to sliding motion and applied force. A conceptual time discretization algorithm that covers a large class of structural dynamics algorithms is presented to provide a general framework; the resulting non-linear algebraic equations together with their linearization are discussed in detail. Several numerical examples emphasizing the salient features of the proposed formulation are given, ranging from the spaghetti problem, reverse spaghetti problem, combined deployment and large angle maneuver, non-linear parametric resonance due to periodically sliding motion. These numerical examples not only demonstrate the versatility of the proposed formulation, but also reveal the complex character of the non-linear dynamic behavior of sliding geometrically-exact beams, not obtainable with linearized theories.

Acknowledgments

The research is supported by grants from the National Science Foundation and from the SRAP program of the Florida Space Grant Consortium. This support is gratefully acknowledged. The first author thanks his students, Kyle Thornton and Hui Deng, for their help in generating the results for several examples presented above.

References

[1] C.D. Mote Jr., Dynamic stability of axially moving materials, Shock Vibration Dig. 4 (1972) 2–11.

[2] L. Frýba, Vibration of Solids and Structures under Moving Loads (Noordhoff, Groningen, 1972).

[3] L. Vu-Quoc and M. Olsson, Formulation of a basic building-block model for interaction of high-speed vehicles on flexible structures, ASME J. Appl. Mech. 56(2) (1989) 451–458.

[4] L. Vu-Quoc and M. Olsson, A computational procedure for interaction of high-speed vehicles on flexible structures without assuming known vehicle nominal motion, Comput. Methods Appl. Mech. Engrg. 76 (1989) 207–244.

[5] L. Vu-Quoc and M. Olsson, New predictor/corrector algorithms with improved energy balance for a recent formulation of dynamic vehicle/structure interaction, Internat. J. Numer. Methods Engrg. 32 (1991) 223–253.

[6] L. Vu-Quoc and M. Olsson, High-speed vehicle models based on a new concept of vehicle/structure interaction component. Part I: Formulation, ASME J. Dynamic Syst., Measurements Control 115(1) (March 1993) 140–147.

[7] L. Vu-Quoc and M. Olsson, High-speed vehicle models based on a new concept of vehicle/structure interaction component. Part II: Algorithmic treatment and results for multispan guideways, ASME J. Dynamic Syst. Measurements Control 115(1) (March 1993) 148–155.

[8] G.F. Carrier, The spaghetti problem, Amer. Mathematical Mthly 56 (1949) 669–672.

[9] J.N. Zaiser, Nonlinear vibrations of a moving threadline, Ph.D. Dissertation, University of Delaware, 1964.

[10] C.D. Mote Jr., On the nonlinear oscillation of an axially moving string, ASME J. Appl. Mech. 33 (1966) 463–464.

[11] A.L. Thurman and C.D. Mote Jr., Free, periodic, nonlinear oscillation of an axially moving string, ASME J. Appl. Mech. 36 (1969) 83–91.

[12] J.A. Wickert and C.D. Mote Jr., Classical vibration analysis of axially moving continua, ASME J. Appl. Mech. 57 (1990) 738–744.

[13] J.A. Wickert and C.D. Mote Jr., Current research on the vibration and stability of axially moving materials, Shock Vibration Dig. 20 (1988) 3–13.

[14] D.B. Cherchas, Dynamics of spin-stabilized satellites during extension of long flexible booms, J. Spacecraft Rockets 8(7) (1971) 802–804.

[15] K.W. Lips and V.J. Modi, Transient attitude dynamics of satellites with deploying flexible appendages, Acta Astronaut. 5(10) (1978) 797–815.

[16] K. Tsuchiya, Dynamics of a spacecraft during extension of flexible appendages, J. Guidance Control 6(2) (1983) 100–103.

[17] A.M. Ibrahim and V.J. Modi, On the dynamics of beam type structural members during deployment, Adv. Astronaut. Sci. 58, Part I (1985) 239–256.

[18] S. Kalaycioglu and A.K. Misra, Analytical expressions for vibratory displacements of deploying appendages, 1988 AIAA/AAS Astrodynamics Conference, Minneapolis, MN (1988) 270–277.

[19] N.G. Creamer, On the deployment of a flexible boom from an oscillating base, Proc. AIAA Dynamics Specialist Conference, Washington, DC (1990) 459–468.

[20] A.L. DilPare, Transient nonlinear deflections of a cantilever beam of uniformly varying-length by numerical methods, AIAA J. 8 (1970) 2293–2295.

[21] A.K. Banerjee and T.R. Kane, Extrusion of a beam from a rotating base, J. Guidance Control Dynamics 12(2) (1989) 140–146.

[22] R. Elmaraghy and B. Tabarrok, On the dynamic stability of an axially oscillating beam, J. Franklin Instit. 300 (1975) 25–39.

[23] J. Zajaczkowski and J. Lipinski, Instability of the motion of a beam of periodically, varying length, J. Sound Vibration 63 (1979) 9–18.

[24] J. Zajaczkowski and G. Yamada, Further results on instability of the motion of a beam of periodicity varying length, J. Sound Vibration 68(2) (1980) 173–180.

[25] N.G. Chalhoub and A.G. Ulsoy, Control of a flexible robot arm: Experimental and theoretical results, ASME J. Dynamic Systems Measurement Control 109 (1987).

[26] P.K.C. Wang and J.D. Wei, Vibrations in a moving flexible robot arm, J. Sound ibration 116(1) (1987) 149–160.

[27] K. Krishnamurthy, Dynamic modelling of a flexible cylindrical manipulator, J. Sound Vibration 132(1) (1989) 143–154.

[28] Y.C. Pan, R.A. Scott and A.G. Ulsoy, Dynamic modeling and simulation of flexible robots with prismatic joints, J. Mech. Des. 112 (1990) 307–314.

[29] Y.C. Pan, R.A. Scott and A.G. Ulsoy, Experimental model validation for a flexible robot with prismatic joints, J. Mech. Des. 112 (1990) 315–323.

[30] K.W. Buffinton, Dynamics of elastic manipulators with prismatic joints, ASME J. Dynamic Systems Measurement, Control 114 (1992) 41–49.

[31] S.S.K. Tadikonda and H. Baruh, Dynamics and control of a translating flexible beam with a prismatic joint, ASME J. Dynamics Syst. Measurement Control 114 (1992) 422–427.

[32] B. Tabarrok, C.M. Leech and Y.I. Kim, On the dynamics of an axially moving beam, J. Franklin Instit. 297(3) (1974) 201–220.

[33] L. Mansfield and J.G. Simmonds, The reverse spaghetti problem: Drooping motion of an elastica issuing from a horizontal guide, ASME J. Appl. Mech. 54 (1987) 147–150.

[34] J. Stolte and R.C. Benson, Dynamic deflection of paper emerging from a channel, J. Vibration Acoustics 114 (1992) 187–193.

[35] J.C. Simo and L. Vu-Quoc, On the dynamics of flexible beams under large overall motions – The plane case: Part I, ASME J. Appl. Mech. 53(4) (1986) 849–854.

[36] J.C. Simo and L. Vu-Quoc, On the dynamics of flexible beams under large overall motions – The plane case: Part II, ASME J. Appl. Mech. 53(4) (1986) 855–863.

[37] L. Vu-Quoc and J.C. Simo, On the dynamics of Earth-orbiting flexible satellites with multibody components, AIAA J. Guidance Control Dynamics, 10(6) (1987) 549–558, paper G87-088, Nov–Dec.

[38] J.C. Simo and L. Vu-Quoc, A geometrically-exact beam model incorporating torsion shear and torsion warping deformation, Internat. J. Solids Structures 27(3) (1991) 371–393.

[39] K. Huseyin, Vibrations and Stability of Multiple Parameter Systems (Sijthoff & Noordhoff, Alphen, 1978).

[40] T.R. Kane, R.R. Ryan and A.K. Barnerjee, Dynamics of a cantilever beam attached to a moving base, J. Guidance Control Dynamics 10 (1987) 139–151.

[41] J.C. Simo and L. Vu-Quoc, The role of nonlinear theories in transient dynamics analysis of flexible structures, J. Sound Vibration 119(3) (1987) 487–508.

[42] L. Vu-Quoc, A formulation of geometrically-exact structural finite elements for efficient implementation and computation, Internat. J. Numer. Methods Engrg, in preparation.

[43] J.E. Marsden and T.J.R. Hughes, Mathematical Foundations of Elasticity (Prentice Hall, New Jersey, 1983).

[44] J.C. Simo and L. Vu-Quoc, On the dynamics in space of rods undergoing large motions – A geometrically exact approach, Comput. Methods Appl. Mech. Engrg. 66 (1988) 125–161.

[45] T.J.R. Hughes, The Finite Element Method (Prentice Hall, New Jersey, 1987).

[46] M. Spivak, Calculus on Manifolds (W.A. Benjamin, New York, 1965).

[47] P. Smolinski, W.K. Liu, G. Hulbert and K. Tamma, eds., New Methods in transient analysis, Symposium Proc. ASME Publication No. PVP. Vol. 246 or AMD-Vol. 143, ASME Winter Annual Meeting, Anaheim, CA, November, 1992.

[48] C. Hoff and P.J. Pahl, Development of an implicit method with numerical dissipation from a generalized single-step algorithm for structural dynamics, Comput. Methods Appl. Mech. Engrg. 67 (1988) 367–385.

[49] H.M. Hilber, T.J.R. Hughes and R.L. Taylor, Improved numerical dissipation for time integration algorithm in structural dynamics, Earthquake Engrg. Structural Dynamics 5 (1977) 283–292.

[50] G.M. Hulbert and J. Chung, A new explicit time integration method for structural dynamics: The explicit generalized-α method, in: P. Smolinski et al., ed., Proc. Symposium on New Methods in Transient Analysis, ASME publication no. PVP. Vol. 246 or AMD – Vol. 143, ASME Winter Annual Meeting, Anaheim, CA, November, 1992.

[51] S. Li, On the dynamics of length-varying flexible beams under large overall motions: A geometrically-nonlinear approach, Master's Thesis, Aerospace Engineering, Mechanics & Engineering Science, University of Florida, Gainesville, FL 32611, 1993.

[52] O.C. Zienkiewicz and R.L. Taylor, The Finite Element Method, 4th edition (McGraw-Hill, New York, 1991).

[53] L. Vu-Quoc and S. Li, Dynamics of sliding geometrically-exact beams: Large angle Maneuvers and nonlinear parametric resonance. Presentation transparencies, Aerospace Engineering, Mechanics & Engineering Science report no. AeMES-TR-92-3-04, University of Florida, FL 32611, 1992.

[54] G.F. Carrier, Private conversation after his G.I. Taylor Memorial Lecture at University of Florida, Gainesville, FL, February, 1993.

[55] W.F. Ames, S.Y. Lees and J.N. Zaiser, Nonlinear vibration of a traveling threadline, Internat. J. Nonlinear Mech. 3 (1968) 449–469.

[56] S.-J. Hwang and N.C. Perkins, Supercritical stability of an axially moving beam, Part I: Model and equilibrium analysis. Part II: Vibration and stability analyses, J. Sound Vibration 154 (1992) 381–409.

[57] M.S. Jankovic, Comment on 'Dynamics of a spacecraft during extension of flexible appendages, J. Guidance, Control Dynamics (1984) 128.

[58] G.E. Weeks, Dynamic analysis of a deployable space structure, J. Spacecraft Rockets 23(1) (1986) 102–107.

[59] J. Yuh and T. Young, Dynamic modeling of an axially-moving beam in rotation: Simulation and experiment, ASME J. Dynamic Syst. Measurement Control 113 (1991) 34–40.

[60] J.C. Simo, A finite strain beam formulation. Part I. The three dimensional dynamic problem, Comput. Methods Appl. Mech. Engrg. 49 (1985) 55–70.